MODELING, SIMULATION AND ANALYSIS OF TYPE-III COMPOSITE OVERWRAPPED PRESSURE VESSELS FOR HIGH-PRESSURE GAS STORAGE

A Thesis Submitted to
the Graduate School of Engineering and Sciences of
İzmir Institute of Technology
in Partial Fulfillment of the Requirements for the Degree of

DOCTOR OF PHILOSOPHY

in Mechanical Engineering

by
Serkan KANGAL

July 2019
İZMİR

We approve the thesis of **Serkan KANGAL**

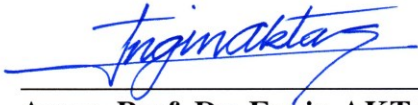**Examining Committee Members:**

_____
Prof. Dr. Metin TANOĞLU
Department of Mechanical Engineering, İzmir Institute of Technology

_____
Assoc. Prof. Dr. Hatice Seçil ARTEM
Department of Mechanical Engineering, İzmir Institute of Technology

_____
Assoc. Prof. Dr. Engin AKTAŞ
Department of Civil Engineering, İzmir Institute of Technology

_____
Assoc. Prof. Dr. Mehmet SARIKANAT
Department of Mechanical Engineering, Ege University

_____
Assist. Prof. Dr. Levent AYDIN
Department of Mechanical Engineering, İzmir Katip Çelebi University

16 July 2019

_____
Prof. Dr. Metin TANOĞLU
Supervisor, Department of Mechanical
Engineering, İzmir Institute of Technology

_____
Prof. Dr. Sedat AKKURT
Head of the Department of Mechanical
Engineering

_____
Prof. Dr. Aysun SOFUOĞLU
Dean of the Graduate School of
Engineering and Sciences

ACKNOWLEDGMENTS

ABSTRACT

MODELING, SIMULATION AND ANALYSIS OF TYPE-III COMPOSITE OVERWRAPPED PRESSURE VESSELS FOR HIGH-PRESSURE GAS STORAGE

In this thesis, multi-layered composite overwrapped pressure vessels (COPVs) for high-pressure gaseous storage were modeled by finite element (FE) method and manufactured by filament winding technique. Two liners with distinct geometries were utilized for containing gas and forming a basis for composite filament winding. 34CrMo4 steel as a load-sharing metallic liner was selected for investigation of hybridization effects. Glass and carbon filaments were overwrapped to the liner with a winding angle of $[\pm 11°/90°_2]_3$ to obtain a fully overwrapped composite reinforced vessel with non-identical front and back dome endings. The other type of liner was made of Al 6061-T6 and chosen for containing high-pressure gas such as hydrogen and its better strength-to-weight ratio suitable for onboard applications. Doily layers were implemented to the structure for inducing safe burst modes and increasing the burst pressure of the aluminum-based COPVs. All vessels were hydrostatically loaded with increasing internal pressure up to the burst pressure. The mechanical performances of pressure vessels were investigated by both experimental and numerical approaches. In numerical approaches, FE analysis was performed featuring a simple progressive damage model available in ANSYS for composite section. The metal liners were modeled as elastic-plastic material with two different hardening approaches; bilinear and multilinear hardening. The results from steel based COPV indicate that the FE model provided a good correlation between experimental and numerical strain results for the vessels with indications that the composite interlayer hybridization has positive effects on radial deformation of the COPVs. The constructed model for aluminum-based COPVs was also able to predict experimental burst pressures within a range of 8%.

Keywords: composite overwrapped pressure vessels (COPV), filament winding, manufacturing, hybridization, burst pressure, finite element analysis (FEA), ANSYS, progressive damage, polymer composites, hydrogen storage.

ÖZET

YÜKSEK BASINÇLI GAZ DEPOLAMA İÇİN TİP-III KOMPOZİT SARILI BASINÇLI KAPLARIN MODELLENMESİ, BENZETİMİ VE ANALİZİ

Bu tez çalışmasında, yüksek basınçlı gaz depolama için çok katmanlı kompozit sarılı basınçlı kaplar sonlu elemanlar metodu ile modellenmiş ve filaman sarma yöntemi ile üretilmiştir. Birbirinden farklı geometri ve malzemelere sahip iki tip iç gömlek, gaz depolama ve kompozit filaman sarma tekniğinde mandrel olarak kullanılmıştır. 34CrMo4 çeliği, katmanlararası hibritleşme etkilerinin incelenmesi için yük paylaşabilen metalik iç gömlek için seçilmiştir. Cam ve karbon iplikler iç gömlek üzerine $[\pm 11°/90°_2]_3$ oryantasyonunda, tamamen kompozit takviyeli ve ön ve arka dom kısımları birbirinden farklı basınçlı kaplar elde edilmesi için sarılmıştır. Diğer iç gömlek ise 6061-T6 alüminyumdan yapılmıştır ve hidrojen gibi yüksek basınçlı gaz ihtivası ve taşınabilir uygulamalar için uygun olan daha iyi mukavemet-ağırlık oranı sebebiyle seçilmiştir. Yapıya yama katmanları eklenerek alüminyum esaslı kompozit sarılı basınçlı kapların patlama basınçları arttırılmıştır ve güvenli patlama modları tetiklenmiştir. Tüm basınçlı kaplar iç basınçları patlama basıncına kadar hidrostatik olarak yüklenmiştir. Basınçlı kapların mekanik performansları hem deneysel hem de nümerik yaklaşımlarla incelenmiştir. Nümerik yaklaşımlarda sonlu elemanlar analizi kompozit kısım için ANSYS'te bulunan basit ilerlemeli hasar modeli ile gerçekleştirilmiştir. Metalik iç gömlekler iki farklı sertleştirme yaklaşımı; ikidoğrusal ve çokdoğrusal pekleşme ile elastik-plastik olarak modellenmiştir. Çelik esaslı kompozit sarılı basınçlı kapların sonuçları incelendiğinde sonlu elemanlar modeli deneysel sonuçlarla iyi bir bağıntı sağlamıştır. Nümerik gerinim sonuçları da katmanlar arası hibritleşmenin radyal deformasyon üzerinde pozitif etkileri olduğunu işaret etmektedir. Alüminyum esaslı kompozit sarılı basınçlı kaplar için oluşturulan model ise patlama basınçlarını %8 sapma ile hesaplayabilmiştir.

Anahtar kelimeler: kompozit sarılı basınçlı kaplar, filaman sarma üretimi, hibritleşme, patlama basıncı, sonlu elemanlar analizi, ANSYS, ilerlemeli hasar, polimerik kompozitler, hidrojen depolama.

TABLE OF CONTENTS

LIST OF FIGURES

LIST OF TABLES

CHAPTER 1

INTRODUCTION

Throughout the history of mankind, energy and its availability were always an issue. As civilizations advance, their power and survival strictly depend on their ability to harness and store energy. Today, most of the world's energy needs are still met by fossil fuels, which are finite sources of energy. Besides their limited availability, they are responsible for CO_2 and other greenhouse gases, which are primary reasons for global warming and severe environmental pollution. Therefore, the world's leading countries and unions such as the European Union, are actively in search for preventing environmental pollution by avoiding fossil fuel dependence. In this context, at the G-7 summit held in Germany in June 2015, it was decided to completely terminate the use of fossil fuels by the end of this century.[1]

Because of its non-existent greenhouse gas emission, high energy efficiency and abundance, hydrogen is considered to be the new energy carrier of the next century.[2,3] Since the early 2000s, significant improvements have been achieved in the technologies for the public availability, and use of hydrogen energy and several commercial products have been put into use. As shown in Figure 1.1, hydrogen is used in many European cities as a carrier of energy in public transportation, private cars, hospitals, and public buildings. The developments in hydrogen technology indicate that a new market has emerged in the field of energy and opportunities will be created for different sectors.[4–7]

(a)   (b)

Figure 1.1. Onboard applications for hydrogen energy. (a) A hydrogen-powered fuel cell vehicle beside a hydrogen station, (b) a hydrogen-powered public transportation vehicle in London. (Source: Oyakhire, 2012)

Hydrogen is the first and the simplest element of the periodic table with its single electron orbiting a proton. With being the simplest element, it is also the most abundant in the universe, both with its elemental and compound forms. Hydrogen has a gravimetric density of about 140 MJ/kg, which makes it one of the highest energy-dense materials. The disadvantage of hydrogen as a fuel comes from its volumetric energy density, which is about 5 MJ/L for gaseous hydrogen at 700 bar pressure.[8] Figure 1.2 shows the comparison of gravimetric and volumetric energy densities of hydrogen with other common fuel types. It is clearly seen that increasing volumetric energy density of the hydrogen will increase its competitiveness and thus, the acceptance as a universal energy carrier for the next century.
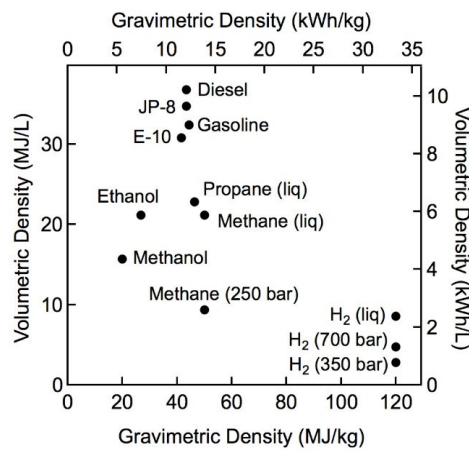
Figure 1.2. The comparison of gravimetric and volumetric energy densities of common fuel types. (Source: US Department of Energy, 2019)

Figure 1.3 shows the global estimated consumption of hydrogen in the world until 2050. In the future, it is predicted that almost 90% of the hydrogen energy will be used in transportation, and the remaining 10% will be shared by the housing and industrial sectors.[9] In order to increase the acceptance of this new type of energy and to be an alternative to fossil fuels, hydrogen must be stored in a compact and safe manner.
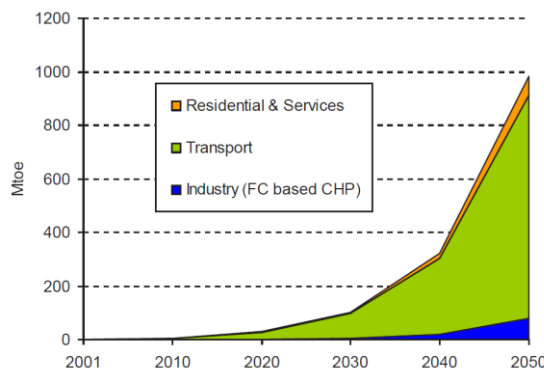
Figure 1.3. Hydrogen energy usage projection until 2050.
(Source: Enerdata, 2010)

The current state of hydrogen storage can be classified in two primary methods; (i) physical-based storage which involves storage of hydrogen in a compressed gaseous form at room or cryogenic temperatures without phase change. The phase change of hydrogen into a liquid with employing a cryogenic liquid is also considered as physical-based storage; (ii) material-based storage, which can also be called as chemical storage, involves chemical reactions for binding of hydrogen to chemical compounds. The chemical storage techniques include adsorption of hydrogen molecules utilizing a metal organic frame (MOF), boron-based hydrogen storage and metal hydride compounds.[5] Figure 1.4 summarizes the classification of the above-mentioned hydrogen storage techniques.
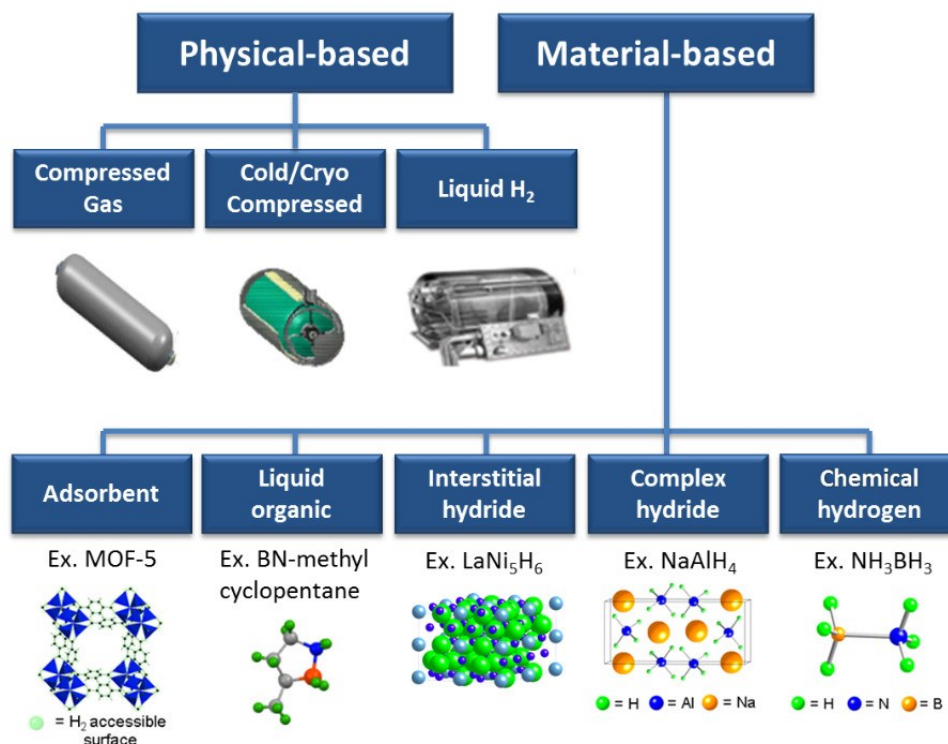
Figure 1.4. The schematic of the classification of the current hydrogen storage technologies. (Source: US Department of Energy, 2019)

Hydrogen storage as a compressed gas at room temperature is currently the most well-established method, with some advantages compared to others, such as its technical simplicity, rapid filling, and unloading processes. Another major advantage of compressed gas storage is cost. The energy required to liquefy hydrogen is between 30% and 40% of the fuel energy that hydrogen will provide. 5% to 20% of energy is required for high-pressure storage. Furthermore, the storage in the pressurized tank is carried out at room temperature, while the liquid storage is carried out under vacuum in well-sealed containers at -253°C.[10]

Gaseous hydrogen storage can be classified into four types, according to their technical performance and cost.[11,12] Type I vessels are made entirely of metal (aluminum or steel) and generally operates at a pressure between 150-300 bar which is considered as low-pressure gas storage. They have the lowest cost among all types of high-pressure vessels but also has a weight disadvantage. Type-II vessels are produced by the circumferential winding of resin-impregnated fibers on the load-sharing metal liner. This yields to an expensive product, but also lighter and resistant to higher working pressure than Type-I vessels. For high-pressure storage (300 bar and higher pressures), more advanced vessel types are needed especially for onboard applications. Type-III composite pressure vessels generally consist of a winding of fibers on the non-load bearing metal (usually aluminum) inner sleeve. Nearly complete coverage of the liner is achieved. Similarly, in Type-IV vessels, the liner is also non-load bearing and are entirely covered with composite layers. The difference comes from the liner, which is a thermoplastic material (typically high density polyethylene). This type of vessels is costlier but lighter than Type-III. Figure 1.5 shows the structural differences between the primary types of COPVs.[13]
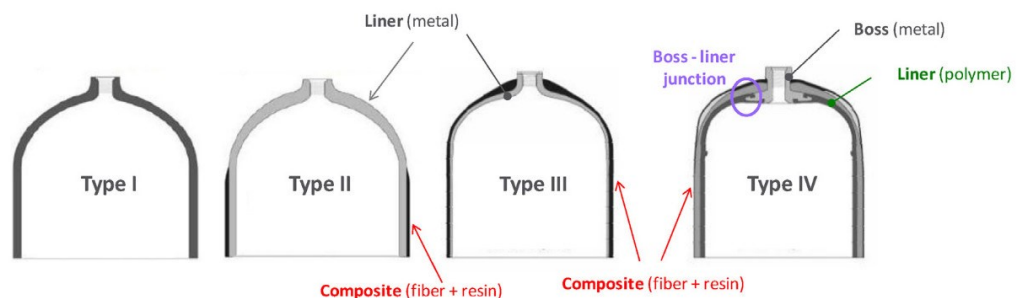
Figure 1.5. Schematic representation of Type I, II, III and IV COPVs.
(Source: Barthelemy et al., 2017)

Hydrogen storage for onboard applications is generally carried out with Type-III and Type-IV pressure vessels due to their enhanced strength-to-weight ratios. These vessels are produced by circumferential / polar / helical winding of carbon fibers onto aluminum or polymer liner. The non-load-bearing metal or polymer part ensures gas tightness and insulation of the composite material with the stored material, while the carbon fiber / epoxy layers form the structural integrity. Nearly 85% of the applied pressure is carried by these layers.

Operating range of type III tanks is 350 bar in general applications. In the new generation hydrogen vehicles, approximately 4 kg of hydrogen gas is needed to ensure continuous operation at a range of 400 km. This means the need for an internal volume is

about 22 L. This value is significant for new generation hydrogen burning vehicles. This size problem can be solved by storing at higher pressures (700 bar).[14–16] Figure 1.6 shows the placement of Type-III tanks in a vehicle.[17]

Figure 1.6. Typical positioning of a COPV on a commercial hydrogen-powered vehicle, Toyota Mirai. (Source: Lawrence Livermore National Laboratory, 2019)

For Type III and Type IV storage systems, the European Union and the US Department of Energy set out the criteria shown in Table 1.1. The most important criteria are gravimetric capacity and volumetric capacity. For gravimetric capacity, 5.5% H_2, and for the volumetric capacity of 40 g H_2 / L is the lowest limits.[18]

Table 1.1. Summary of the assessment for hydrogen storage vessels compared to DOE targets. (Source: Ahluwia et al., 2009)

Performance Criteria	Unit	350 bar	700 bar	2015 target	Final target
Gravimetric Capacity	wt%	5.5	5.2	5.5	7.5
Volumetric Capacity	g-H_2/L	17.6	26.3	40	70
Storage System Cost	$/KWh	15.4	17.8	2	TBD
Fuel Cost	$/gge	56.5	54.2	60	60

In order to ensure a broader acceptance of hydrogen energy, countries consider the development of design codes and standards as one of the essential requirements. These codes and standards that will enable the systematic and accurate evaluation of the risks related to hydrogen will facilitate the manufacturers to invest in this sector and will attract more attention of the public, and thus the barriers to commercialization will be removed. Recently, international and regional standards on hydrogen storage at high pressure have been published and are shown in Table 1.2.[10]

With the established standards demanding for higher working and burst pressures, the importance of the proper modeling and manufacturing of the COPVs escalates further.

As reported in CompositesWorld magazine, the explosion during fueling of a Falcon 9 caused by a COPV failure.[19] Specifically, from the accumulation of oxygen between the aluminum liner and the composite shell leads to failure in the fiber reinforcement. Applications of COPVs in aerospace and automotive industries are similar such as the previously mentioned example and they are generally subjected to extreme conditions.

Table 1.2. Several developed standards for hydrogen storage vessels.
(Source: Zheng et al., 2012)

Country / Organization	Standard Code and Name
ISO	ISO/TS 15869 "Gaseous Hydrogen and Hydrogen Blends – Land Vehicle Fuel Tanks"
JARI	JARI S 001 "Japanese Regulation for Containers of Compressed Hydrogen Vehicle Fuel Devices"
SAE	SAE J2579 "Technical Information Report for Fuel Systems in Fuel Cell and Other Hydrogen Vehicles
EU	CGH2R Draft Revision 12 "Hydrogen Vehicles: Onboard Storage Systems Draft ECE Compressed Gaseous Hydrogen Regulation Revision 12"
PR China	"Vehicle Fiber Full Wrap Aluminum Liner High Pressure Hydrogen Cylinder"

In light of this information, it is evident that hydrogen and hydrogen energy will be part of our lives in the near future. The situation for hydrogen energy in Turkey is somehow more critical due to the fact that Turkey's lack of natural resources and so being a major importer of energy. This new energy carrier may play a crucial role as hydrogen can be produced from the electricity generated from renewable energy sources.[20] So, this brings out the problem of storage of hydrogen as an energy carrier. Considering the adoption state of hydrogen energy in Turkey, it is clear that there is a need for safe, lightweight, high-pressure pressure vessels for storing this new gaseous energy vector, hydrogen. This study is motivated by this need and aims for the improved adoption rate of alternative energy sources and carriers such as hydrogen in Turkey. The primary and specific objectives of this thesis are given in the following subsection.

1.1. Aim of the Study

The primary objective of the study is to investigate the mechanical behavior of the composite overwrapped pressure vessels suitable for high-pressure storage by utilizing the finite element method and validate the model through experimental testing. Also, the effects of inter-layer hybridization of the composite section are investigated for possible positive outcomes. Furthermore, revealing the significance of doily layers for

improving the burst pressure performance of a COPV is another primary objective of this thesis study.

In this manner, the following can be stated as the specific objectives of this study;

- Manufacturing of prototype steel and Al-based COPVs for high-pressure storage.
- Determining the mechanical properties of the materials involving the liners and the composite portion of the COPVs through experimental testing of specimens obtained from the corresponding sections.
- Developing a finite element model of full pressure vessel featuring a progressive failure model, thickness and angle variations due to the nature of the filament winding process, non-linear material, and geometric behavior.
- Obtaining burst pressure, location, and strain behavior of the COPVs and neat liners through hydrostatically pressurizing the vessels.
- Determining the effects of design parameters such as winding orientation and wall thickness to the structural performance of the vessel and to develop novel composite tank designs suitable for hydrogen storage conditions
- Implementing inter-layer hybridization of glass and carbon layers to the COPVs and revealing its effects on burst pressure and the strain behavior.
- Implementing doily layers to the aluminum carbon fiber COPVs and measuring its effectiveness for maximizing burst pressure performance of the vessels.

1.2. Novelty of the Thesis

This study contributes to the literature with two distinct approaches. First, the effect of the interlayer hybridization of the composite shell was investigated for the COPVs, utilizing a steel liner, glass, and carbon fibers. Due to the unique geometry of the steel liner, the winding angle for achieving fully overwrapped vessel and the hybrid composite layer sequence was an original contribution to the literature.

The second approach involves maximizing the burst pressure performance of a

COPV. For that, aluminum liners were manufactured with a combination of deep drawing and spinning processes and utilized for containing the gas and improving the strength-to-weight of the structure. The aluminum liners have a specific design, so the experimental evaluation and the modeling of these liners and the COPVs based on these liners were original contributions to the literature.

For maximizing the burst pressure performance of the specific aluminum liner based COPVs, only carbon fibers were utilized. In addition to filament wound carbon fibers, carbon woven layers were introduced as doily layers for front and aft dome sections to improve the burst performance and to induce burst at the cylindrical section of the vessel. Studies on the effect of doily layers on COPV structural performance was scarce in the literature, so the investigation of doily layers in a COPV is an original contribution to the literature.

In addition to the mechanical behavior investigation of the COPVs, both neat steel and neat aluminum liners were experimentally evaluated and numerically modeled. The testing of liners includes determining mechanical properties with specimens obtained from neat liners and mechanical behavior of the vessel up until the burst failure. The mechanical behavior investigation of the neat liners significantly improved the numerical predictions of COPVs and contributed to the literature.

This study investigated the full model of both neat liners and COPVs, from the boss section and front dome to the aft dome. Most of the studies in the literature assume that the cylindrical section of the vessel is the most critical part and analyzes only that specific section. Primarily due to manufacturing issues, that assumption might prove wrong, and dome sections may fail, resulting in an unsafe burst mode. For that, it is vital to analyze the vessel as a whole to identify the proper burst mode.

Due to manufacturing processes, both liners have a specific geometry, rather than a hypothetical shape-optimized vessel as a liner. This situation generates a need for non-geodesic winding for the manufacturing of the COPVs, thus creating the phenomena of winding friction and its control. This restriction creates a unique angle of helical winding for full composite coverage of the liners, which is an original contribution to the literature.

The thickness variations of the liners due to the manufacturing processes were also investigated by sectioning the liner into half. This investigation dramatically improves the accuracy of the numerical model for both the neat liners and the COPVs and adds originality to the study.

In the literature, mechanical properties of the materials involving the structural

problem generally determined from elsewhere. In this thesis, the mechanical properties of all materials involving were experimentally determined and supplied to the finite element model. This approach yields a more accurate prediction of mechanical behavior of the COPVs.

This thesis fully utilizes built-in features of ANSYS Finite Element software package for the prediction of mechanical behavior and burst pressure of the COPVs. It was observed in the literature that custom material and damage modeling needed for structural problems involving composite materials. It is shown that a commercial software package such as ANSYS can handle this specific structural problem without implementing any additional code or model, thus increasing the efficiency and lowering the computation time.

Finally, the mechanical behavior of the unique neat liners and the developed COPVs with specific configurations were investigated from at least from three different locations at the cylindrical section of the vessels, and the obtained strain behavior was compared with the results of the developed FE model.

1.3. Thesis Outline

In this chapter, brief introductory information was given, followed by the motivation of this thesis. The primary objective of the study was stated, and the specific objectives of the thesis were listed. In addition, unique contributions to the literature were also briefly discussed in the first chapter of the thesis.

In Chapter II, a summary for the composite materials and structures is given with their definition, historical information, classifications, principal applications and most common manufacturing techniques for the readers that are unfamiliar with composite materials and their terminology.

Chapter III begins with an introduction about the finite element method and then deals with numerical methods specifically for composite structures. Afterward, detailed information about composite failure criteria was given.

With Chapter IV, a comprehensive literature survey about the COPVs was provided, and different numerical approaches for the solution of COPV structural problems were investigated.

In Chapter V, experimental procedures throughout the thesis were detailed. These experimental works include tensile testing of specimens obtained from the metal liners and filament wound composite plate, materials analysis of tensile testing specimens and the COPVs and finally burst pressure testing of the neat metal liners and the COPVs.

Chapter VI emphasized on numerical modeling of the specific problem of internally pressurized neat liners and COPVs. For that, a numerical model was developed for tensile testing and validated by the experimental data. Subsequently, the validated model was employed for the case of the pressure vessels. Model reduction and mesh convergence studies were also performed for minimizing the computation time.

Chapter VII contains the results from both experimental and numerical modeling part of the thesis. Comparisons were also made followed by the discussions of the performance of numerical models for predicting the burst pressure and mechanical behavior of the COPVs.

The final chapter, Chapter VII, consists of concluding remarks of the study. Possible future studies may originate from this thesis were discussed.

CHAPTER 2

COMPOSITE MATERIALS AND STRUCTURES

Composites can be defined as a combination of at least two or more distinct materials at a macroscopic level that provides improved desired properties than those of the individual constituents used alone. The structure of a composite can be defined in two components; the matrix and the reinforcement. The reinforcement material may be in the form of fibers, particles, or flakes. The matrix covers the reinforcement and acts as a binder material and are usually in continuous nature.

Four basic features differentiate composites from conventional materials. First, they have a noticeable interface bearing a non-uniform material in macroscopical terms. Second, the resulting composite must lead to an essential change in the desired properties. Third, one constituent should have a property which is higher than the other. Lastly, each constituent of the composite must be greater than 10% in volume. In Table 2.1, the comparison of polymeric composite materials with conventional metals can be found.[21] It is clearly seen that while preserving or increasing the mechanical properties, composites significantly improve the strength-to-weight ratio of the structure compared to steel.

Table 2.1. Density related mechanical properties comparison of several composite types, individual fibers and commonly used isotropic materials. (Source: Kaw, 1997)

Materials	Specific Gravity	Young's Modulus (GPa)	Ultimate Strength (MPa)	Specific Modulus (GPa.m³/kg)	Specific Strength (MPa.m³/kg)
Graphite fiber	1.8	230	2067	0.1278	1.148
Aramid fiber	1.4	124	1379	0.08857	0.9850
Glass fiber	2.5	85	1550	0.0340	0.6200
Unidirectional graphite/epoxy	1.6	181	1500	0.1131	0.9377
Unidirectional glass/epoxy	1.8	38.60	1062	0.02144	0.5900
Cross-ply graphite/epoxy	1.6	95.98	373	0.06000	0.2331
Cross-ply glass/epoxy	1.8	23.58	88.25	0.01310	0.0490
Quasi-isotropic graphite/epoxy	1.6	69.64	276.48	0.04353	0.1728
Quasi-isotropic glass/epoxy	1.8	18.96	73.08	0.01053	0.0406
Steel	7.8	206.84	648.10	0.02652	0.08309
Aluminum	2.6	68.95	275.80	0.02652	0.1061

Throughout history, men have constantly been attempting to shape and create new materials with more exceptional features than the previous ones by combining materials

into each other. An example comes from the Japanese warriors called Samurais. They made use of laminated metals to obtain the desired results in the forging of their swords. As another example, in the Ancient Egyptian Period, workers of pyramid constructions combined chopped straw with bricks in order to boost the integrity of their structures.

In the early 20th century, the reinforced concrete was produced by the civil engineers who combined cement with steel. World War II also witnessed another combination of materials, to say fiberglass polymer matrix composites. This has also paved the way to the use of this material nowadays. In Figure 2.1, one can see a comparison of composites with materials on the basis of specific strength within the framework of a historical timeline.
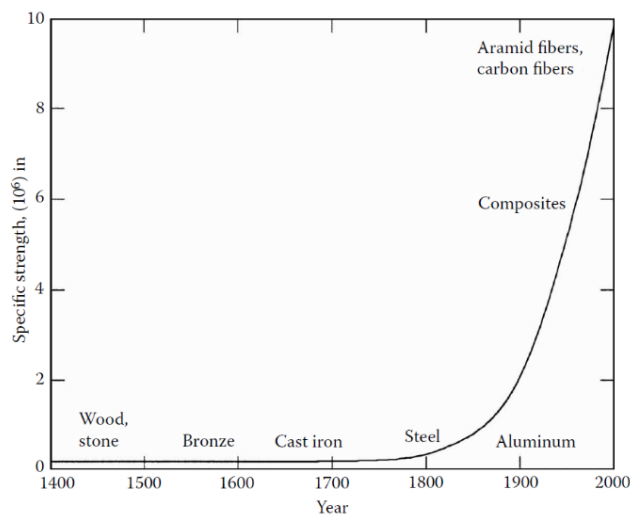
Figure 2.1. Specific strength as a function of time of use of materials.
(Source: Kaw, 1997)

Modern composites are usually made of two phases; the reinforcement phase and the matrix phase. The reinforcing phase provides strength and stiffness to the composite material, and the matrix material acts as a medium to transfer the load to the reinforcement and gives ductility and toughness to the composite material.

2.1. Classification of Composite Materials

Composites were generally classified by the type of matrix constituent, the reinforcement geometry, or their structure.

Structurally, composites can be classified into two categories; the laminated composites and sandwich structures. The former has two distinctive properties. First,

12

multiple layers are piled together. Second, they consist related or unrelated fiber angles with the intention of accommodating different loading types. The application domains of composite structures can be determined by designing the orientation of the laminated composites. The scope of this thesis ultimately involves laminated fiber reinforced composites.

Sandwich structures basically consist of two faces and core material. Faces can be laminated composites or conventional materials such as metals. The core material generally has a low density and greater thickness than the faces. The introduction of the core material between the faces improves the deflection capabilities of the resulting structure while increasing the strength-to-weight ratios.

2.1.1. Classification by the Reinforcement Geometry

The reinforcement geometry in the composites can be classified as fiber, flake, and particulate. A representation of different reinforcement geometries is shown in Figure 2.2.

The fiber, matrix, and the interface region constitute the fiber reinforced composites. A number of materials such as aramid, carbon, glass, flax, etc. can be made use in composites. There are two types of fibers in terms of their continuity: continuous fibers or discontinuous fibers such as mats and short fibers. The former follows a specific orientation and can be easily controlled. The latter, on the other hand, follows a random orientation. Woven clothes and helical winding exemplify the continuous reinforcements, whereas chopped fibers and random mats are the typical examples of discontinuous reinforcements.

Discontinuous fibers are referred to as short fibers as well since their length is lower than 0.3 cm. Besides, they are placed into a matrix randomly. This random placement leads to a more isotropic behavior in discontinuous fibers when compared to the continuous ones.

A flake reinforcement is included as a flat reinforcement to the matrix. Glass, aluminum, and silver are typical examples of flake materials. Such composites are advantageous in three ways. First, they are high out-of-plane flexural modulus. Second, they have a higher strength. Last, they are advantageous with their low costs. Some

disadvantages also follow. Such flakes employ only a limited number of materials. In addition, they cannot be easily oriented.
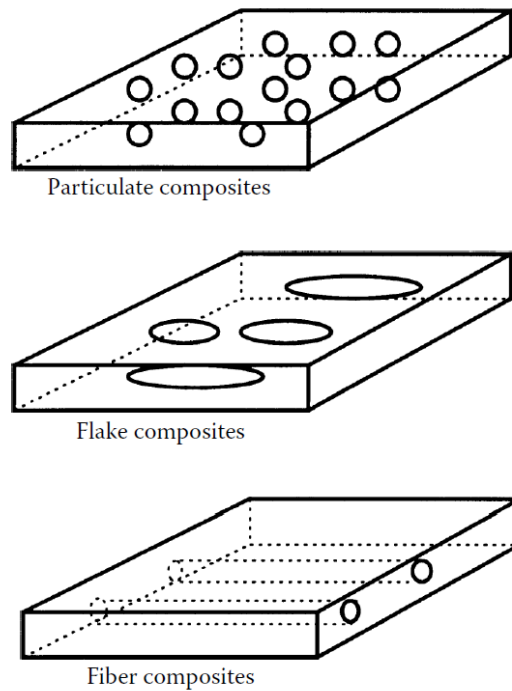
Figure 2.2. Types of composites based on reinforcement shape.
(Source: Kaw, 1997)

Particles in various sizes are found in particulate composites, and they are generally ranged from nanometer to micrometer, which is spread in matrices such as, ceramics, alloys, etc. Since the particles spread homogeneously, they often behave in an isotropic manner. Particulate composites are advantageous in a couple of aspects. First, their endurance level is high, which means they have improved strength. They bear a more increased operating temperature. Last but not least, they are resistant to oxidation. The use of gravel, sand, and cement in order to make concrete is a typical example of a particulate composite. Another example is using silicon carbide in aluminum, and aluminum particles in the rubber.

2.1.2. Classification by the Matrix Constituent

A composite's matrix phase bears some significant functions. Binding the components of the composite and adjusting the thermo-mechanical stability can be counted as the first function of the matrix phase. Moreover, it not only provides protection

of reinforcements against wear, environmental effects, impact, etc. but it serves as a stress-transfer medium and distributes the applied load as well. It also enables the structure to be more durable and tough. The role of the matrix is more complicated than the reinforcement when it comes to the strength and toughness of the composite. As the stress on reinforcing components such as glass, boron fibers, and graphite is too much to lead to an unstable flaw growth, those components go through a fatal failure since they are linear and fragile solids. Notwithstanding the fact that the reinforcing component, as well as the matrix, are fragile, the combination of them may yield a very tough material. This material will be much tougher than either of the components in isolation, and this is the result of synergism of a combination of mechanisms, which is inclined to keep cracks and flaws on a minimum level. It also has a tendency to distribute mechanical energy in an effective way.

2.1.2.1. Polymer Matrix Composites (PMCs)

Polymer matrix composites (PMCs) consist of a polymer which is reinforced by thin diameter fibers such as aramids, borons, etc. They are known as the most common advanced composites due to their high endurance and low costs. They are also products of simple manufacturing principles.[22] Graphite/epoxy composites are one of the typical examples of such composites due to the fact that they are approximately five times stronger compared to steel on a weight-to-weight basis. There are also a number of disadvantages of PMCs. Owing to the polymeric nature of the matrix, they can only endure low operating temperatures, and they have high coefficients of thermal and moisture expansion. They also display low elastic properties in matrix dominant directions. Kevlar, glass, and graphite are the most known and common fibers used in this domain.

2.1.2.2. Metal Matrix Composites (MMCs)

There are definite reasons as to why metals are employed as the primary material in MMCs. One of the reasons is that they can endure higher temperatures in the

application. Second, they are stronger and stiffer transversely. Another reason is that they have a high toughness level. Furthermore, there is no risk of flammability, and the moisture effect is absent in metal matrices. They also have high resistance against radiation. As a conductor, they are useful in both electrical and thermal procedures. Not only do MMCs have a higher level of strength-to-density, and stiffness-to-density ratios, but they also display better fatigue and wear resistances than monolithic metals. Like the last reason, conventional metalworking equipment can duplicate MMCs.

On the other hand, there are also some drawbacks for MMCs. First, most of the metals are known to be heavy. Note that since titanium and stainless steel have higher densities, they are not included in the advanced group. Second, metals are vulnerable to degradation on interface level at reinforcement and matrix. As a matter of fact, degradation of properties at high temperatures can be observed in almost all metals. This means that MMCs also display some thermal limitations in use.

Aluminum, copper, and magnesium are the metals which are commonly used in MMCs. Among these metals, aluminum, whose alloys are generally employed with silicon carbide coated boron, has a temperature of application which is higher than 300 ºC. Besides, 6061 aluminum combines strength, corrosion resistance, and toughness, and it is used more frequently than in 1100 or 2024. As known, 1100 is a pure aluminum with a high level of Charpy impact resistance. 2024, on the other hand, yields the highest strength. 800 ºC is the temperature at which titanium can be employed as a matrix for borsic fibers. Magnesium alloys can generally be used with graphite reinforcements. For the composite, it needs to have 177 MPa of longitudinal tensile strength, and 90 GPa moduli value.

2.1.2.3. Ceramic Matrix Composites (CMCs)

Metallic and non-metallic elements can compose ceramics, and there are a number of reasons as to why they are employed as the matrix material. First of all, they have an application temperature of higher than 2000 ºC, which means that they accommodate applications of heat engine.[23] Second, they are known to have low density, and they generally display high modulus values of elasticity. What is disadvantageous about ceramic matrices is that they are very fragile, thus inclined to exhibit flaws. In addition

to their brittleness, they are non-uniform and display low thermal and mechanical shock resistance. Their fragile nature is their major weakness in that a minor surface scratch or internal defect can malfunction the whole structure. What is necessary here is to produce sturdy ceramic materials. Glass ceramics such as lithium aluminosilicate, oxides such as alumina and mullite, nitrides such as silicon nitride, and carbides such as silicon carbide are the four most commonly used ceramic matrix materials.

2.1.2.4. Carbon/Carbon Composites (C/Cs)

Carbon is also employed as a matrix material in composite systems with carbon fibers. The carbon matrix and its carbon/carbon (C/C) composite are resistant against high temperatures even in excess of 2200 ºC. This is one of the several advantages of such composites. Another advantage can be said as the elevated temperatures provide extra strength to those composites. High strength-to-weight and high stiffness-to-weight values can be observed in C/C composites as well as high dimensional stabilities and resistance to exhaustion. Therefore, wherever temperatures are high, structural, and non-structural applications tends to employ C/C composites. For instance, such composites are used on the leading edge and on the rocket engine nozzles of the NASA space shuttle. High temperatures are observed on those points during flight and re-entry and in the brake system of airplanes.

It is already known that, carbon is inert in chemical and biological processes; therefore, the human body keeps it in a sterile way. Also, developers and manufacturers can use the composite as prosthetic devices. Such applications are the ones used in medical fields other than those extensive use of the composite in high-temperature applications. For instance, the structure of the bone is very similar to this composite hips and joints can be replaced by C/C composite in medical surgeries. Another application in the medical field is the internal or surgical implants since those composites are much more corrosion resistant than metal alloys and stainless steel. They are also inherently robust. On the other hand, the most known drawback of C/C composites is their cost. In other words, both the material and the fabrication processes are quite costly for this type of composites. So this drawback is the main reason behind the limited range of applications of this superior material.

2.2. Applications of Composite Materials

As technology advances, its necessities have urged many new needs to emerge in the last fifty years. Those needs should be compensated with new advances in new materials and manufacturing technologies, and so have it been so far. The market in which composites are employed can be given as follows: aerospace, consumer products, construction, corrosion resistant equipment, automotive, marine, appliance/business equipment, among others.[21–26] The benefits of composite materials were first noticed in the aerospace industry. Nowadays, with the help of composites, airplanes, rockets, and missiles all fly higher and faster. Glass, carbon, and Kevlar fiber composites are designed to be used in aerospace parts are shown in Figure 2.3.
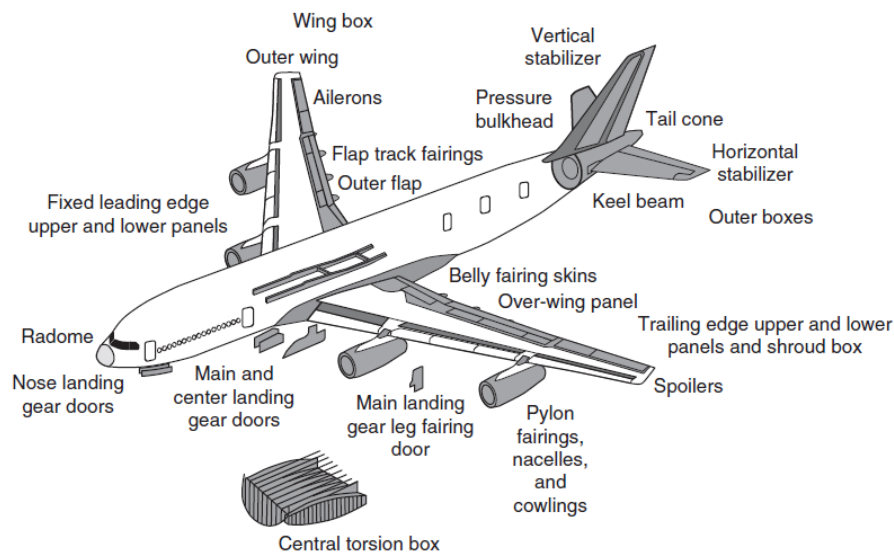
Figure 2.3. Illustration of usage of fiber reinforced polymer composites in an Airbus 380 commercial airplane. (Source: Mallick, 2007)

Since carbon fiber composites display high performance, the aerospace industry is one of the industries that mainly makes use of carbon fiber composites. Due to the fact that composite materials provide weight savings and dimensional stability, they are commonly used in spacecraft applications. It is significant that dimensional stability is maintained in support structures and reflecting members in low Earth orbit since the variation in temperature ranges between –100 to +100°C. Carbon epoxy composite laminates are sometimes constructed in a way that they yield a zero coefficient of thermal expansion. Space structures are typically defined as tubular truss structures, which include facesheets, and antenna reflectors, etc. Weight savings up to 1200 kg are provided per space shuttle if composite materials are to be employed.[24]

A couple of applications in the automotive industry considers composite materials to be the *material of choice* by means of furnishing the details, concluding a high-quality surface finish, as well as processing choices. The automotive industry needs more and more composites as the technology and the demands of the people advances, and the manufacturers can meet those demands to reduce the cost, to shine the appearance, and to boost the performance. Nowadays, one can track records of composite body panels in many categories of automotive industry ranging from sports cars and personal cars to medium, and heavy trucks. Since carbon fiber composites are high in material costs, they have not been acknowledged as the primary material so far. One of the reasons for this is that the automotive market is cost-sensitive and attempts to achieve a low cost – high-performance quality. The primary reinforcement material in automotive composites is glass fibers.

Composite materials are also becoming very popular among recreation equipment suppliers as well as sports equipment suppliers. Structural composites that were used in sporting equipment has boosted the performance in sporting goods and racing boats. Composite materials can be encountered anywhere – for instance in a store where sporting equipment is sold such as rackets, fishing rods, golf shafts, etc. All those materials are made of composite materials. The positive side of these products is that they are light, easy to handle and provide high performance, which, in turn, yields an increased comfort.[25] Figure 2.4 shows a racing bicycle made of carbon fiber reinforced polymer matrix composites.

Figure 2.4. Lightweight race bicycle made of composite parts.
(Source: Long, 2005)

Marine applications also employ composite materials in many applications such as boats, buoys, ferries, etc. since they are resistant against corrosion, and they are constructed out of light materials. This, in turn, boosts fuel efficiency, cruising speed, and yields a high rate of portability. Glass-reinforced plastics whose core materials are foam and honeycomb are the primary material in most components.

Offshore pipelines also include composites in order to extract oil and gas. Glass-reinforced plastics are used in this industry for such applications since it reduces handling and installation costs. It also provides better corrosion resistance as well as mechanical performance. Besides, it provides adhesive bonding. This removes the requirement for a hot process in cases where welding is necessary.

CHAPTER 3

FINITE ELEMENT ANALYSIS OF COMPOSITE STRUCTURES

Finite element (FE) analysis is an immensely powerful numerical method for solving physical problems within several disciplines, including structural mechanics, fluid dynamics, and electromagnetism. FE method became a widespread analysis technique particularly for structural problems with the development of digital computers in the 1950s and exponential increase of computational power since the 1980s.[27] A solution to a complex structural problem may be only available through FE analysis. Even though a solution may obtainable, nonlinearities in the physical problem, including, material model and properties, geometry and contact can remarkably increase computational time. To decrease computational time/power, some assumptions and simplifications can be made and/or specific analytical approaches may have implemented to the FE solution algorithm using a FE software package such as ANSYS.

3.1. Finite Element Method

Analytical and finite element methods are frequently used methods in the solution of engineering problems. If a physical problem can be solved analytically, then the analytical method is the best way to solving that problem. However, it is not always possible to solve most of the engineering problems through analytical methods. In such cases, the finite element method is used as a numerical solution method for the problem.

The finite element method basically divides complex problems into simpler sub-problems, and then the sub-problems are solved with a system of equations. The method has three main characteristics: First, the solution domain, which is generally referred to a geometrically complex region, divided into geometrically simple sub-domains called the finite elements. Second, it is assumed that continuous functions in each element can be defined as linear combinations of algebraic polynomials. The third assumption is that it is sufficient to solve the problem by obtaining the values of the definition equations,

which are continuous in each element of the searched values at specific points, which are called nodes.

Approximation functions are selected from polynomials using general concepts of interpolation theory. The degree of the polynomials selected depends on the degree of the equation of definition of the problem and the number of nodes in the element to be solved. In a continuous environment, field variables (stress, displacement, pressure, temperature, etc.) have an infinite number of different values. If it is known that a domain is a continuous medium, the variation of the field variables in this sub-domain can be defined by a function with a finite number of unknowns. Depending on the number of unknowns, the selected function can be linear or higher order. Since the sub-domains of the continuous medium are the same characteristic regions, when the field equation sets belonging to these regions are combined, a set of equations representing the whole system is obtained. By the solution of the equation set, field variables in the continuous medium are obtained numerically. Figure 3.1 shows the finite element model of a tire consisting of hexahedral elements throughout the solid body.[28]
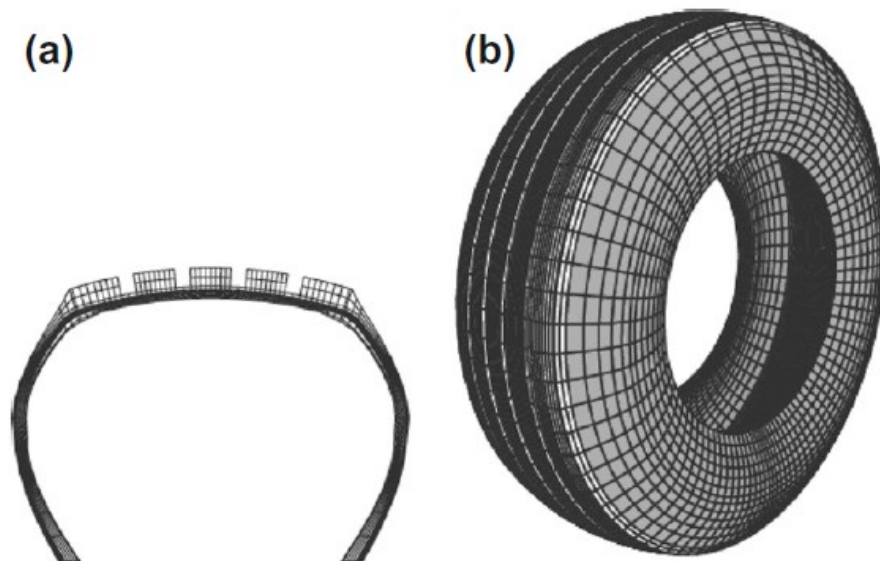
Figure 3.1. Finite element model of a tire: (a) tire cross-section, (b) full model.
(Source: Zienkiewicz et al., 2014)

The approximation solution method to be used in problem solving with the finite element method does not change the procedure to be followed. The steps in the solution method are:

- Dividing the object into finite elements
- Selection of interpolation functions
- Formation of the element stiffness matrix

- Calculation of system stiffness matrix

- Finding the forces acting on the system

- Determination of boundary conditions

- The solution of system equation

In the finite element method, the object to be analyzed is assumed to be divided into tiny elements in the finite dimension. One-dimensional objects are separated by nodes, two-dimensional objects are separated by boundary lines, and three-dimensional objects are separated by fields. In two- and three-dimensional objects, element dimensions or element shapes may be different from each other. Nodes are taken at the intersection points of the boundary lines. As a result of this separation, the body will be transformed into a structure consisting of a finite number of elements and nodes connecting them together. The division of the above-mentioned elements forms the basis of the finite element method. An illustration of a 3D solid finite element which consists of eight nodes with three degrees of freedom is shown in Figure 3.2.[29]
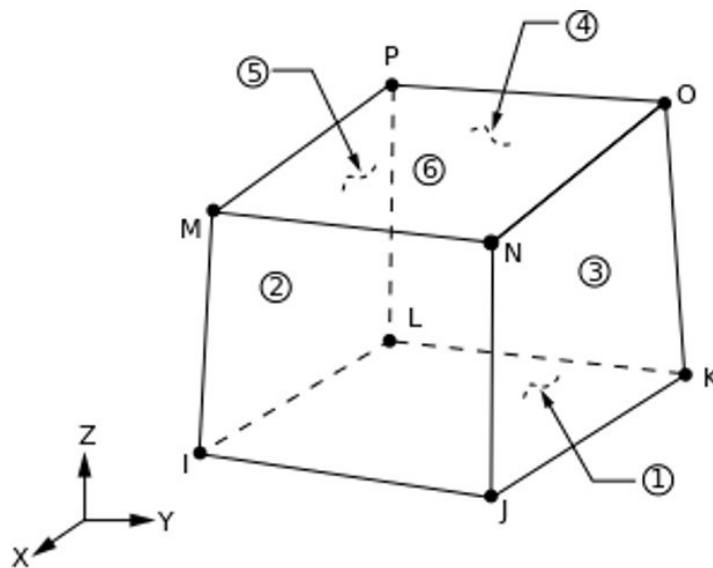
Figure 3.2. A representation of a solid 8-node hexahedral element.
(Source: ANSYS Inc., 2017)

In addition to solid elements, shell elements can also be employed for solving structural problems with the finite element method. Utilizing shell elements can lead to massive computation time savings since the model ends up with fewer mesh elements and nodes. It can be also noted that it is easier to mesh extremely thin solid details and prevents calculation errors.

Shells elements are basically a simplification of solid elements with special cases. With thin shells the third dimension (generally thickness) data stored as a physical

property rather than a geometric property of the model and by doing so, the element becomes 2D abstraction of a solid element. Because of this, stress through the thickness is not considered in the thin shell elements.

Shell elements are suitable for structural problems with geometries featuring small thickness over length (t/L) ratios. With small t/L ratios, transverse shear deformations are not important and shell elements can be employed for the efficiency of the FE analysis. When t/L is large, shear deformations through the thickness becomes dominant and solid elements should be used.

Considering the specific structural problem of the composite overwrapped pressure vessels, most of the structure has low t/L ratios, so shell elements can be employed. Due to the nature of the filament winding process, thickness and fiber angle are subject to change in end dome sections of a COPV. These regions considered as critical for the failure of the vessel. So, when considering thickness buildup in the composite section of a COPV, through the thickness stresses might become apparent and should be considered. In this case, solid elements should be utilized. Through this thesis study, 8 and 20 node solid elements were utilized considering the abovementioned scenario. The specific 8-node element also named as SOLID185 in ANSYS software package, will be heavily utilized throughout the FE analysis of this thesis and shown in Figure 3.2.

It must be pointed out that the finite element method provides approximate results to the physical problem. The accuracy of these results is directly related to FE method variables, including the element type, the mesh structure, the boundary conditions and the loading types that are used in the model.

3.2. Nonlinearities in Finite Element Analysis

In structural analysis, the linear region was identified where a linear relation exists between applied forces and the resulting displacements. The linear static analysis is conducted in this specific region and applicable until stresses remain in the elastic range of the materials involved in the problem. The stiffness matrix is constant in this region and the solution time for the analysis are very short. For a preliminary understanding of the structural problem, generally, a linear static analysis was conducted before the

addition of any complexities.

Regardless, a nonlinear relation may exist or occur between the applied force and the resulting displacements. There might be several reasons for the nonlinear behavior and can be listed as;

- Geometrical nonlinearities which correspond to large deformations of the structure,

- Material nonlinearities which indicate material behavior change over the applied loading such as yielding that occurs in elastoplastic materials,

- Contact or constraint nonlinearities which can be caused by relationships that hold in contact surfaces (such as friction) and boundary conditions that create imposing restrictions on the movement of the structure after a certain level of deformation.

All these effects result in a non-constant stiffness matrix during the loading, in contrast with linear static analysis where the stiffness matrix remained constant. In a non-linear analysis, different approaches needed to solve the structural problem and this requires drastically more computation power than the linear analysis.

In this thesis, geometrical and material nonlinearities occur in the specific problem of pressurizing the composite overwrapped pressure vessels. Geometrical nonlinearities are due to the large deformations that were expected to occur until the burst failure of the structure. Material linearities occur due to the elastoplastic behavior of the steel and aluminum liner materials. In addition, the failure and damage behavior of the composite reinforcement also introduces an important material nonlinearity to the structural problem in this thesis study.

The following section will briefly explain how the elastoplastic materials behave and were modeled in this study as understanding the plasticity of the isotropic liner material is vital for determining the burst pressure of the COPVs.

3.2.1. Plasticity models in FE Analysis

As mentioned in the previous section, the yielding of material creates a nonlinearity in isotropic materials. Several plasticity theories are used to model materials under loadings that causes the material to go beyond their elastic region. Figure 3.3 shows

a typical behavior for an elastoplastic material which features linear elastic region initially, followed by a nonlinear plastic region. The unloading of the material at any point at the plastic region reveals the permanent deformation of the material, as only the elastic strain recoverable.
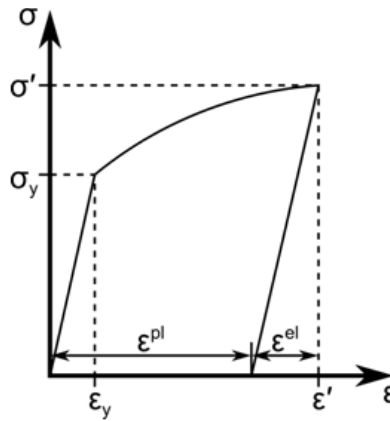
Figure 3.3. A typical stress-strain behavior for an elastoplastic material.
(Source: ANSYS Inc., 2017)

There are several constitutive models exist ranging from simple to complex, for simulating the behavior of an elastoplastic material. The suitability of an elastoplastic model depends on the experimental data provided for that specific material. History of the loading and the corresponding development of plastic strain affects the yield criterion for most materials. Hardening is the change of the yielding point of a material due to loading. Hardening of a material results in a change of yielding strength, which generally increases that specific property.

Isotropic and kinematic hardening is the two most known types of hardening rules. Isotropic hardening models the behavior of a material featuring monotonic loading and elastic unloading. In contrast, the phenomenon of kinematic hardening can be detected in the cyclic loading of isotropic materials, such as metals. This hardening rule used to model the buildup of plastic strain during cycling loading regimes.

Most materials show both hardening behavior and for proper modeling of a material, both hardening rules were used together to form a realistic hardening model. In this thesis, only the isotropic hardening model was featured for the sake of simplicity and computation time. Bilinear, multilinear and nonlinear rules are available for isotropic hardening model. Von Mises yield criterion is valid for all of these hardening models.

Bilinear isotropic hardening can basically be described by effective use of two lines with different slopes. Obviously, the initial slope refers to the elastic modulus of the material. After the yielding occurs, the relationship continues to be linear but featuring a

different slope than the elastic modulus. The slope of the second line that represents the plastic region of the material is called bilinear tangent modulus. For most materials, the bilinear tangent modulus can attain values between zero to the value of the elastic modulus. Figure 3.4 shows bilinear isotropic hardening behavior of a material under tensile loading, followed by a gradual compressive loading.
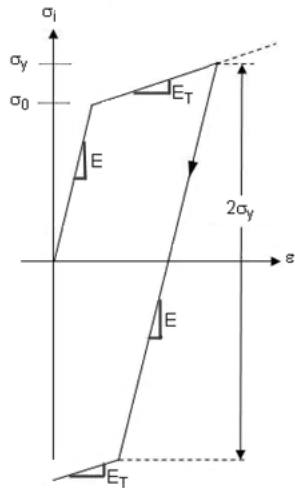
Figure 3.4. A representation of bilinear isotropic hardening behavior.
(Source: ANSYS Inc., 2017)

In multilinear hardening, rather than a single line representing the plastic region, a curve consists of a series of points models the plasticity of the material. The distinct behavior is shown in Figure 3.5.
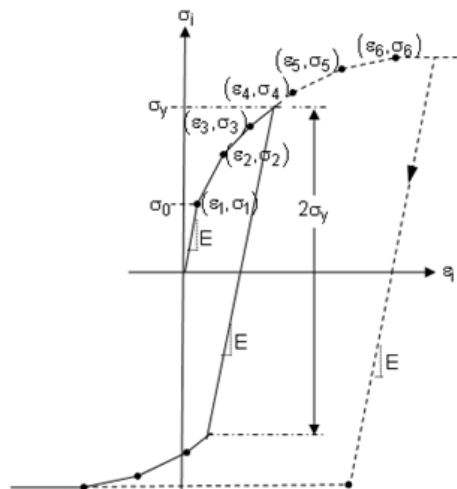
Figure 3.5. Stress vs. Total Strain for Multilinear Isotropic Hardening
(Source: ANSYS Inc., 2017)

In this thesis, both bilinear and multilinear isotropic hardening models were employed. Experimental data were utilized to determine the bilinear tangent modulus and the multilinear isotropic plastic behavior of the steel and aluminum liner materials.

3.3. Failure in Composite Materials

In structural mechanics, failure is understood as complete loss of functionality of the material system. However, in the case of composite materials, the complete failure of laminate is a process that is initiated by local failure and progresses as it the structural integrity of the laminate finally collapses.

Considering continuously reinforced fibrous composites, local failure refers to individual constituent phases, the fiber, and the matrix. Thus, failure and damage in the continuously reinforced fibrous composite can be considered as a micro-level event.

The ultimate collapse of the structural integrity of the composite laminate is a result of gradual accumulation of micro-level damage. At first, this damage accumulation is manifested at the composite laminate by some form of initial failure. This phenomenon is called "First Ply Failure" (FPF) and extensively investigated in the literature. There are many proposed criteria for FPF of composite laminates and will be briefly explained in the following sections.

Beyond FPF of composite laminate, accumulation of damage continues to progress as FPF is a micro-scale local failure. As loads and displacements on the composite laminate increase, additional local failures may occur and begin to develop. Until the final collapse of the structure, this accumulation of local failure is called "damage propagation or evolution or growth," and the branch of mechanics which studies initiation and evolution of damage until final failure of the structure is called damage mechanics. A typical path for a progressive damage analysis of composite materials is shown in Figure 3.6.[30]
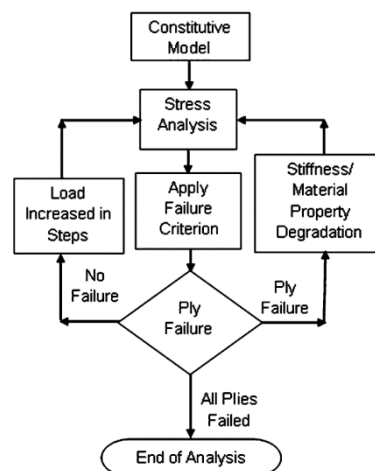
Figure 3.6. A typical flowchart for progressive failure analysis in composites.
(Source: Murugesan, 2017)

Following sections will briefly explain the most widely studied theories about the damage initiation and evolution.

3.3.1. Damage Initiation (First Ply Failure)

The concept of damage initiation states that if the stress of any lamina reaches specific stress limits, failure occurs. These specific limits may directly correspond to the strength values of the lamina or be correlated from these values. The strength values of a lamina were determined through experimental testing, considering several primary stress states such as uniaxial tensile or pure shear. Generally, these experimental evaluations were using simple and homogeneous specimen configurations and dimensions, such as unidirectional specimens. As a result, the first ply failure concept should only be applied or valid when the stress through the thickness are homogeneous. This case is usually valid in thin composite laminates, as their length to thickness ratios are substantial, and forms a basis for mechanics of composite laminates.

The first ply failure theories for composite laminates were developed from the necessity, as the established theories for conventional materials such as metals inaccurately predicts the failure for composites which are not isotropic. It is also important to note that there is no single universally accepted failure criterion for different types of composite laminates and their structural cases. This situation results in the proposal of many different approaches, and the research on this topic still ongoing today.

The classification of the first ply theories can be made by their predictive nature. To be specific, if the failure theory able to predict the failure mode of the composite in addition to the failure, it is classified as an 'interactive' failure theory. On the other hand, the theories that only predict the failure, it can be named as a 'non-interactive' theory. Several theories fall into both categories' dependent on the structure or the loading case, and presumably called 'semi-interactive' composite failure theories.

The following subsections briefly explain the major FPF theories available in the literature for composite laminates which include maximum stress, maximum strain, Tsai-Hill, Tsai-Wu, Hashin and Puck failure theories. The composite failure theories are not limited with these criteria. But Hashin being one of the most used failure criterion because of ease of application and prediction for the failure mode.

3.3.1.1. Maximum Stress Criterion

The maximum stress criterion dictates that if one of the stresses exceeds the allowable stress values for the corresponding direction, the failure will occur. This theory considers stress components independently and does not identify any failure modes. This failure criterion was directly adapted to composite materials from its first application to isotropic materials. The following inequalities were presented to examine failure;

$$\sigma_1 \geq X_t, \qquad \sigma_1 \leq X_c \tag{3.1}$$

$$\sigma_2 \geq Y_t, \qquad \sigma_1 \leq Y_c \tag{3.2}$$

$$\tau_{12} \geq S_{12}, \qquad \tau_{12} \leq -S_{12} \tag{3.3}$$

Where X is the allowable stress in the fiber direction and similarly, Y stands for the allowable stress in the transverse direction to fibers (the matrix dominated direction) and, while subscripts t and c stands for tension and compression, respectively; and S is the shear stress allowable.

3.3.1.2. Maximum Strain Criterion

The maximum strain criterion emphasizes on the allowable strain values of the composite material, in contrast to the allowable stress utilization of the maximum stress failure theory. Other than this, both approaches are very similar in nature. If one of the strains exceeds the allowable stress values for the corresponding direction, the failure will occur. The conditions of the failure theory are given in (3.4 to (3.6.

$$\varepsilon_1 \geq \epsilon_t^1, \qquad \varepsilon_1 \leq -\epsilon_c^1 \tag{3.4}$$

$$\varepsilon_2 \geq \epsilon_t^2, \qquad \varepsilon_1 \leq -\epsilon_c^2 \tag{3.5}$$

$$\varepsilon_{12} \geq \epsilon_{12}, \qquad \varepsilon_{12} \leq -\epsilon_{12} \tag{3.6}$$

In these inequalities, ϵ is the allowable strain and ε is the current strain in the corresponding direction. Subscripts t and c stands for tension and compression.

3.3.1.3. Tsai-Hill Criterion

Hill (1948) proposed a yielding criterion for anisotropic materials which can be found in (3.7.[31]

$$F(\sigma_{yy} - \sigma_{zz})^2 + G(\sigma_{zz} - \sigma_{xx})^2 + H(\sigma_{xx} - \sigma_{yy})^2 + 2L\sigma_{yz}^2 + 2M\sigma_{zx}^2$$
$$+ 2N\sigma_{xy}^2 = 1 \tag{3.7}$$

In this equation, the material anisotropy represented by the constants F, G, H, L, M and N. The values of the constants for the corresponding anisotropic material can be obtained through experimental evaluation in the principal directions. The subscripts x, y and z denote fiber, transverse and the thickness directions, respectively.

Azzi and Tsai (1965) further developed the criterion proposed by Hill (1948) for thin composite materials.[32] Out-of-plane stresses were neglected in this approach and the modified failure theory were written in (3.8.

$$(G + H)\sigma_1^2 - 2H\sigma_1\sigma_2 + (H + F)\sigma_2^2 + 2N\tau_{12}^2 = 1 \tag{3.8}$$

The constants F, G, H and N in (3.8 can be expressed as in terms of material properties, specifically strengths of each direction (X, Y and Z) and shear strength (S).

$$\frac{1}{X^2}\sigma_1^2 - \left(\frac{1}{X^2} + \frac{1}{Y^2} - \frac{1}{Z^2}\right)\sigma_1\sigma_2 + \frac{1}{Y^2}\sigma_2^2 + \frac{1}{S^2}\tau_{12}^2 = 1 \tag{3.9}$$

Azzi and Tsai (1965) also proposed an additional simplification and indicated that properties are identical in all directions except the fiber reinforcement direction, based on their dependence to the matrix material. The final form of the Tsai-Hill failure criterion was written as in (3.10.

$$\frac{1}{X^2}\sigma_1^2 - \left(\frac{1}{X^2}\right)\sigma_1\sigma_2 + \frac{1}{Y^2}\sigma_2^2 + \frac{1}{S^2}\tau_{12}^2 = 1 \tag{3.10}$$

3.3.1.4. Tsai-Wu Criterion

Tsai and Wu (1971) modified the previous anisotropic yield criterion and proposed the expression in (3.11.[33]

$$F_1\sigma_1 + F_2\sigma_2 + F_6\sigma_6 + F_{11}\sigma_1^2 + F_{22}\sigma_2^2 + F_{66}\sigma_6^2 + 2F_{12}\sigma_1\sigma_2 + 2F_{16}\sigma_1\sigma_6$$
$$+ 2F_{26}\sigma_2\sigma_6 = 1 \tag{3.11}$$

It was further claimed that the direction of the shear should be independent of the material properties. Therefore, (3.11 were rewritten as (3.12.

$$F_1\sigma_1 + F_2\sigma_2 + F_{11}\sigma_1^2 + F_{22}\sigma_2^2 + F_{66}\sigma_6^2 + 2F_{12}\sigma_1\sigma_2 = 1 \tag{3.12}$$

The constants F_1 and F_{11} can be obtainable by tensile and compressive tests in the fiber dominated direction. Similarly, F_2 and F_{22} values can be found from experimental test results in the transverse direction to the fibers. F_{66} value was obtained from the shear strength of the composite material which can be found through several shear testing techniques. The abovementioned constants can be expressed in the form of material properties and shown in (3.13 to (3.15.

$$F_1 = \frac{1}{X_t} - \frac{1}{X_c}, \qquad F_{11} = \frac{1}{X_t}\frac{1}{X_c} \tag{3.13}$$

$$F_2 = \frac{1}{Y_t} - \frac{1}{Y_c}, \qquad F_{22} = \frac{1}{Y_t}\frac{1}{Y_c} \tag{3.14}$$

$$F_{66} = \frac{1}{S^2} \tag{3.15}$$

The final constant, F_{12}, can be obtained through biaxial testing of the composite material. Due to the complicated nature of this type of testing, the assumption of $F_{12} = -0.5\sqrt{F_{11}F_{22}}$ considered as acceptable.[23]

Up until this section, the failure theories of maximum stress, maximum strain, Tsai-Hill and Tsai-Wu are modified from several yield criteria primarily proposed for isotropic materials. These theories in the literature are known as the *classical theories*. They are not capable of predicting the failure mode, which is crucial for progressive failure analysis of composite structures.

3.3.1.5. Hashin Criterion

One of the most important limitations of classical theories is that the mode of the failure is not separately defined. In other words, in those classical theories, matrix failure

and fiber failure are not considered separately. As previously mentioned, classical theories are not able to predict the first failure mode, which is required to perform progressive failure analysis. Stresses, which can cause different modes of failure, are combined to define a single failure surface in classical theories.

Hashin (1980) proposed that different failure modes can occur in fiber reinforced composite materials, and a quadratic function may not be adequate to predict the failure modes.[34] Furthermore, a failure criterion that consists of a function higher than a quadratic degree to capture the failure modes would make things more complicated. Hashin examined fiber and matrix failure separately, in contrast to previously mentioned failure theories. This results in a piece-wise continuous failure envelope, instead of a continuous failure surface. Physical representation of the failure modes considered in Hashin failure criterion were shown in Figure 3.7.[35]

For tensile fiber mode ($\sigma_1 \geq 0$); the following equation for the 3D plane stress condition was proposed.

$$\left(\frac{\sigma_1}{X_t}\right)^2 + \left(\frac{\tau_{12}}{S_{12}}\right)^2 + \left(\frac{\tau_{13}}{S_{13}}\right)^2 = 1 \qquad (3.16)$$

For the fiber compressive mode ($\sigma_1 < 0$);

$$-\left(\frac{\sigma_1}{X_c}\right) = 1 \qquad (3.17)$$
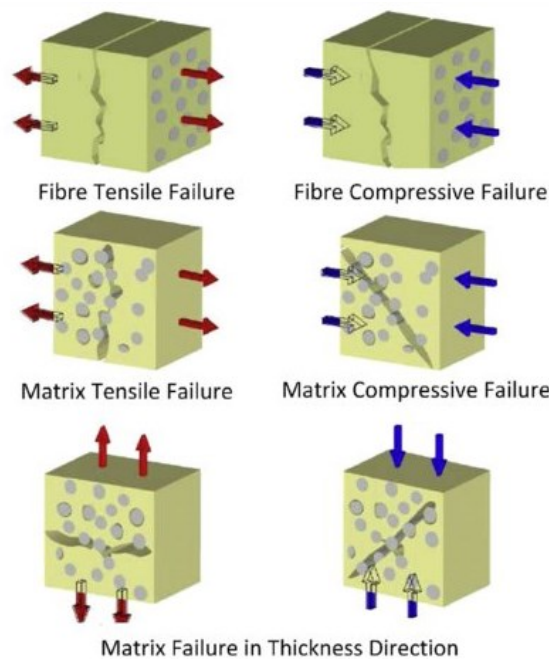
Figure 3.7. The failure modes that were considered in the Hashin failure criterion.
(Source: Doitrand et al. 2015)

The approach to the matrix failure modes is much more complicated. A failure plane, where its normal makes an angle θ with the y-axis (the matrix dominated direction), was introduced and the failure was examined for tensile and compressive according to the stress on the failure plane. The following equations expresses the conditions for the matrix failure modes for 3D stress state.

The tensile failure in the matrix ($\sigma_2 + \sigma_3 \geq 0$) can be expressed as;

$$\left(\frac{\sigma_2}{Y_t}\right)^2 + \left(\frac{\tau_{23}}{S_{23}}\right)^2 + \left(\frac{\tau_{12}}{S_{12}}\right)^2 + \left(\frac{\tau_{13}}{S_{13}}\right)^2 = 1 \tag{3.18}$$

For the matrix compressive mode ($\sigma_2 + \sigma_3 < 0$);

$$\left(\frac{\sigma_2}{2S_{23}}\right)^2 + \left(\frac{\tau_{23}}{S_{23}}\right)^2 + \left(\frac{\tau_{12}}{S_{12}}\right)^2 + \left[\left(\frac{Y_c}{2S_{13}}\right)^2 - 1\right]\frac{\sigma_2}{Y_c} = 1 \tag{3.19}$$

3.3.1.6. Puck Criterion

Puck and Schürmann (1998) published a study on the composite failure which emphasized on the different mechanisms of fiber and inter-fiber failure.[36]

The study indicated that there are significant differences between the fiber and the matrix failure. Therefore, distinct criteria for each failure mode have to be utilized. In addition to that, transverse loading should be considered separately for tensile and compression loadings. After the damage onset, gradual stiffness degradation should be gradual be observed. Additionally, for interfiber failure, the crack formation for the compressive and tensile cases should be identified.

Non-linear relationships between stresses and strains were considered for the case of shear and transverse stress and strains. Unlike the previously mentioned failure theories, Puck's failure theory analyses stresses and strains of the fibers and the matrix distinctly. A parameter which is called *stress magnification effect* ($m_{\sigma f}$) is introduced for this strategy. Transverse loadings cause different stresses on the fibers and the matrix due to the significant difference between elastic moduli of the constituents. This strategy leads to the conditions for fiber failure expressed in (3.20 and (3.21;

$$\frac{1}{\epsilon_{1T}}\left(\epsilon_1 + \frac{v_{f12}}{E_{f1}}m_{\sigma f}\sigma_2\right) = 1 \tag{3.20}$$

$$\frac{1}{\epsilon_{1C}}\left(\epsilon_1 + \frac{v_{f12}}{E_{f1}} m_{\sigma f}\sigma_2\right) = -1 \tag{3.21}$$

where ϵ denotes the allowable strain and the subscripts $f, 1, 2, T$ and C stand for fiber, longitudinal, transverse, tension and compression, respectively.

Puck failure theory introduces a failure plane for inter-fiber failure, similar to the Hashin failure criterion. The concept of the failure plane is schematically presented in Figure 3.8.[37]

Figure 3.8. The illustration for inter-fiber failure mechanism of Puck's failure criterion. (Source: Puck et al, 2002)

In contrast to Hashin failure theory, which investigates the matrix failure in two modes, Puck's theory for inter-fiber failure is categorized into three modes. For Mode A, transverse tensile stress and shear stress are present, and the angle of the fracture plane is assumed as zero. Mode B is comparable with Mode A; the only difference is being as the transverse stress is now compressive. For Mode C, stresses that are present are identical with Mode B, with the compressive stresses are significantly more dominant. This distinction causes a different failure mechanism occur in 45° failure planes. The fracture curve with addition of the physical representation of the failure modes is given in Figure 3.9.[36]

The determination of the inclination angle of the failure plane is critical in Puck's composite failure theory. For this purpose, *a stress exposure factor,* $f_E(\theta)$ is introduced to the theory. This factor is dependent on the angle and establishes the *risk of fracture* for any stress plane with an inclination of angle, θ. Finally, the fracture plane can be found by calculating the inclination angle, which maximizes the exposure factor.

As one can see, the consideration and identification of additional failure modes inevitably increase the complexity of the failure theory and its implementation to the FE

analysis. More recent failure theories also exist for the composite materials with increasing complexity such as LaRC03 and its 3D implementation LaRC04.[38,39] A comparison of several failure criteria with experimental results for transverse and shear loading was shown in Figure 3.10.[38]
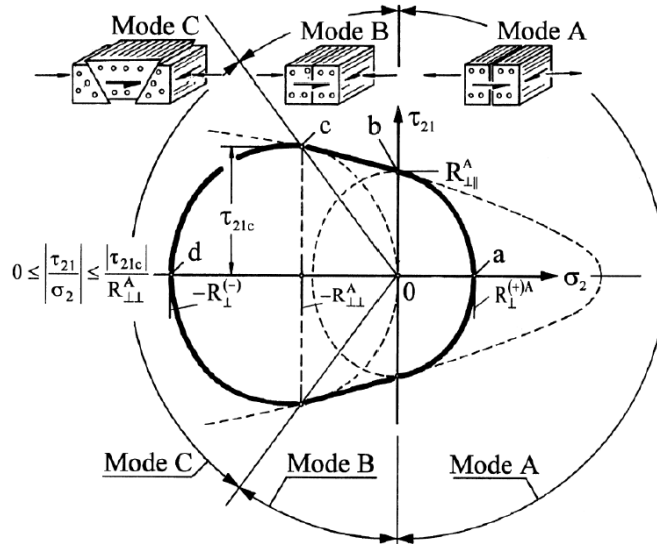
Figure 3.9. The fracture curve for inter-fiber failure mechanism with illustrations of the three different inter-fiber fracture modes A, B, C. (Source: Puck et al., 1998)
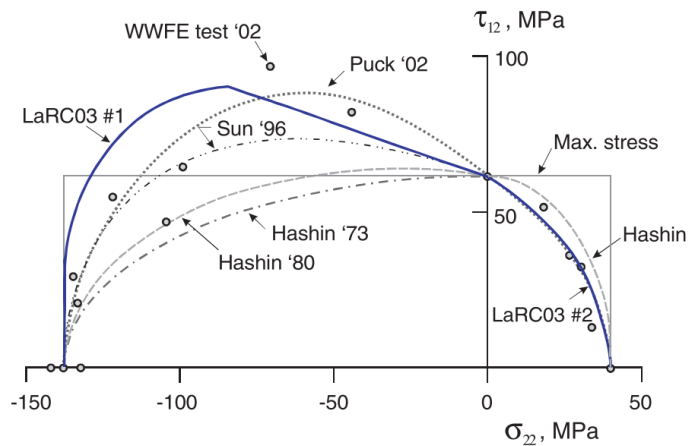
Figure 3.10. Comparison of several composite failure theory envelopes with experimental data for a unidirectional fiber reinforced composite. (Source: Davila et al., 2005)

It can be seen in Figure 3.10 that the failure envelope the Hashin theory fits well with the experimental data. Hashin failure theory provides two crucial feature for the FE analysis of this study; the ability to identify the failure modes which is required by the progressive damage analysis and the number of additional constants, which some of them related with the mechanical properties, introduced with the theory is minimum compared to more advanced theories such as Puck's failure or LaRC03.

3.3.2. Damage Evolution

As mentioned before the concepts of failure and damage for composite materials is complicated compared to conventional materials. The prediction accuracy of the composite failure theories greatly varies with different cases of the orientation of the laminates, the loading conditions and the boundary conditions. Therefore, a universally accepted failure does not exist. For specific cases, several ply failure theories can dictate the final failure of the structure, but this strategy may result in over safe design and increase the material costs of the composite structure. So, it is safe to assume that the load-bearing capability of a laminated composite continues even after the first ply failure.

The implementation of the progressive failure method to the analysis is pivotal when considering the damage evolution of the fiber reinforced polymer matrix composites. The following sections are dedicated to different damage evolutions methods that are widely used in the literature.

3.3.2.1. Ply Discount Method

The ply discount method reduces the stiffness properties of a ply when a damage onset occurs on the respective ply of the laminated composite. With this method, the ply is assumed to reach the final state of damage immediately instead of any evolution of damage. Several applications of this method include the total reduction of ply stiffnesses to zero and limited ply discount emphasizing only relevant moduli set to zero, depending on the failure mode.

3.3.2.2. Material Property Degradation (MPDG)

A simple progressive damage analysis method also called as material property degradation method was introduced for damage evolution in composite laminates.

For this model, a damage parameter which is expressed in terms of the degradation factor, d, is introduced. The degradation factor specified as 1 for the undamaged condition and 0 for the complete loss of material properties. Following the onset of damage,

material stiffness reduction occurs immediately. The reduction amount can be given in the range of 0 to 1. The constitutive relationship for a damaged material is given as in (3.22, where σ is the effective stress and ε is the total elastic strain.

$$\sigma = [D]_d \varepsilon \tag{3.22}$$

The damaged stiffness matrix ($[D]_d$) can be expressed as in (3.23 for a transversely isotropic thin composite material in-plane stress state.

$$[D]_d = \frac{1}{A}\begin{bmatrix} (1-d_f)E_f & (1-d_f)(1-d_m)v_{21}E_f & 0 \\ (1-d_f)(1-d_m)v_{12}E_f & (1-d_m)E_m & 0 \\ 0 & 0 & A(1-d_s)G_{fm} \end{bmatrix} \tag{3.23}$$

Where A defined as in terms of undamaged Poisson's ratios (v_{12}, v_{21}) and the fiber and the matrix dominated damage variables, d_f and d_m, respectively ((3.24);

$$A = 1 - v_{12}v_{21}(1-d_f)(1-d_m) \tag{3.24}$$

Four damage variables (one for each failure mode) are utilized to measure the damage. The fiber and matrix dominated direction damage variables for calculating the damaged stiffness matrix are determined as in (3.25 and (3.26.

$$d_f = \begin{cases} d_{f,t}, & if \ F_{f,t} > 0 \\ d_{f,c}, & if \ F_{f,c} > 0 \end{cases} \tag{3.25}$$

$$d_m = \begin{cases} d_{m,t}, & if \ F_{m,t} > 0 \\ d_{m,c}, & if \ F_{m,c} > 0 \end{cases} \tag{3.26}$$

The shear damage variable d_s, depends on fiber and matrix damage variables and can be expressed as in (3.27.

$$d_s = 1 - (1-d_{f,t})(1-d_{f,c})(1-d_{m,t})(1-d_{m,c}) \tag{3.27}$$

3.3.2.3. Continuum Damage Mechanics (CDM)

Continuum damage mechanics considers the gradual degradation of mechanical properties rather than the immediate reduction that occurs in the material property degradation method (MPDG). Similar to the MPDG, once the failure occurs, the material

stiffness is controlled by damage variables that have values between states of undamaged (0) and fully damaged (1). The evolution law, thus the calculation of the damage variables is based on the fracture energy, which is the energy dissipated as a result of the damage. The approach may sensitive to the mesh structure and size. To eliminate this problem, the concept of characteristic length is introduced into the formulation during material softening. A linear elastic material behavior prior to damage initiation is assumed, the negative slope after damage initiation is achieved by evolution of the respective damage variables.

A schematic representation of different degradation approaches is shown in Figure 3.11.[40] The simple progressive damage method indicated as instantaneous unloading reduces material properties close to zero. As a completely different approach, the constant stress model assumes that the damaged element will continue to carry its load at the failure but no additional loads. The real ply behavior is something between these two models. Hence, models that use different gradual unloading approaches have been and still being developed.
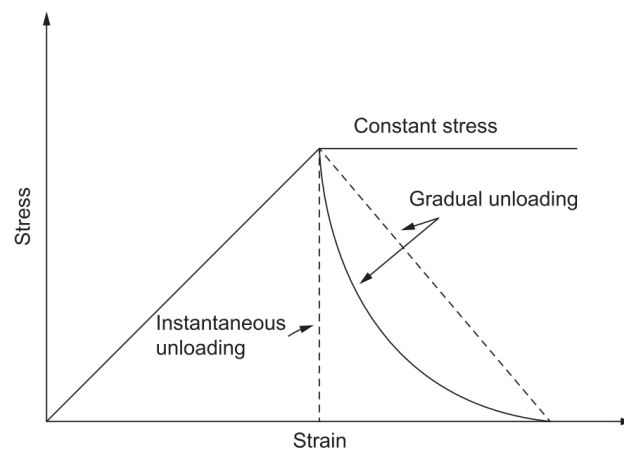
Figure 3.11. A schematic representation of different degradation rules.
(Source: Marulo et al., 2017)

Then, to consider progressive failure, simple degradation models with an immediate reduction in properties are easy to implement and only requires a failure criterion. Nevertheless, this damage evolution approach may not predict the ultimate failure correctly for some instances. An energy-based degradation approach is more realistic, but the determination of degradation parameters is considerably difficult, which requires fracture toughness testing, and the model can be too complicated to be implemented into a FE code.

CHAPTER 4

COMPOSITE OVERWRAPPED PRESSURE VESSELS

Composite overwrapped pressure vessels (COPVs) have been considered as one of the most effective solutions for high-pressure gas storage.[13,41] COPVs have attracted considerable attention for potential applications such as onboard fuel tanks for vehicles and aerospace power systems. Also, they offer significant weight reduction up to 75% as compared to metallic pressure vessels for similar tasks.[42–44]

4.1. Types of COPVs

Currently, for high-pressure gaseous storage, COPVs may be categorized into five main types based on their performance and cost.[11,12] Type-I is all metal vessel and generally used for stationary applications. This type has the lowest cost but also the heaviest one. Type-II vessels consist of a metal liner with cylindrical section overwrapped with fiber reinforced composite. This type has higher costs then Type-I due to the composite section, but also it is lighter. Type-III vessels comprise of non-load sharing metal liner (generally aluminum) fully overwrapped by fiber reinforced composite. Type-IV vessels consist of polymeric-based liner instead of a metal one, for further weight reduction. Again, it's fully overwrapped by composite with utilizing helical and hoop filament winding process. Lastly, Type-V vessels do not contain any liner and consist only fiber reinforced composite. This type of vessels currently used for aerospace applications and its production is limited to a few companies. Figure 4.1 shows several examples to the aforementioned pressure vessel types.[13,45]

For high-pressure onboard hydrogen storage (with 350 bar or higher working pressures), Type-III (metallic liner fully overwrapped with composite) and Type-IV (polymer-based liner overwrapped with composite) vessels represent the most practical solution (weight per amount fuel stored) for many commercial onboard applications.[15] Figure 4.2 shows a commercial onboard application of Type-IV pressure vessel.
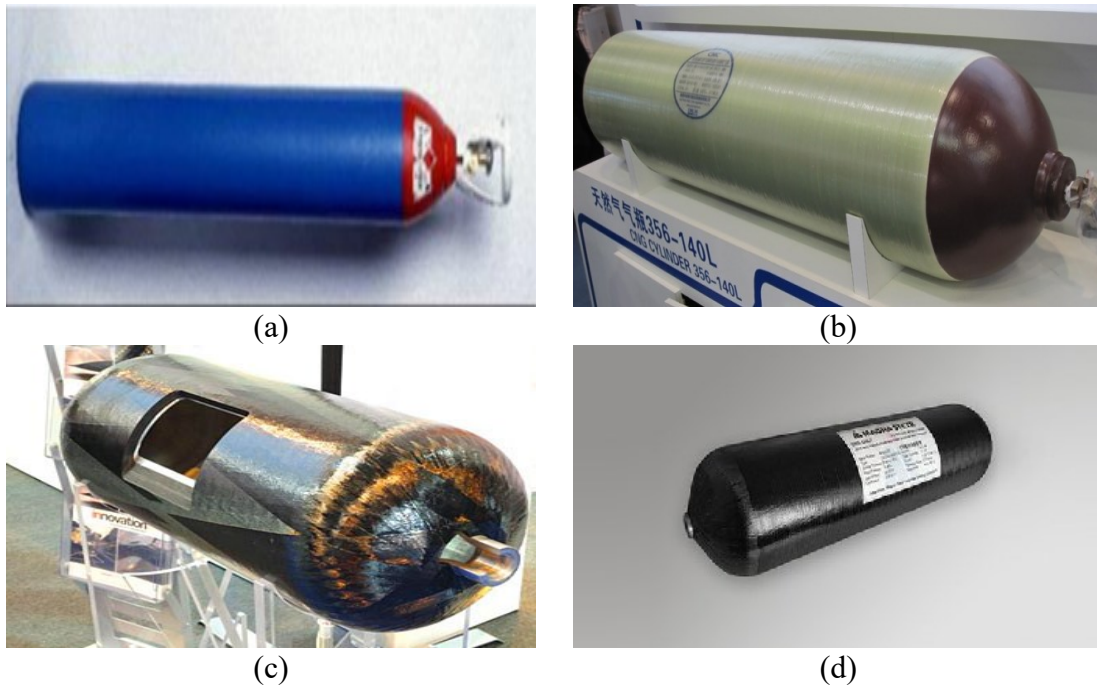
Figure 4.1. Several examples for each classification of high-pressure gaseous pressure vessels (a) Type-I, (b) Type-II, (c) Type-III, (d) Type-IV (Source: Barthelemy, 2012)

Figure 4.2. Composite overwrapped pressure vessel placement on a commercial vehicle.

4.2. Manufacturing of COPVs by Filament Winding Technique

Filament winding is a composites manufacturing process which primarily suitable for open or closed-end cylindrical structures such as large pipelines, power shafts, T and L tubes, bicycle rims, missile casings, aircraft fuselages, radomes and pressure vessels.[22] A schematic illustration of the process can be found in Figure 4.3.
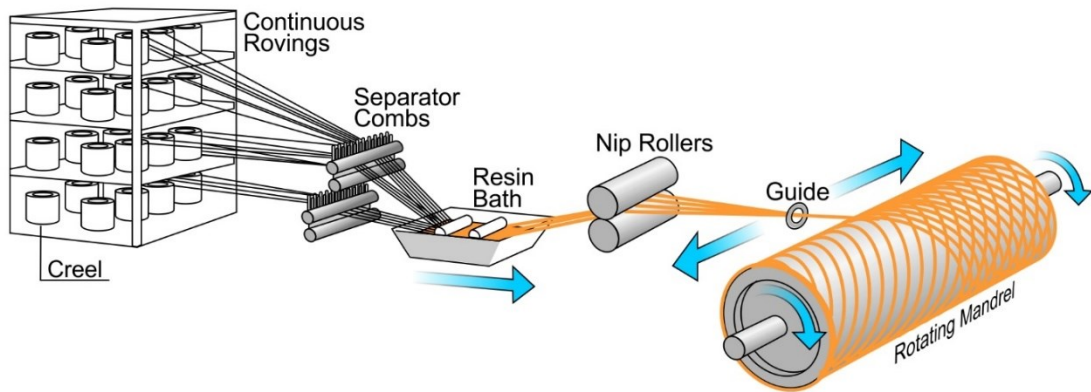
Figure 4.3. Schematic illustration of the filament winding technique

In this process, a mandrel is positioned horizontally or in some rare cases vertically between gripping supports followed by the winding of filaments over the rotating mandrel. Fibers are pulled out of the creel with the help of the rotating mandrel. To improve the fiber fraction ratio and thus the mechanical performance of the composite, fibers are generally tensioned utilizing a tensioner apparatus. Fibers are guided through separator combs to prevent any entanglement between the fiber tows. Then the fibers are submerged into a resin bath and wettened. Nip roller apparatus that is capable of finely tuning the distance between the cylinders are employed to control the excess resin on the fibers. After nip rollers, fibers arrive at the carriage which has 2 to 12 axes of motion. With the digitally controlled movements of the carriage and the rotating mandrel, winding angles and patterns can be configured and place the fibers which are finally guided by an eye or guide, onto the mandrel in a previously determined path.

The path of the fibers may be geodesic, semi-geodesic, or completely non-geodesic. The predetermined path type dramatically affects the composite buildup on the mandrel; thus, the mechanical behavior of the vessel. It is also important to note that due to the geometry of the mandrel, not all path types may be available for winding, thus creating fiber friction and slippage issues, especially in the case of non-geodesic winding.

Capabilities of the carriage or in recent years, a robotic arm create opportunities for different types of winding. Hoop or circumferential winding achieves nearly 90° of winding through the mandrel. This type of winding considerably improves the strength over the cylindrical section of the structure. The downside of the hoop winding is that it is only applicable to the horizontally straight surfaces. In contrast, lower angles involve in the helical winding. This type of winding yields to longitudinal reinforcement, which is dependent on the angle. Lower angles contribute to greater axial strength of the structure. Similar to helical winding, polar winding involves only very low winding

42

angles. These low angles achieved by the winding of fibers tangential to the polar regions of the vessel. Illustrations for the winding types is shown in Figure 4.4.
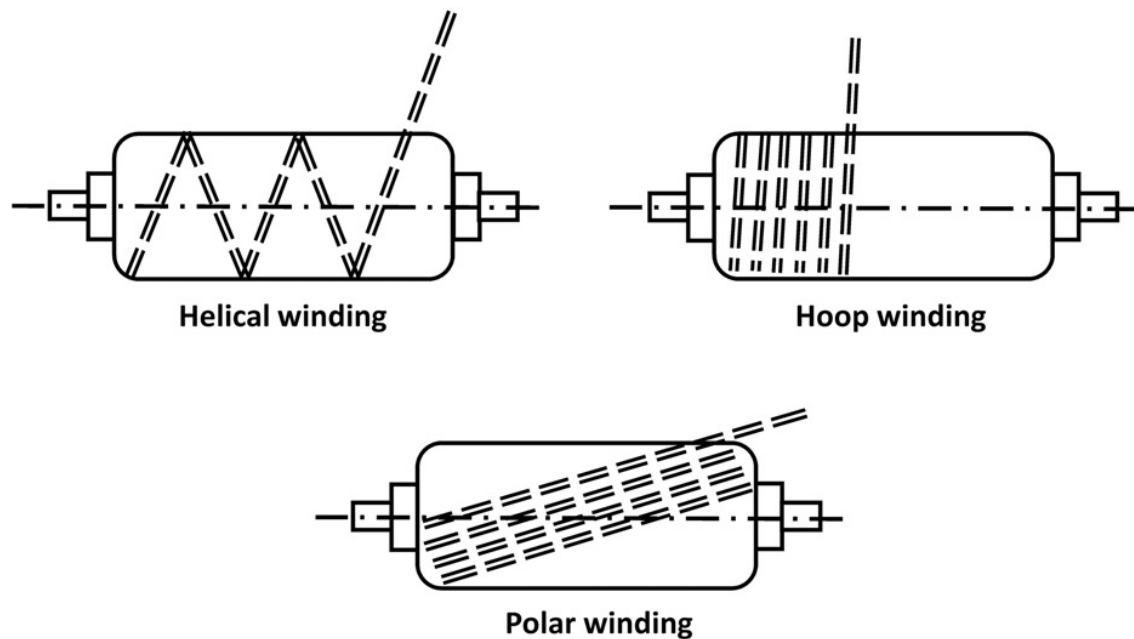
Figure 4.4. Illustrations for filament winding patterns.

Besides the abovementioned wet winding, towpreg winding employs pre-impregnated continuous tows as instead of wettened fibers. Towpregs eliminate the necessity for wettening, thus removing the need for a resin bath. This type of winding extensively improves the control over the process due to higher friction between the surface, higher and uniform fiber volume fraction and bandwidth. Hence resulting in high-quality products.

Curing is the final step of the filament winding manufacturing technique. The vessel overwrapped with wet or towpreg fibers is placed in an oven and suitable curing for the matrix material was applied. It is essential to rotate the vessel during curing for resin homogeneity over the whole structure.

This process can be highly automated and repeatable, thus resulting in high production rates.

Considering the case of COPVs, the abovementioned mandrel can be metal or plastic and named as *the liner*. So, the mandrel or the liner itself becomes the part of the composite structure in Type-III and Type-IV vessels. Unlike other types of vessels, in Type-V vessels, water-soluble or removable liner material is employed in the filament winding process and then removed afterward. Thus, eliminating the load sharing and fluid containing the ability of a liner.

4.3. Additional Reinforcements to the COPVs – Doily Layers

In addition to the helical and hoop plies overwrapped by the filament winding process, doily layers were utilized to reinforce the front and the aft dome sections of the vessels to reduce the total usage of carbon fiber and to improve the burst pressure performance.[46–48] Since it is not possible to wind hoop layers on the end domes directly by filament winding technique, an additional layer either a unidirectional or woven fabric are placed on the end domes.[49]

Due to the geometry of the vessels, the end domes are known to prone to manufacturing issues such as thickness variations. They are also known to be the weakest region of a vessel from a mechanical standpoint. The doily layers are basically *patches* of carbon fiber (CF) placed accordingly at the dome sections as a local reinforcement. the doilies are inserted between helical layers over the dome in order to provide extra strength in the circumferential direction. The dome is reinforced along the longitudinal direction as well as the circumferential direction if woven fabrics are utilized. As a result, the need for helical layers is reduced, and so, the total amount of CF usage is also reduced. If the liner geometry is not optimized for reducing the stress at the end domes and the geodesic winding, utilization of the doily layers may immensely increase the burst performance of the COPV.

However, the utilization of doily layers as local reinforcements to the critical sections of the COPVs has not been adopted by the COPV manufacturers, due to concerns of automated manufacturability and potential delamination that may be caused by the doilies over cyclic loadings.[47]
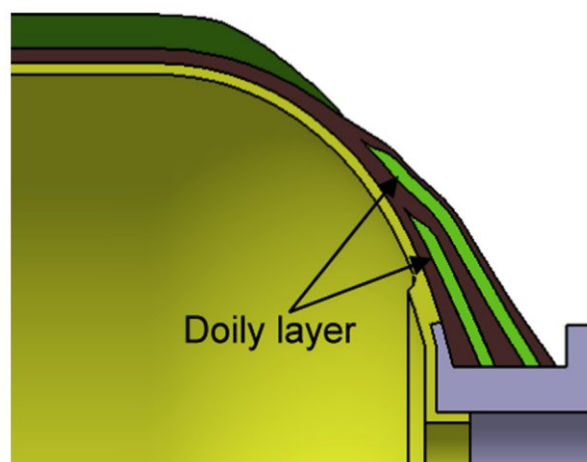
Figure 4.5. Schematic representation of doily layers as a local reinforcement for the front dome and boss region of a COPV. (Source: Roh et al., 2013)

4.4. Analysis of the Neat Liners

In order to predict the burst pressure of a vessel, material properties and elastic-plastic models must be determined precisely with an experimental validation if possible. Material models for the plastic region of pressure vessel material gain great importance, mainly after maximum load attained (post-necking). Several studies reported in the literature involved different ductile metals. Ling (1996) proposed a post-necking plastic behavior model for various alloys and compared it with power law using FE analysis. A similar approach was followed by Yao et al. (2016) for SAE 304 steel and acquired model were applied to different alloys for successful prediction of failure strains for a custom tensile test.[50]

The tensile behavior of ductile steel (34CrMo4), which is widely used for pressure vessels was studied through tensile testing of vessel material and FE analysis.[51] A geometric defect implemented through FE software and Gurson-Tvergaar-Needleman (GTN) model was used for ductile fracture initiation for 34CrMo4 steel. Experimental data used for evaluation of GTN model parameters and parametric study has been done for geometric defect size. Geometrical imperfections implemented through FE software for a circular casing were also studied.[52] The reliability of the predicted burst pressures of the circular casing was validated through a comparison with a series of experimental burst test data. Post-necking tensile behavior of steel was studied utilizing digital image correction (DIC) experimental setup and plastic model, including post-necking region, was correctly estimated for commercial ferritic steel and dual-phase steel.[53] During metal forming and other processes involving large deformations, resulting metal may exhibit a weak anisotropy. This phenomenon was studied through experiments and FE analysis to obtain the proper material response of Al-6061-T6 at larger strains.[54] With a DIC system that is capable of measuring local strains, tensile and disk compression tests data were used for the validation of several anisotropic yield models and it is reported that yield function acquired from Barlat et al. (2005) demonstrated most accurate behavior to experimental data.[55]

Constitutive modeling and burst pressure predictions for tubular structure and pressure vessels were also studied for various alloys including widely used Al-6061-T6 and mild steel.[56–58]

4.5. Analysis of COPVs

ISO/TS 15869:2009 defines requirements and safety factors for each type of pressure vessel to be used in onboard applications.[59] Thus, it is very critical to analyze and determine the burst pressure and damage initiation mechanisms of COPVs for safety and cost reasons. Therefore, there are several studies in the literature, which have studied the burst pressure and damage developments of COPVs with distinct approaches.

Hocine et al. developed an analytical model for stresses and strains on the cylindrical section of the hydrogen storage vessel. The model was validated by testing the vessels experimentally.[60] Shao et al. produced high-pressure vessels with epoxy and vinlyester matrices with carbon fiber reinforcements. Vessels were loaded with internal pressure up to burst pressure. Deformations during loading were measured with strain gages and digital image correlation (DIC) techniques.[61] The influence of filament winding parameters and the fiber volume fraction on the strength of COPVs were studied by Cohen (1997), and Cohen et al. (2001) respectively. The studies indicate that manufacturing parameters such as laminate stacking sequence, winding tension and winding time significantly affect the final burst pressure of the vessel.[62,63]

The finite element analysis (FEA) is one of the most efficient and robust numerical methods to predict the burst pressure and damage evolution properties of the COPVs.[64] Implementing a progressive failure analysis on the COPVs provides an accurate prediction for the damage initiation and burst pressure.[65] Leh et al. developed two distinct progressive failure finite element model for the hydrogen storage vessel burst. The first model is fully adapted to low computation time for future optimization trials. The second model contains only solid elements and promotes higher accuracy on the stresses.[66] They also defined safe and unsafe burst modes for COPVs. The safe burst mode occurs in the cylindrical section, without any ejection of the liner or boss material during the burst. On the contrary, the unsafe burst mode occurs at dome sections of the vessel with the ejection of the liner or boss material. The detection of these modes during FEA is essential for safety reasons, as unsafe burst modes should be avoided at all costs. Xu et al. proposed a 3D finite element model to predict the burst pressure and damage evolution of the COPV with increasing internal pressure.[67] The effect of several different failure criteria including the maximum stress, Hoffman, Tsai-Hill and Tsai-Wu, on the burst pressure of COPVs were investigated. It was reported that the Tsai-Wu failure criterion yielded the most

accurate burst pressure for the cylindrical composite structures. Alcantar et al. developed two different approaches for weight minimization of hydrogen pressure vessels, which are genetic algorithms and simulated annealing. They proposed an objective function featuring the Tsai-Wu failure criterion, composite ply thickness with the addition of a safety factor, and finally, a penalization factor.[68] Kim et al. proposed design algorithms for filament wound vessels under internal pressure. They developed a semi-geodesic path algorithm, a progressive failure damage model, and a modified genetic algorithm for optimization.[69] Thickness and fiber angle variations on the dome section due to the filament winding process are critical for determining unsafe burst modes. Park et al. predicted winding patterns by utilizing a semi-geodesic fiber path equation. In that way, they were able to calculate the difference of the fiber angle and thickness on helical wound layers. FEA performed considering these factors, and geometrical nonlinearities were verified with experimental data.[70]

Almeida et al. investigated the load sharing ability of steel and aluminum liners in Type-III COPVs. A FE model considering nonlinear geometry was developed, and a parametric study on the effect of liner thickness on 4 different cases (bare aluminum and steel liners with their fully composite overwrapped counterparts) were performed. The study revealed that metal liners might share the load on COPV with decreasing effectiveness while increasing internal pressure. Also, the mechanical behavior for different regions of a COPV was observed within the internal surface of the liner by utilizing the FE model and realization of von-Misses stresses along the internal surface.[71]

It is further possible that the hybridization of glass and carbon fibers may contribute to the performance/cost of COPVs for high-pressure storages. Studies on the hybridization of composites began as early as in the 70s due to their high stiffness and cost of then-recently found carbon fibers.[72] The hybridization of continuous fiber reinforced composites can be divided into 3 categories; (i) interlayer/interply (layer-by-layer), (ii) intralayer (yarn-by-yarn), (iii) intrayarn (fiber-by-fiber). The application of interlayer hybridization to COPVs is effortless due to the layer-by-layer nature of the filament winding manufacturing. Mahdi et al. investigated the effect of hybridization on the crushing behavior and energy absorption of filament wound composite cylinders.[73] Various orientations of carbon and glass interlayer hybrid composites were examined, and it was found out that failure modes were significantly influenced by the hybridization. The glass-carbon-glass alternating combination displayed high energy absorption among all configurations. Kobayashi et al. performed a burst strength evaluation of composite

pipe filament wound with high and low modulus carbon fibers.[74] A numerical analysis was conducted for burst strength prediction with a maximum strain criterion employed as a first ply failure theory. It was reported that analytical burst strength predictions were consistent with experimental results. Gemi studied low-velocity impact response of interlayer hybrid filament wound hybrid composite tubular structure.[75] A parametric study was performed on the effect of stacking sequence of glass and carbon layers on the damage formation. That study revealed that carbon-glass-glass stacking represented higher impact resistance while glass-carbon- carbon did not show any leakage. Similarly, Prusty et al. studied the effect stacking sequence on flexural behavior of interlayer hybrid composites.[76] Among several proposed stacking sequences, 7 layered hybrid composite with 2 carbon/epoxy plies at the two end surfaces (C2-G3-C2) performed comparable to full carbon/epoxy composite (C7), having 93% of modulus and 96% strength of the latter. It was also noted that the presence of carbon/epoxy plies at the tensile side of the flexural specimen leads to enhanced strength and modulus at the expense of being prone to catastrophic failures.

To put it in a nutshell, modeling and manufacturing of Type-III COPVs, the following topics have generally been considered in the literature: the elastic-plastic behavior of isotropic metal liner[51,71,77–80], the progressive failure analysis of composite section[65,81,82], the composite ply thickness and fiber angle variations on the dome sections due to the nature of filament winding manufacturing technique[68,70,83], the determination of safe and unsafe burst modes based on burst failure locations[66], the validation of the numerical model with experimental data[84,85]. In addition to the aforementioned features, composite hybridization effects of filament wound cylindrical structures were studied in the context of burst pressure, low-velocity impact, and flexural behavior. However, in the case of COPVs, any investigation of the interlayer hybridization effect on final burst pressure of the vessel seems to be absent in the literature.

CHAPTER 5

EXPERIMENTAL PROCEDURES

5.1. Materials

1200 tex FWR6 glass fiber filaments provided from Şişe Cam Inc. (Turkey), 800 tex A-49 carbon fiber filaments provided by DowAksa Inc. (Turkey), and 800 tex T700SC-12K carbon fiber filaments purchased from Toray Industries, Inc. (Japan) were used as fiber reinforcement materials.

A three-component, high-temperature cure epoxy system from Huntsman Inc. was selected as the matrix material in this study. This epoxy system includes Araldite MY740 epoxy resin, Aradur MY918 curing agent, and DY062 accelerator.

34CrMo4 steel liners with an average wall thickness of 4 mm were purchased and used for manufacturing of COPVs. The geometry of the steel liner is shown in Figure 5.1.
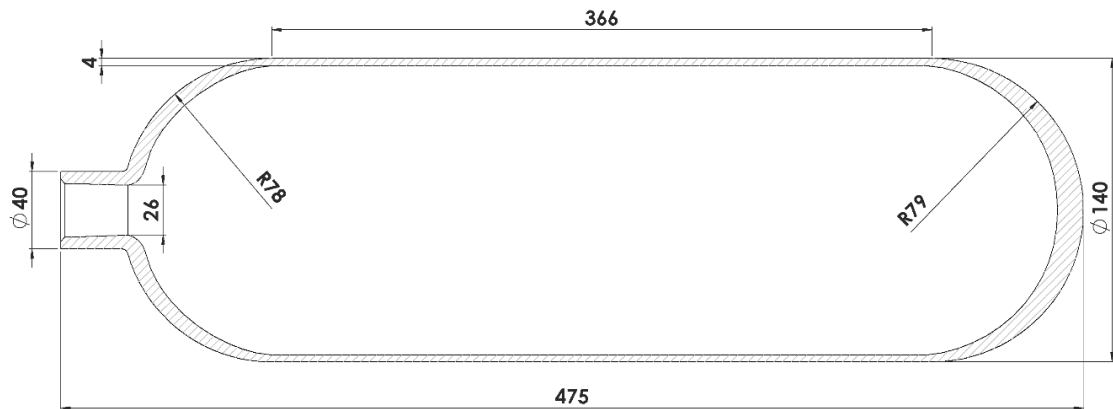
Figure 5.1. The geometry of the metallic liner (dimensions are in mm)

The aluminum vessels were supplied by a local manufacturer based in Kocaeli, Turkey. These vessels were made of Al-6061-T6 and internal volume capacity is about 5 L. These vessels are also suitable as a liner for composite overwrapped pressure vessels (COPV). Figure 5.2 shows the dimensions of the vessel. The 3D models for the liners were also created for FE analysis software.

It is important to note that these liners were already commercially available products. The vessels did not undergo any geometry optimization for filament winding

manufacturing or high-pressure storage at all. This condition forced the manufacturing of COPVs to non-geodesic filament winding manufacturing and restricted the manufacturing to limited angles and introduced slippage during helical winding.
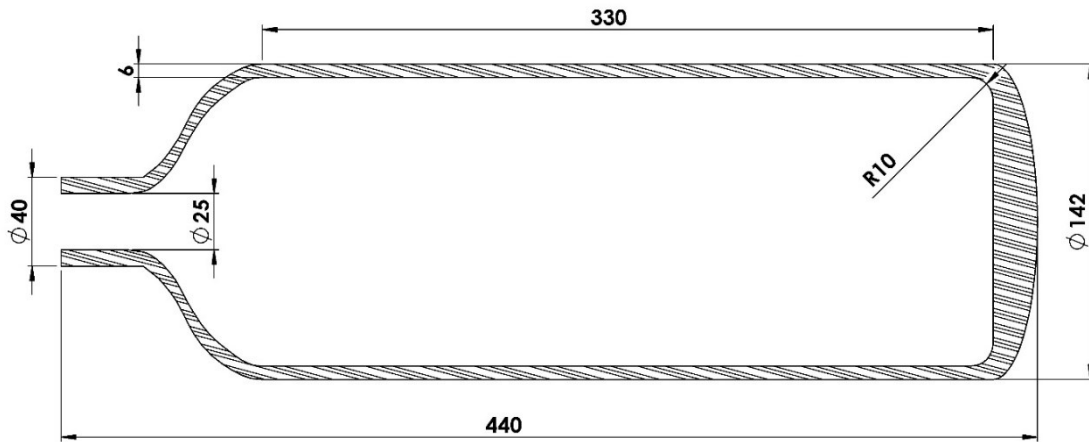
Figure 5.2. Technical drawing of purchased Al-6061-T6 vessels

5.2. Determining the Mechanical Properties of the Materials

In order to determine the mechanical properties of the aluminum liner, tensile tests were performed according to ASTM E8/E8M – 16a standard.[86] For this aim, tensile test specimens were cut from the vessel by using a water jet. Figure 5.3 shows the representative specimens obtained directly from the metal liners or the filament wound composite plate.

The true stress and strain data after yielding is needed for determining the plastic behavior of Al 6061-T6. The bilinear tangent modulus and the tabulated data for multilinear behavior after the yielding are needed as inputs for ANSYS software package. For that, experimentally acquired engineering stress-strain curves were converted into true stress-strain data up to necking point, assuming uniform deformation occurs up until that point.

In addition to the properties of the metal liners, the mechanical properties of the composite section are essential for the COPV modeling. For this aim, unidirectional (UD) carbon/epoxy plates were manufactured by filament winding technique to simulate identical conditions as in COPV manufacturing. then the plates were cured (Figure 5.4).

(a)

(b)

(c)

(d)
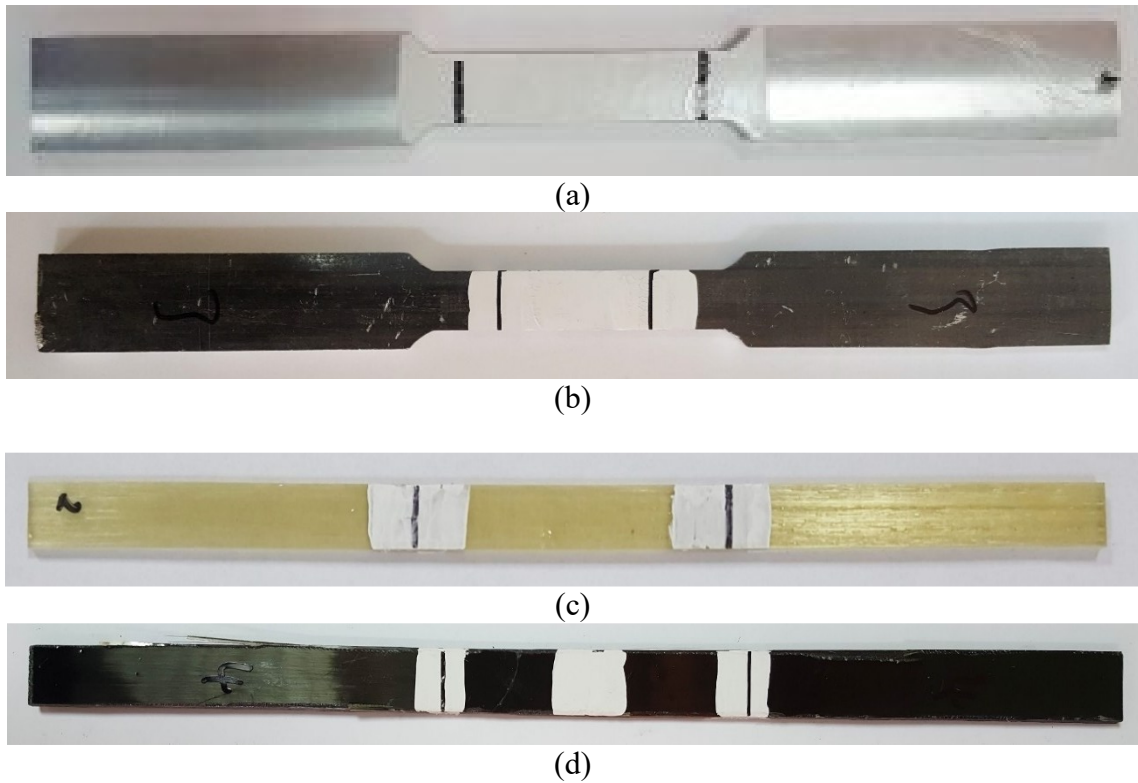
Figure 5.3. Representative tensile test specimens. (a) Directly obtained from Al liner, (b) obtained from Steel liner, (c) glass fiber / epoxy specimen from GF FW composite plate, (d) carbon fiber / epoxy specimen from CF FW composite plate.
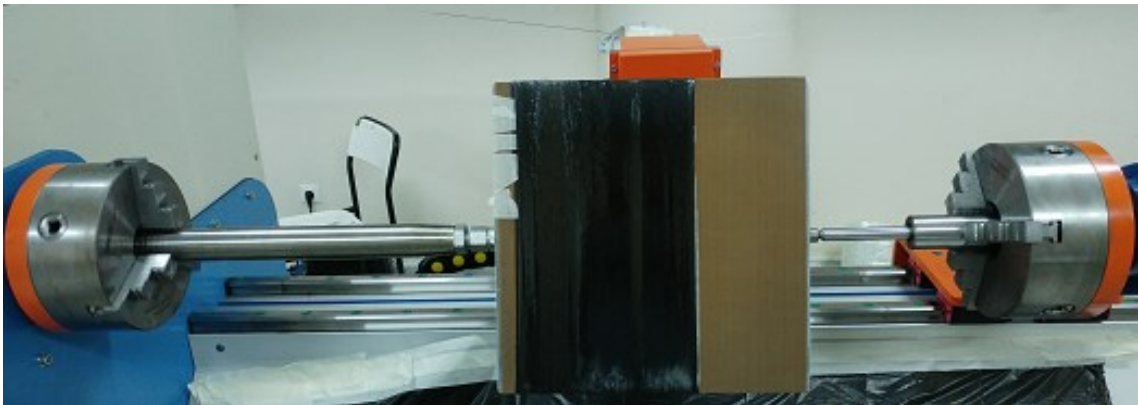
Figure 5.4. Composite UD plate manufacturing by filament winding technique.

Tensile testing in accordance with ASTM D3039-17 was conducted to the specimens obtained from the filament wound plate. To obtained fiber dominated direction properties, specimens aligned with longitudinal direction with dimensions of 150x15 mm were cut utilizing a diamond saw.

The universal testing machine, Shimadzu AG-IC 100KN were employed for all mechanical testing of the materials involved in this study. All tests were conducted at room temperature and the crosshead speed was set to 2 mm/min in conformity with the

relevant standards. At least 5 samples were tested for each material type. The specimens that was gripped between the tensile grips of the universal testing machine during the tensile testing is shown in Figure 5.5.

<div align="center">(a)   (b)   (c)</div>
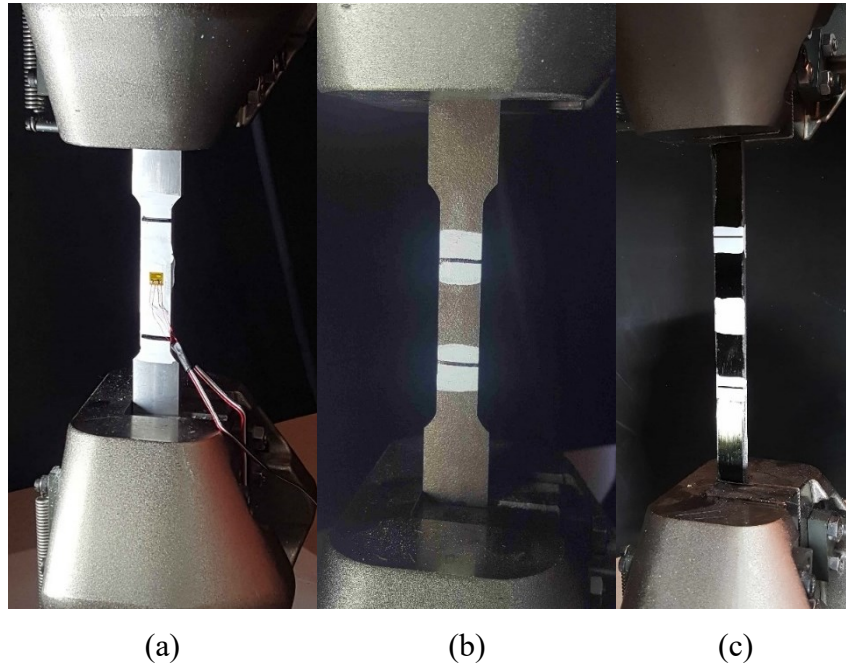
Figure 5.5. The specimen placement during tensile testing.

Tensile stress and strain values were calculated based on the following equations;

$$\sigma = \frac{F}{A} \hspace{3cm} \text{Eqn. 5.1}$$

$$\varepsilon = \frac{(L - L_0)}{L_0} \hspace{3cm} \text{Eqn. 5.2}$$

In the Eqn. 5.1 and Eqn. 5.2, F denotes the maximum load carried by the specimen, A is the cross-sectional area of the specimen tested, L_0 is the initial displacement between video extensometer gauge markings and L is the instantaneous distance between gauge markings. Elastic modulus (E) of the materials was obtained from the initial linear region of the stress-strain curves.

5.3. Determining the Fiber Weight and Volume Ratio for Composites

The fiber weight and volume ratio of the polymeric composite reinforcement in the COPVs were measured by acid digestion of cured resins in accordance with ASTM D3171-15 Test Method I – Procedure A. Three different samples obtained from distinct

locations were analyzed. In this method, about 1 gram of the sample from composite structures was cut and dissolved in a nitric acid solution (Figure 5.6). The fiber residue was weighted after the evaporation of the nitric acid solution. With the known densities of the fiber and the matrix phases, weight fractions can be converted to the volume fractions by utilizing Eqn. 5.3.

$$V_f = \frac{v_f}{v_f + v_m} = \frac{\dfrac{m_f}{\rho_f}}{\dfrac{m_f}{\rho_f} + \dfrac{m_m}{\rho_m}} \qquad \text{Eqn. 5.3}$$

In this equation, v, m and ρ denote the volume, the weight and the density of the measured phases, respectively. Subscripts f and m indicate the fiber and the matrix phases, respectively.
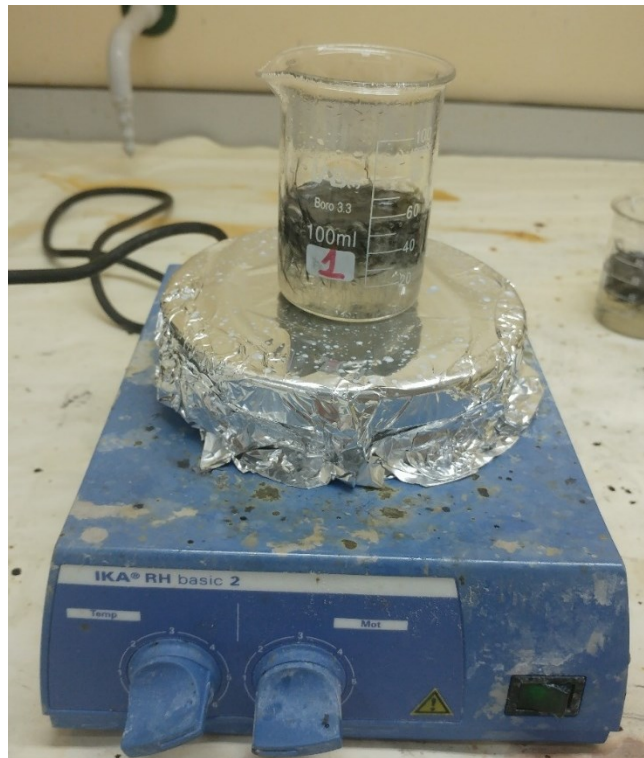
Figure 5.6. Carbon fiber / epoxy composite was dissolved in an acid solution for determining the fiber volume fraction.

5.4. Manufacturing of COPVs

The COPV's helical and hoop composite layers were manufactured by a filament winding machine, as shown in Figure 5.7. One roving was utilized to overwrap the steel liner with a roving bandwidth of 4 mm for glass fiber and 5 mm for carbon fiber.

Furthermore, in order to ensure that the steel liner was fully overwrapped with a composite section, 105% degree of coverage was selected, utilizing CADWIND CAM software.[87]

(a)
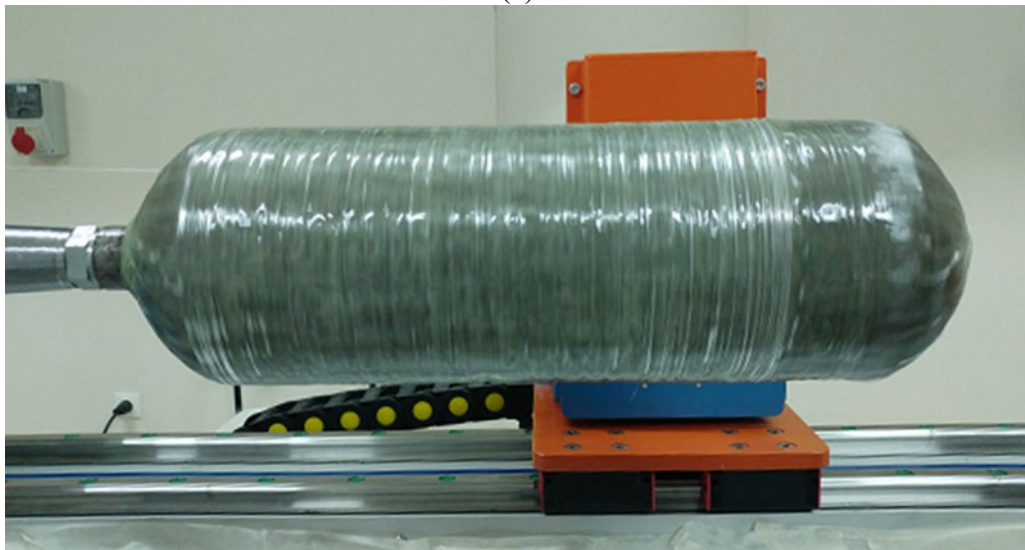
(b)

Figure 5.7. The winding of (a) a helical layer and (b) a hoop layer over the metallic liner by the filament winding equipment.

Preliminary winding simulations performed with CADWIND software have demonstrated that the asymmetric nature of the liner on the axial direction (the open-end front dome vs. the closed-end back dome) creates manufacturing restrictions on winding angle. It was observed that, for this specific liner geometry, only $\pm11^\circ$ helical winding angle could achieve complete coverage of both front and back dome sections of the liner. Due to this manufacturing restriction, the winding angle of the helical layers was chosen

as $\pm 11^\circ$ in order to achieve a fully overwrapped pressure vessel. It was agreed upon the fact that at least three helical and three hoop layers were needed to differentiate the effect of composite layers over the steel liner. Two different types of COPVs were manufactured for investigation of hybridization effect of glass and carbon fibers. The first type consisted of only glass fibers as a fiber reinforcement material. For the second type, carbon fibers were incorporated as hoop layers over the glass helical layers to create hybrid COPVs. Stiffer carbon fiber / epoxy layers implemented to create a positive hybridization effect for improving the burst pressure of the vessel. CF/Epoxy reinforced the liner at the cylindrical region, as the burst failure of the COPVs were expected at the cylindrical region of the vessel.

In hybrid COPVs, composite layers consist of two hoop layers of carbon fibers on the inner section, three helical layers of glass fibers, and one hoop layer of glass fibers on the outermost section. Filament winding of the outermost helical layer of a pressure vessel as a glass fiber / epoxy layer is a common practice in manufacturing of COPVs for increasing impact and corrosion resistance.[79,88,89] Winding configurations of manufactured vessels are summarized in Table 5.1.

Table 5.1. Configurations and final dimensions of steel liners and manufactured steel-based COPVs

Specimen	Matrix	Fiber Reinforcement	Layer Orientation	Total # of Plies	Avg. Diameter (mm)	Avg. Ply Thickness (mm)	Avg. Length (mm)
Steel Liner							
Prototype 1	-	-	-	-	140.25	-	474.50
Prototype 2	-	-	-	-	140.10	-	474.46
GF COPV							
Prototype 1	Epoxy	Glass Fiber	$[\pm 11^\circ/90^\circ_2]_3$	12	145.25	0.208	486.68
Prototype 2	Epoxy	Glass Fiber	$[\pm 11^\circ/90^\circ_2]_3$	12	145.03	0.199	482.93
Hybrid COPV							
Prototype 1	Epoxy	Glass Fiber / Carbon Fiber	$[\pm 11^\circ/90^\circ_2]_3$	12	146.24	0.250	481.81
Prototype 2	Epoxy	Glass Fiber / Carbon Fiber	$[\pm 11^\circ/90^\circ_2]_3$	12	145.46	0.217	484.79

After the winding process, composite vessels were cured at 80°C for 2 hours using a rotating shaft in a curing oven and post-cured at 120°C for 2 hours. A recently cured

glass fiber reinforced COPV in the curing oven with a rotating shaft is shown in Figure 5.8.
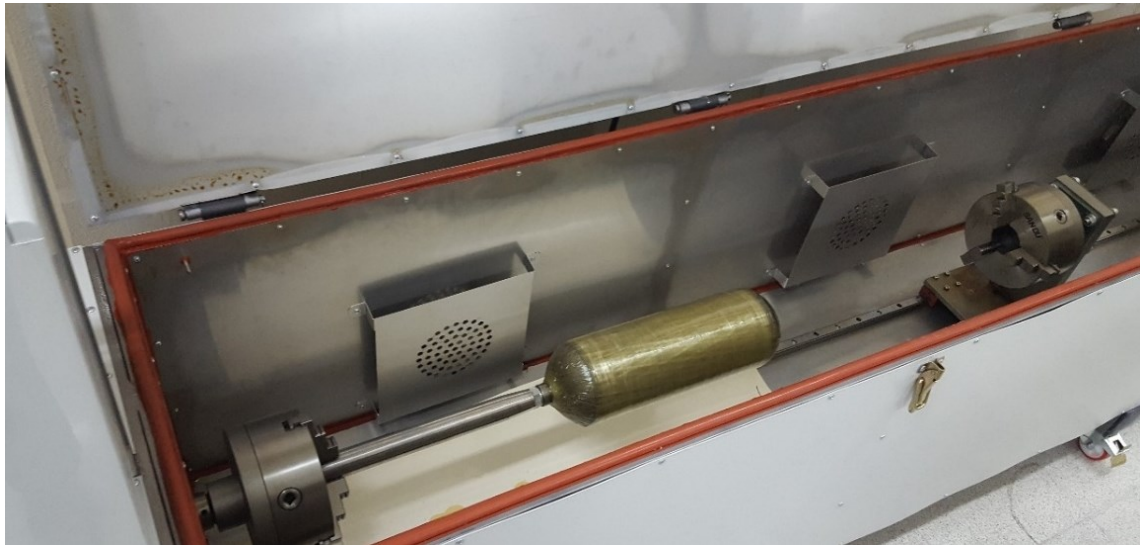
Figure 5.8. A manufactured COPV attached to the rotating shaft of the curing oven.

5.4.1. Manufacturing of Carbon Fiber Reinforced COPVs with Aluminum Liners

Prior to the filament winding process, winding simulations were done with CADWIND CAM software. After simulations, composite helical and hoop layers were winded over the aluminum liner with the filament winding machine, as shown in Figure 5.9. In order to decrease the winding time, three rovings were used with 4 mm width per roving for a total bandwidth of about 12 mm. Furthermore, in order to ensure that the steel liner was fully overwrapped with a composite section, 105% degree of coverage was selected in CAM simulation software. ±14° helical winding angle was selected because the simulations showed that only ±14° winding angle was able to cover the liner completely.

The COPVs, which consist of different number of layers and orientations, were manufactured. Effect of the number of doily layers, helical and hoop layers on the burst pressure of COPVs was investigated. The preliminary studies showed that all the COPVs were failed from the front dome section. Therefore, doily layers were utilized from the front dome section. The implementation of a doily layer to the front dome of the vessel were shown in Figure 5.10. After the winding process, composite vessels were cured at

80°C for 2 hours using a rotating shaft in a curing oven and post-cured at 120°C for 2 hours.

Figure 5.9. The helical winding of aluminum-based COPVs with the filament winding machine.

Figure 5.10. Doily and Helical Layers of COPVs.

The layer orientations and the doily layer configurations of the manufactured COPVs were given in Table 5.2. It was also noteworthy to mention that over 30 prototypes were manufactured, but only 11 of them produced meaningful results. The liner that was manufactured elsewhere had changed several times and that was directly affected the results. In addition to that, the liner also has leakage problems, especially in internal pressures higher than 900 bar. This was due to the generation of microcracks in the liner under compressive loadings.

Table 5.2. Configurations of COPVs

Specimen	Layer Orientation	# of Front Doily Layers	# of Aft Doily Layers
ALCF 1	$[\pm 11^\circ]_9 / [\pm 90^\circ]_7$	-	-
ALCF 2	$[\pm 11^\circ]_9 / [\pm 90^\circ]_8$	-	-
ALCF 3	$[\pm 11^\circ]_{12} / [\pm 90^\circ]_{11}$	-	-
ALCF 4	$[\pm 11^\circ]_{13} / [\pm 90^\circ]_{11}$	-	-
ALCF 5	$[\pm 11^\circ]_9 / [\pm 90^\circ]_7$	7	-
ALCF 6	$[\pm 11^\circ]_9 / [\pm 90^\circ]_7$	11	-
ALCF 7	$[\pm 11^\circ]_9 / [\pm 90^\circ]_7$	15	-
ALCF 8	$[\pm 11^\circ]_9 / [\pm 90^\circ]_7$	17	-
ALCF 9	$[\pm 11^\circ]_9 / [\pm 90^\circ]_7$	17	5
ALCF 10	$[\pm 11^\circ]_9 / [\pm 90^\circ]_7$	17	9
ALCF 11	$[\pm 11^\circ]_9 / [\pm 90^\circ]_8$	17	9

5.5. Burst Pressure Testing

COPVs were subjected to hydrostatic pressure in order to determine the burst pressure. During hydrostatic tests, three rosette-type strain gages were used to measure the local hoop and longitudinal strains. The strain gages were located at 20 mm away from both ends of the hoop winding region with an addition of a strain gage at the center of the cylindrical section of the vessels. An illustration of hydrostatic burst testing specimens before testing with strain gages and strain gage rosette positions on the vessels are displayed in Figure 5.11. A photograph of actual specimens can also be found in Figure 5.12.
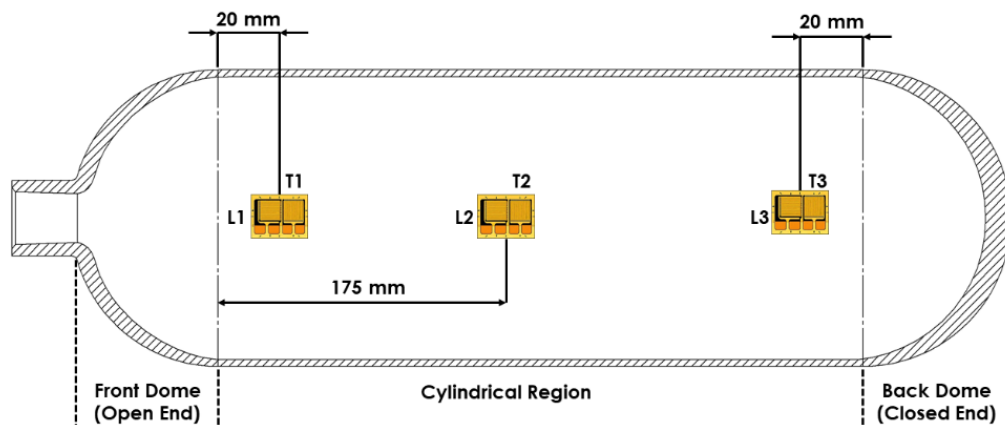
Figure 5.11. The schematic illustration of strain gage rosette positions on steel liner based COPVs.

Similarly, the burst pressure values of aluminum liners were determined by the hydrostatic pressure test. Internal hydrostatic pressure was applied to Al liners up to burst failure. During the burst pressure test, the local strain values at the surfaces of liners were measured by using strain gages. Three strain gages were used and radial and longitudinal strain values during burst pressure test were determined. The exact positions of strain gages were also given in the technical drawing (Figure 5.13). The photographs of the neat aluminum liner and the Al-based liner with carbon fiber reinforced COPV can be found in Figure 5.14 and Figure 5.15.The burst pressure test setup has a maximum test capacity of 2000 bar, and it can increase the internal pressure with an average rate of 5 bar/sec.
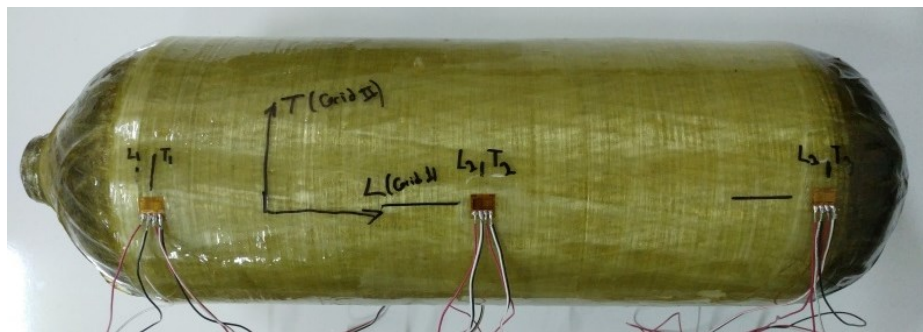
Figure 5.12. A photograph of the hydrostatic test specimen of steel-based glass reinforced COPV before testing.
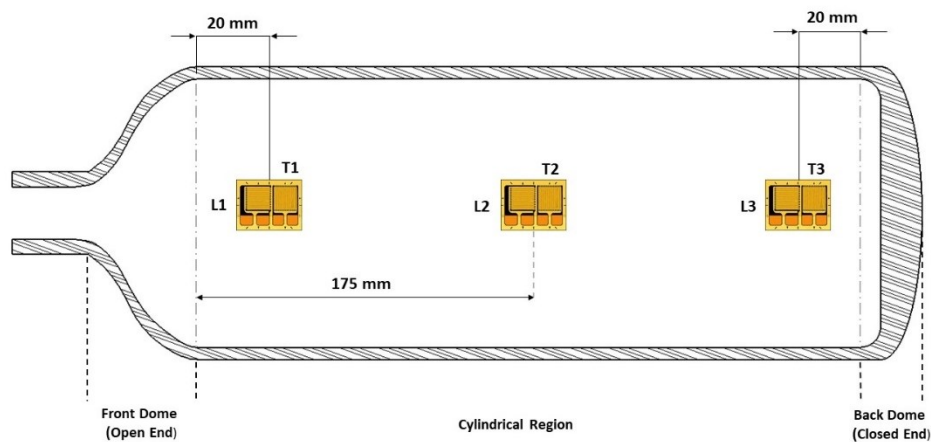
Figure 5.13. The schematic illustration of strain gage rosette positions on aluminum liner based COPVs.
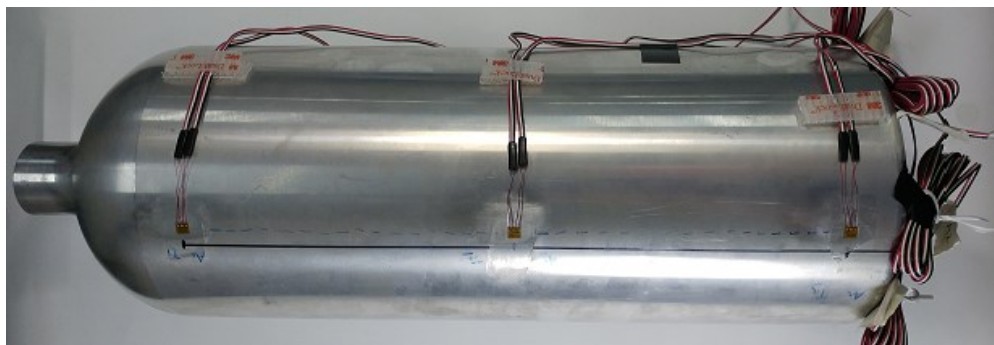
Figure 5.14. A photograph of the hydrostatic test specimen of the neat aluminum liner before testing

Figure 5.15. A photograph of the hydrostatic test specimen of Al-based carbon reinforced COPV before testing

CHAPTER 6

NUMERICAL MODELING OF THE PRESSURE VESSELS

6.1. Validation of the FE model

A 3D model was created from the dimensions measured from the water jet cut specimens for tensile testing. Grip regions were removed to avoid unnecessary inclusion of contact regions with universal testing machine grips and shear loading to the FE analysis. A mesh was formed from 20 node hexahedral elements with an average size of 3 mm. The resulting 3D mesh of the tensile test specimen model is shown in Figure 6.1. One end face on x-direction was defined as a fixed region. 10 mm displacement on x-direction was applied to the other end face on x-direction to observe the post-necking behavior of the tensile specimen (Figure 6.1).
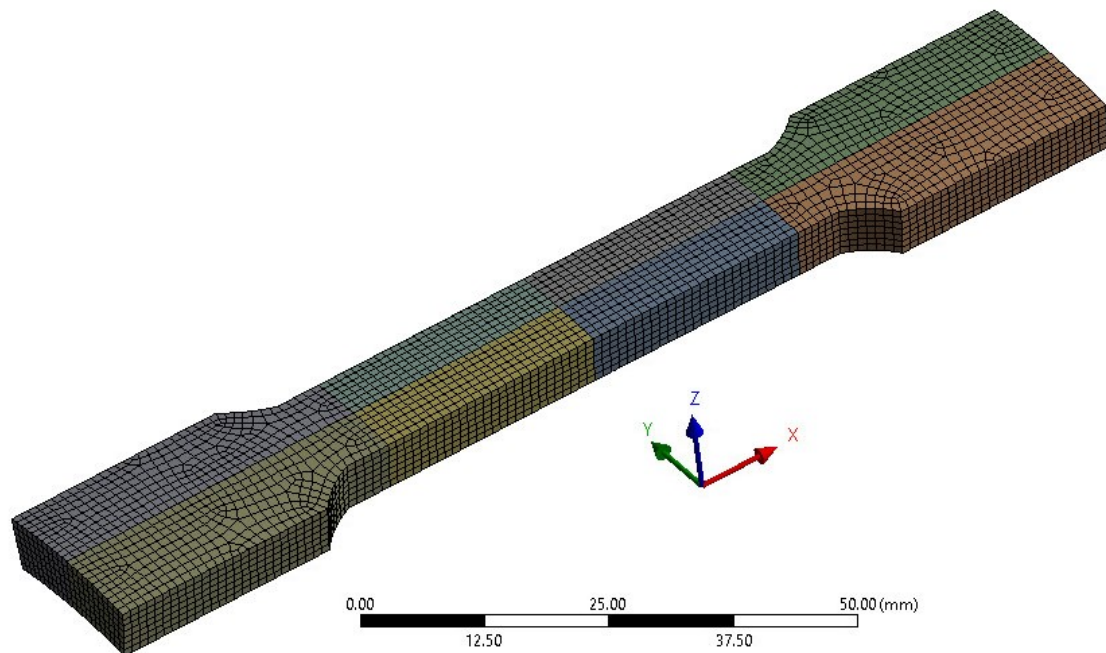
Figure 6.1. The tensile testing specimen FE solid model.

Al 6061-T6 material was defined as an elastoplastic material in ANSYS. Two different isotropic hardening models were utilized for defining the plastic region of the material, the bilinear and multilinear isotropic hardening. True stress – true strain behavior of Al 6061-T6 was acquired from the experimental tensile testing of the material

and by converting the engineering stress-strain curves up to the necking point. Calculated elastic modulus, yield strength and tangent modulus of the bilinear isotropic model was tabulated in Table 7.1.

Large deformations were expected as it was intended to observe the post-yielding behavior of the materials, so non-linear geometry setting was enabled in the FE analysis software. The displacement as the loading condition was applied linearly up until the final time of 1 second, which corresponds to 10 mm of displacement in the x-direction, with three different timestep regions. These timestep regions defined as 0.008 s up to 0.35 s, 0.001 s between 0.35 s and 0.58 s, and finally 0.0005 s until the last converged timestep. It was intended to gradually reduce the timesteps for improving the convergence of the numerical analysis and getting higher resolution of mechanical behavior through the loading.

6.2. Finite Element Analysis of Al Pressure Vessel

For pressure vessel FE analysis, a solid mechanical model was formed utilizing the aforementioned technical drawing (Figure 5.3) and 20 node hexahedral elements (SOLID185 in ANSYS). In order to decrease computational time and taking advantage of axisymmetry, a mesh convergence and a model reduction analysis were performed. The model was reduced to half, quarter and 1/16 of the full 3D model and shown in Figure 6.2.
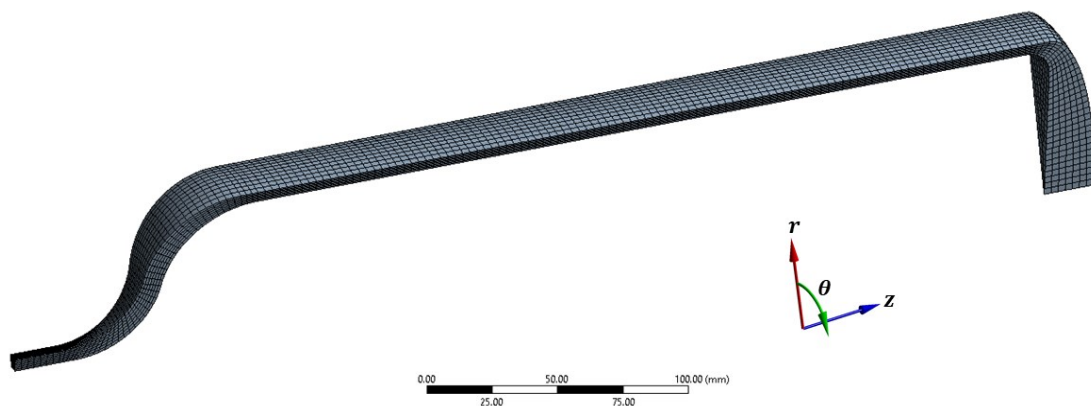
Figure 6.2. FE model of the Al liner with load and boundary conditions

Contact regions with testing apparatus were considered as fixed boundaries and shown in a. Except for the full model, reduced model's both side section boundaries were

given as free movement through axial and radial directions but restricted in the angular direction. Thus, it assumed that no rotational motion occurs through the vessel while internally pressurizing it. Lastly, the pressure was applied normal to internal surfaces of the pressure vessel except the regions in contact with the testing apparatus.
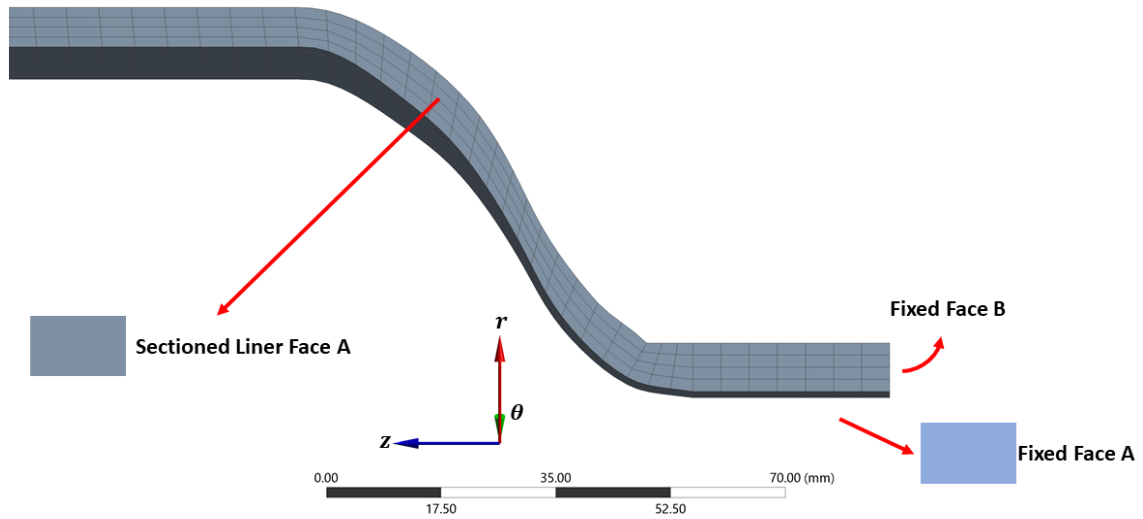
(a)
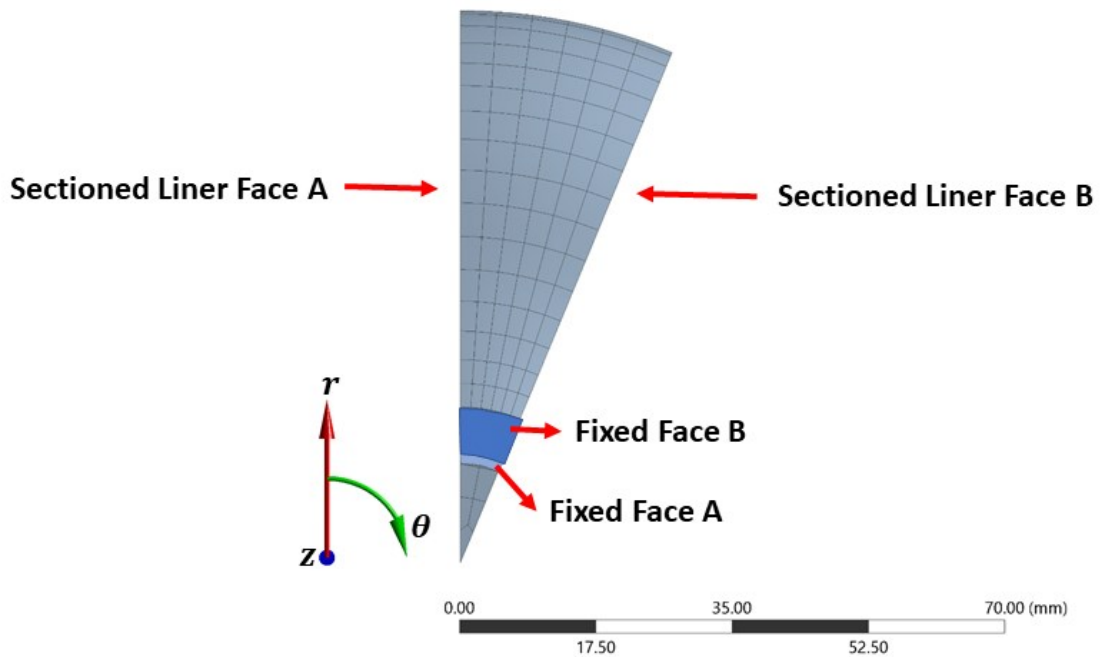
(b)

Figure 6.3. Boundary conditions for pressure vessel 3D FE model, (a) left-view (b) front-view

A mesh convergence study was also performed on the 1/16 model of the vessel. Average element sizes of 2 mm to 7 mm was utilized. Below the 2 mm element size, it is observed that the mesh was too fine to even work within the ANSYS software without

performing the FE analysis. Similarly, above 7 mm element size, severe defeaturing of the model was observed. Furthermore, element size larger than 7 mm had a sizably distorted aspect ratio, in order to ensure that at least three elements were present at the thickness direction, which adversely affects the convergence of the FE analysis.

Analysis settings were configured for the burst pressure simulations similar to the tensile testing numerical model, except the loading was given as pressure instead of displacement, due to the nature of the structural problem. Pressure as a load condition ensures that the force was always applied normal to the surface even in the expected cases of shape change of the surface. This loading condition perfectly represents the case of pressurizing the aluminum vessel. Loading was applied linearly up to final calculation time of 1 s, which corresponds to 30 MPa, with 4 different timestep regions, for improving the convergence of the analysis, thus proper burst pressure calculations of the vessels. Timestep regions were given as follows; 0.008 s up to 0.35 s, 0.002 between 0.35 s and 0.85 s, and finally 0.0005 until last converged timestep. All FE simulations were performed on a Dell Precision WorkStation T7500 featuring 2x HexaCore Intel Xeon X5690 at 3600 MHz and 48 GB of DDR3-SDRAM.

6.3. FE Analysis of Steel-based COPVs

The burst pressure of COPVs stresses throughout the liner, and the radial and axial strains during hydrostatic pressure tests were evaluated by a finite element model developed in ANSYS FEA software package.[90]

In addition to the available global Cartesian (x, y, and z) coordinates, a global cylindrical and a material Cartesian coordinate system were established. To define the boundary conditions for the sectioned walls and several hoop and radial strains, a global cylindrical coordinate system was utilized as r in radial-dir, θ in circumferential direction and z in axial-dir. For material and damage modeling, the local Cartesian coordinates were employed indicating 1 as fiber dominated direction, 2 as matrix dominated direction and 3 thickness (out-of-plane) direction.

34CrMo4 steel liner material was defined as an elastoplastic material in ANSYS. The bilinear isotropic hardening model was used for the plastic region. True stress – true strain behavior of 34CrMo4 steel was acquired from the relevant literature.[51] Yield

strength and tangent modulus of the bilinear isotropic model was calculated from the plastic behavior of the metal and given in Table 6.1.[51,91,92] 8 node solid hexahedral elements (SOLID185 in ANSYS) were used for modeling the liner.

Table 6.1. Orthotropic elastic properties and stress limits of glass and carbon fiber reinforced epoxy-based composites and isotropic properties of the steel liner. (Source: Liu and Zheng, 2010, Liao et al., 2018, Toh et al., 2018)

Symbol	Description	Unit	Value	Value
			Glass Fiber / Epoxy	Carbon Fiber / Epoxy
E_1	Longitudinal (fiber dominated) Modulus	MPa	38500	141000
$E_2 = E_3$	Transverse (matrix dominated) Modulus	MPa	16500	11400
$v_{12} = v_{13}$	Poisson's ratio (in-plane)		0.27	0.28
v_{23}	Poisson's ratio (plane 2-3)		0.40	0.40
$G_{12} = G_{13}$	In-plane shear modulus	MPa	4700	5000
G_{23}	Shear modulus (plane 2-3)	MPa	4700	3080
X_t	Longitudinal (fiber dominated) Tensile Strength	MPa	1250	2080
X_c	Longitudinal (fiber dominated) Compressive Strength	MPa	-650	-1250
Y_t	Transverse (matrix dominated) Tensile Strength	MPa	36	60
Y_c	Transverse (matrix dominated) Compressive Strength	MPa	-165	-290
S_{12}	In-plane shear strength	MPa	86	110
			Steel Liner	
E_{SL}	Young's Modulus	MPa	205000	
$v_{12,SL}$	Poisson's Ratio		0.3	
$\sigma_{y,SL}$	Yield Strength	MPa	743	
E_{tan}	Bilinear Isotropic Hardening Tangent Modulus	MPa	2600	

Composite layer orientations were configured as described in Figure 6.5, Figure 6.6 and Table 5.1. To simulate helical winding, a composite layer divided into homogenized + and – angle plies of winding. The single-ply thickness for helical and hoop plies was chosen as 0.2 mm in accordance with the average of measured values from manufactured COPV prototypes (Table 5.1). The hoop region defined for the cylindrical section of the model as hoop winding covered only the cylindrical section of the liner in filament winding manufacturing.

The thickness and angle variations in the filament winding process were defined to model from the data gathered from CADWIND filament winding simulation, utilizing draping features available in ANSYS ACP Pre module. The thickness variations at the front dome section in the composite model can be seen in Figure 6.4.
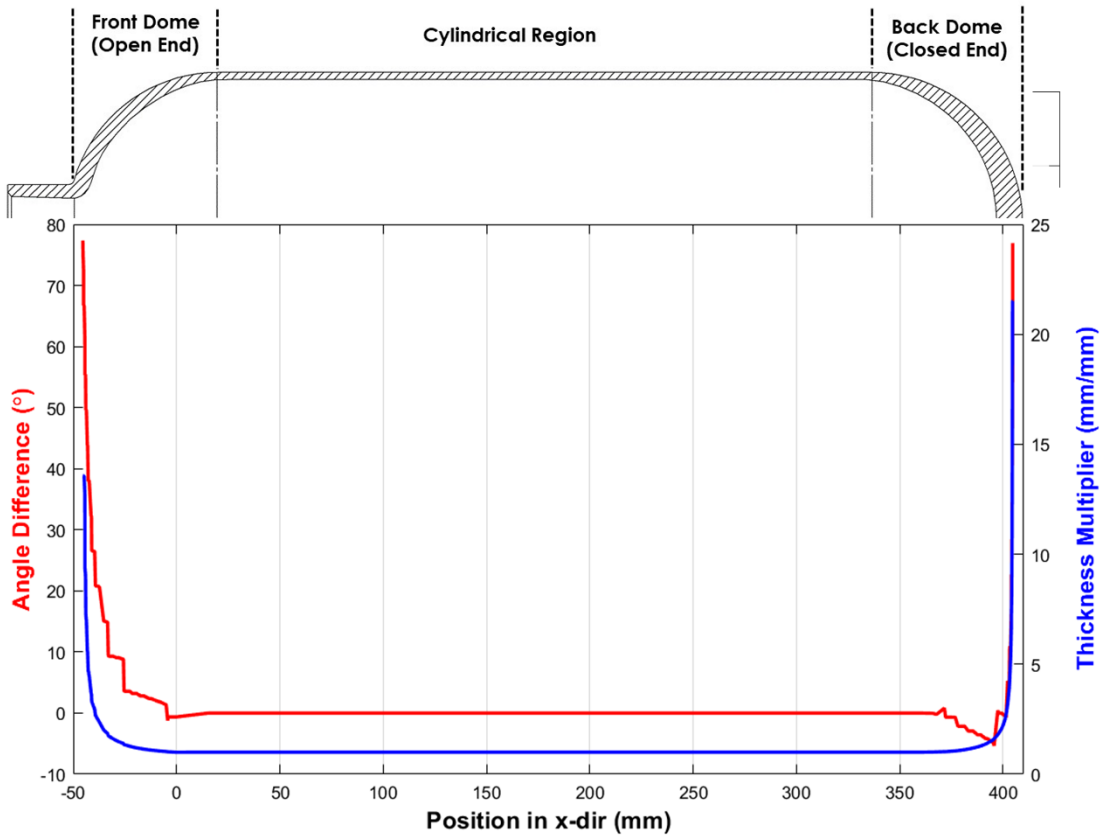
Figure 6.4. Thickness and angle deviations through the axial distance of the COPV.

Similar to the metal liner, 8 node solid hexahedral elements (SOLID185) were chosen for modeling overwrapping composite layers to evaluate 3D stress states of the composite section.
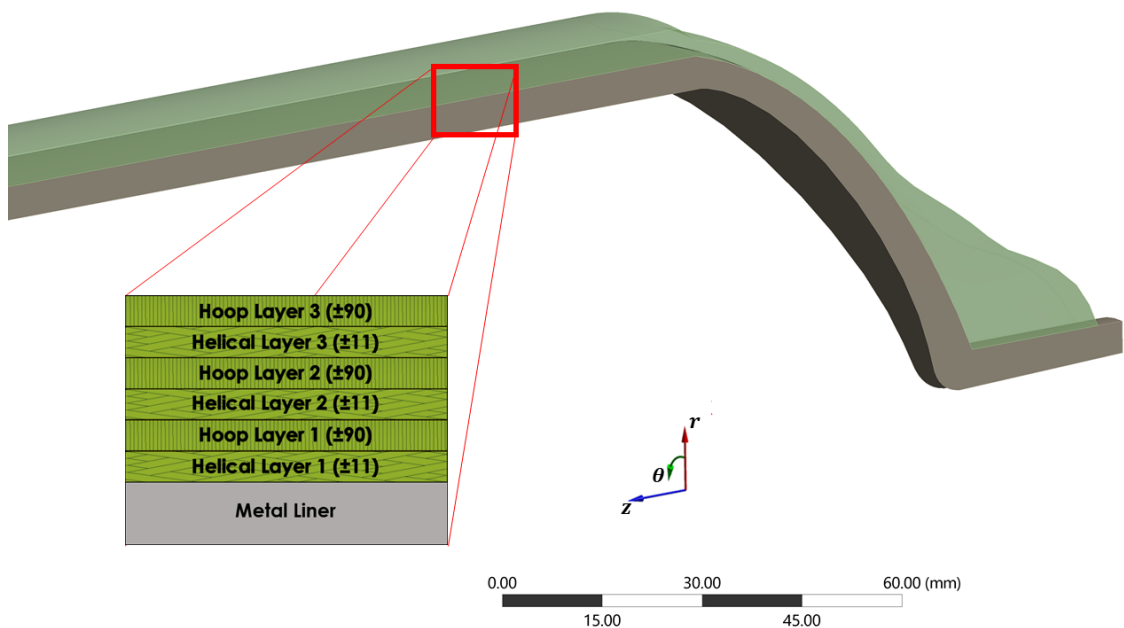
Figure 6.5. A schematic illustration of composite configurations of GF COPV with featuring thickness variations at the front dome section.
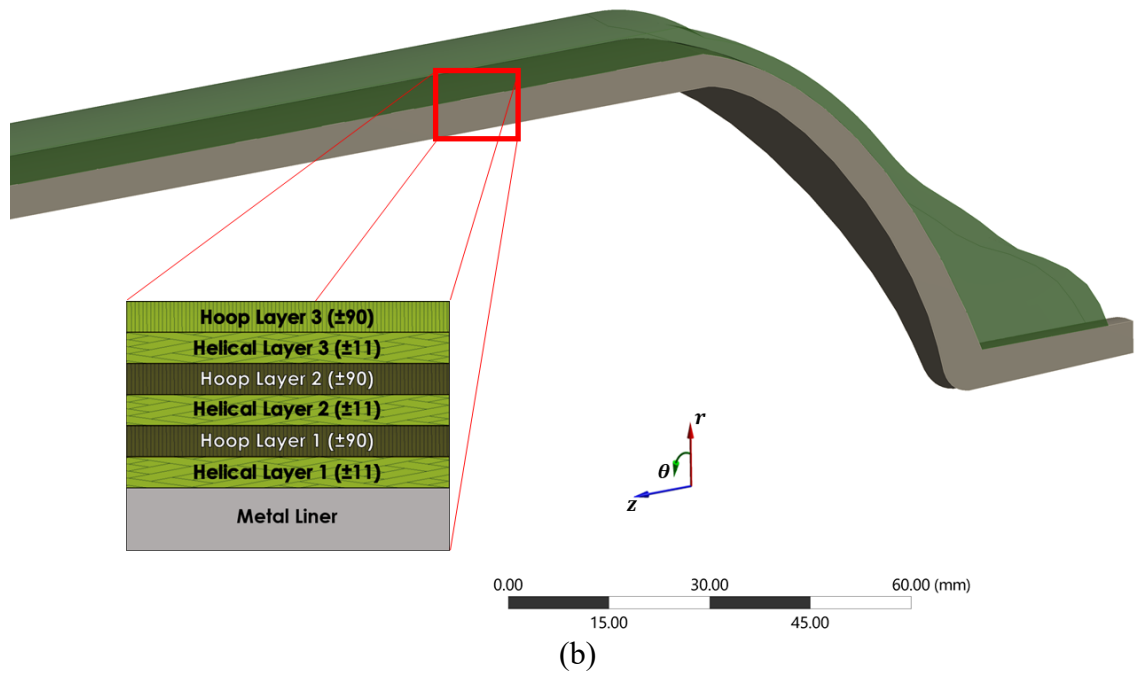
Figure 6.6. A schematic illustration of composite configurations of hybrid COPV with featuring thickness variations at the front dome section

In order to decrease the amount of computing time due to the complete 3D 8-node hexahedral modeling, and acquire a uniform mesh, the full vessel model was reduced to 1/16 by exploiting the axisymmetry in θ-dir. For the sectioned walls of the liner and composite layers in 1/16 model (Sectioned Composite and Liner Faces A & B shown in Figure 6.7 and Figure 6.8), the rotation in θ-dir was restricted and displacement in r and axial (z) direction set as unrestricted. The surfaces, which were in contact with the testing apparatus, were set as fixed faces (Fixed Face A&B).
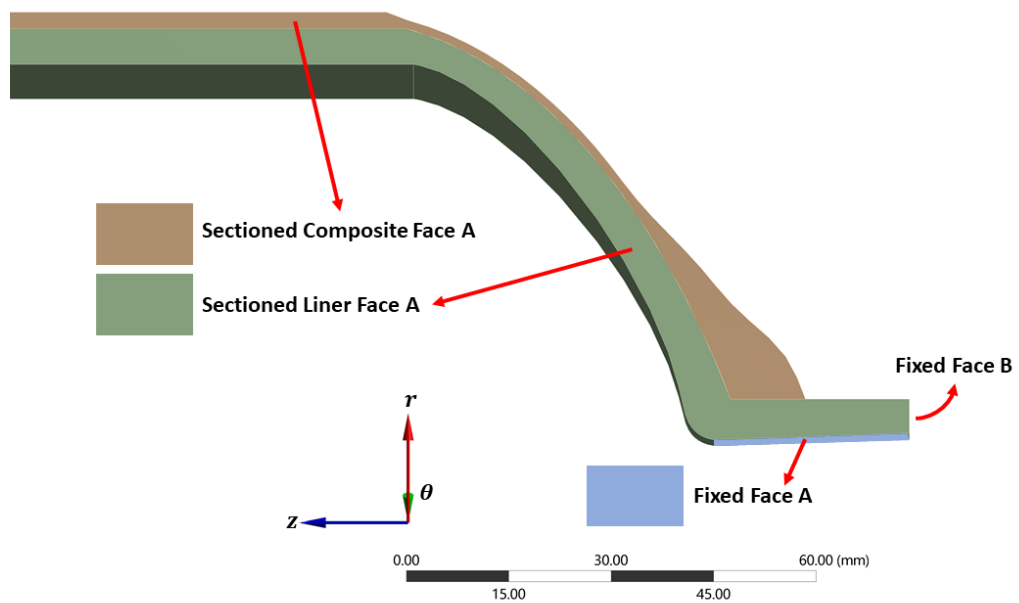
Figure 6.7. Boundary conditions for COPVs (left-view).
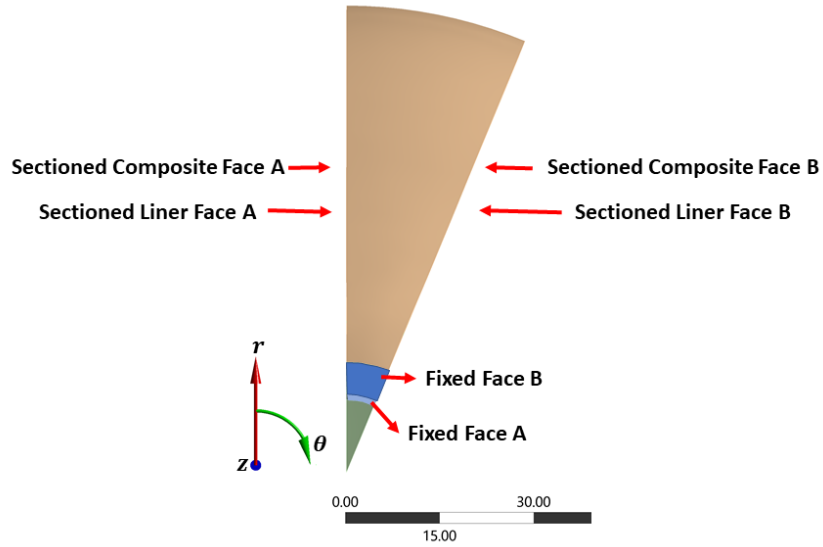
Figure 6.8. Boundary conditions for COPVs (front-view).

A comparison with the full model was also performed for axial and radial deformations of the liner in order to validate the boundary conditions of the reduced 3D model. The conclusion was that displacements in critical regions for both models showed a negligible difference (in the order of -5). A mesh convergence study was also performed to achieve the optimum mesh size for solution accuracy and computing time and 5 mm element size selected for both liner and composite layer modeling. The final 3D model consists of 12194 nodes and 11467 elements (including bonded contact elements between the liner and composite layers). The final 1/16 COPV 3D model with a mesh structure is shown in Figure 6.9.
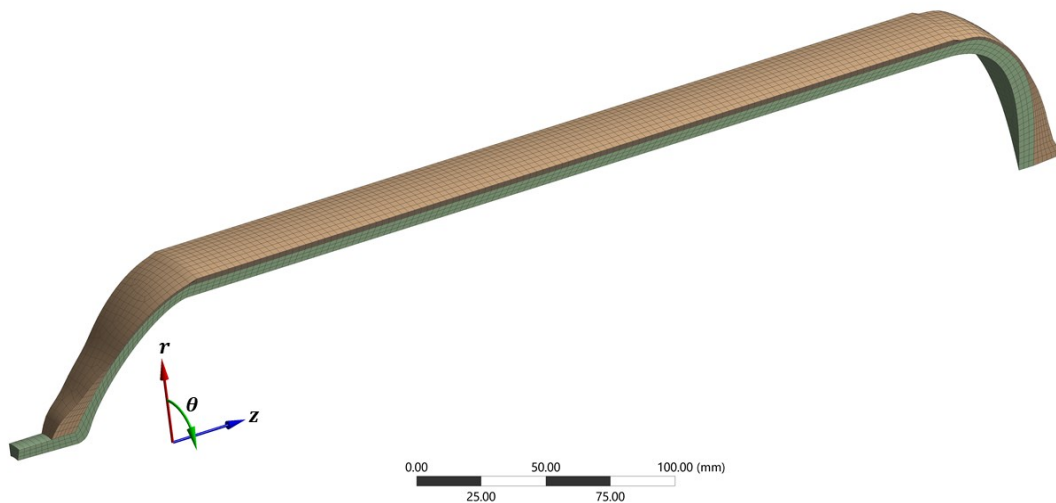
Figure 6.9. 1/16 sectioned 3D model of typical COPV.

The damage initiation in composite layers was defined by the Hashin failure criterion, which is an interactive failure theory that can identify the initiation of damage

modes as fiber tension, fiber compression, matrix tension or matrix compression.[34,93] The Hashin failure criterion has widely been used for composite failure modeling as a first ply failure criterion and is also available as a built-in feature in ANSYS.[94–96] The failure modes and corresponding criteria were considered in the Hashin failure theory for 3D solid elements given in Table 6.2.

Table 6.2. Failure modes with corresponding Hashin failure criteria and material property degradation (MPDG) constants. (Source: Hashin, 1980)

Failure Mode		Failure Criteria	MPDG Constants
Fiber Tension	$\sigma_1 \geq 0$	$F_{1,t} = \left(\frac{\sigma_1}{X_t}\right)^2 + \left(\frac{\tau_{12}}{S_{12}}\right)^2 + \left(\frac{\tau_{13}}{S_{13}}\right)^2$	0.9
Fiber Compression	$\sigma_1 < 0$	$F_{1,c} = -\left(\frac{\sigma_1}{X_c}\right)$	0.9
Matrix Tension	$\sigma_2 + \sigma_3 \geq 0$	$F_{2,t} = \left(\frac{\sigma_2}{Y_t}\right)^2 + \left(\frac{\tau_{23}}{S_{23}}\right)^2 + \left(\frac{\tau_{12}}{S_{12}}\right)^2 + \left(\frac{\tau_{13}}{S_{13}}\right)^2$	0.1
Matrix Compression	$\sigma_2 + \sigma_3 < 0$	$F_{2,c} = \left(\frac{\sigma_2}{2S_{23}}\right)^2 + \left(\frac{\tau_{23}}{S_{23}}\right)^2 + \left(\frac{\tau_{12}}{S_{12}}\right)^2 + \left[\left(\frac{Y_c}{2S_{13}}\right)^2 - 1\right]\frac{\sigma_2}{Y_c}$	0.1

A simple progressive damage model which involves an instant reduction in mechanical properties was adopted to simulate the damage evolution in composite plies. This method, also referred to as Material Property Degradation (MPDG) in ANSYS, is compatible with 3D solid elements and the Hashin failure criterion. This model is similar to ply discount method except for the fact that the amount of degradation differs within a range between 0 and 1 for each failure mode ($F_{f,t}$, $F_{f,c}$, $F_{m,t}$, $F_{f,c}$).[94,96,97] It was assumed that a failure in the fiber dominated direction involves directly with a fiber failure and leads to catastrophic or complete material degradation. Consequently, this causes a massive instant reduction in the mechanical properties in the fiber direction. Therefore, 90% (0.9) reduction was selected to demonstrate the failure in the fiber direction and also improve solution convergence (compared to 100% reduction). Dissimilar to the fiber direction, the degradation in matrix dominated (transverse to fibers) direction begins at the very early stages of the loading process but causes a minor reduction in mechanical properties. This was presumed as the damage only involves the matrix with cracking and crack propagation. The chosen values for each failure mode in this FE model were tabulated in Table 6.2.

The burst pressure was determined by the changes in radial displacement while increasing the internal pressure. A steep increase in the radius of the liner without increasing the internal pressure indicates the burst failure of the liner; thus, the COPV. This phenomenon generally occurs at the end (or nearly at the end, depending on the

applied MPDG parameters and parameters that affect convergence) of the last converged solution of FEA.

6.4. FE Analysis of Al-based COPVs with Doily Layers

Similar procedures were applied for the numerical analysis of Al-based carbon fiber reinforced COPVs with two significant differences being the number of the composite layers and the addition of doily layers.

Increasing the number of composite layers introduced two challenges for the FE analysis of the COPVs. First, the implementation of a large number of helical, hoop, and doily plies increased the total number of elements and nodes of the final 3D model of the COPV. Thus, the degrees of freedom of the system increased extensively, which directly affects the solution time of the FE analysis. In order to counter this, the hoop layers which consist of two plies each dedicated for forward and backward circumferential winding were merged to reduce the number of elements.

Another outcome of the increasing number of composite layers is that the mesh structure tends to be distorted in certain regions of the COPV. Specifically, the transition region from the boss to the dome section of the COPV, the mesh size becomes increasingly smaller at the outermost layer of the transition curvature. At a certain number of helical layers, the mesh becomes completely distorted and the model was not suitable to do any FE analysis. Even with a slightly lowered number of helical layers, convergence problems arise with the small mesh size and flexural loads. To prevent this, a change in boundary conditions were proposed and shown in Figure 6.10. Preliminary analysis showed that the removal of the non-critical boss region dramatically improves the convergence and the burst pressure prediction accuracy of the analysis. The removal of the boss region also reduced the number of elements of the model, which again improves the solution time of the analysis.

The implementation of doily layers to the FE model requires a careful definition of hoop and doily regions with their respective thickness variations. Otherwise unrealistic composite buildups may occur at the transition region. The final form of the transition region configured and validated with the manufactured specimens was shown in Figure 6.11. The merged forward and backward circumferential winding of hoop layers can

clearly be seen and the doily layers were visible as thicker plies at the front dome region. The doily layers in all simulations were modeled as woven carbon fiber plies in contrast with helical and hoop plies, which were unidirectional.

(a)

(b)
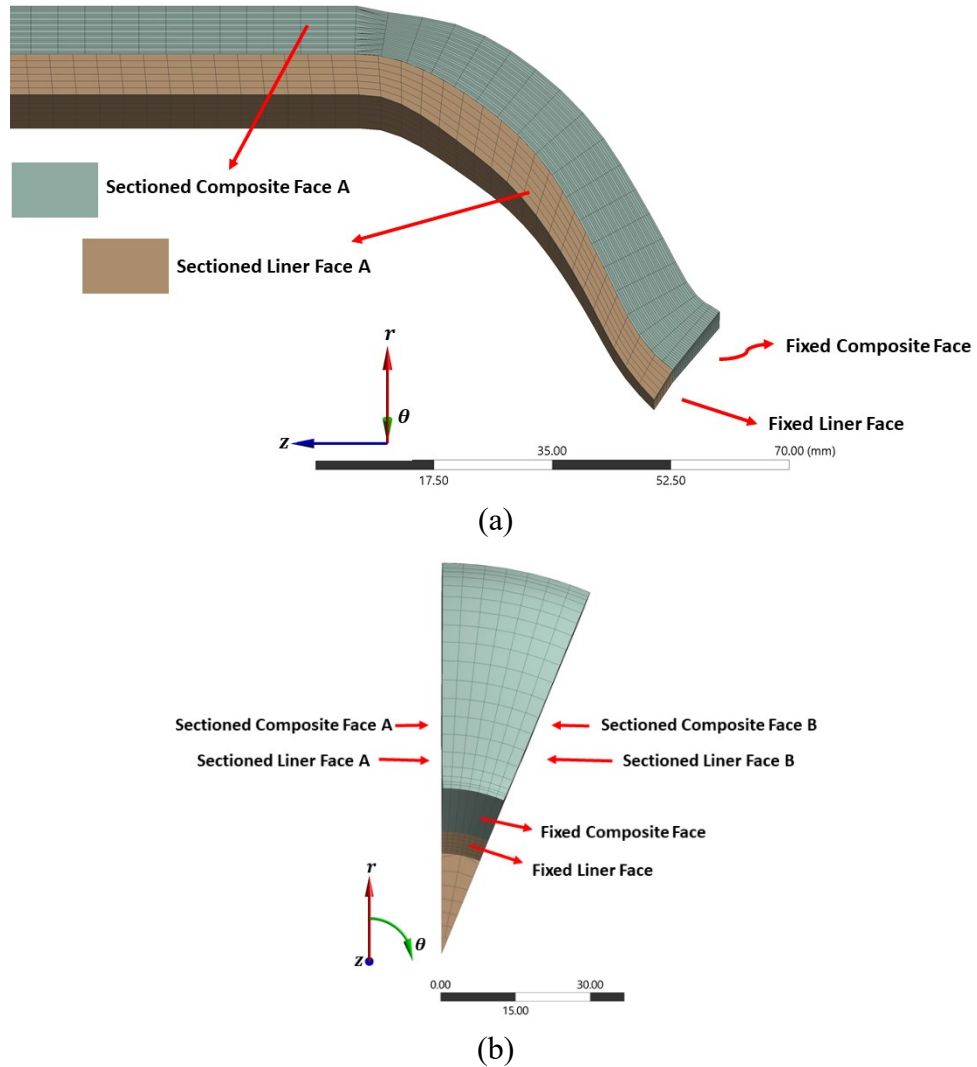
Figure 6.10. Boundary conditions for Al-based COPVs (a) left-view (b) front-view.
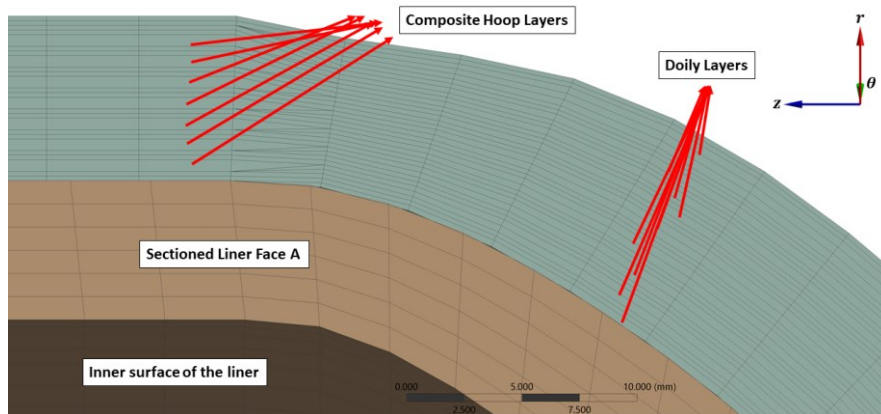
Figure 6.11. The transition region from the cylindrical section to the front dome of the Al-based COPV.

CHAPTER 7

RESULTS AND DISCUSSION

7.1. Tensile Testing

At least five tensile tests were conducted for aluminum specimens, and the results were given in Table 7.1. The experimentally determined mechanical properties, especially yield strength, seems to be lower than the values reported in the literature.[98] The manufacturing processes of the metal pressure vessels might contribute to this difference. These results were employed in further FE analysis. Moreover, experimental the engineering stress-strain behavior of the Al 6061-T6 specimens under tensile loading can be found and compared with the FE model results in Figure 7.4.

Table 7.1. Experimentally found mechanical properties of the Al 6061-T6.

Symbol	Description	Unit	Value
E_{SL}	Young's Modulus	MPa	57548
$v_{12,SL}$	Poisson's Ratio		0.33
$\sigma_{y,SL}$	Yield Strength	MPa	240.3
E_{tan}	Bilinear Isotropic Hardening Tangent Modulus	MPa	975
$\sigma_{ult,\,true}$	True ultimate tensile strength	MPa	317.0

Three different types of filament wound composite plates, Şişecam FW06 glass fiber, DowAksa A-49 and Toray T700SC-1200K carbon fibers were tested with specimens sectioned from the cured plates, accordingly to ASTM D3039 – 17 and the findings were tabulated in Table 7.2.

Table 7.2. Tensile test results of carbon fiber/epoxy plates.

Specimen	Longitudinal Tensile Str. (MPa)	Transverse Tensile Str. (MPa)	E_1 (GPa)	E_2 (GPa)
Şişe Cam FWR6 GF / Epoxy	609.8	14.9	27.93	13.23
DowAksa A-49 CF /Epoxy	1082	15.2	108.3	8.82
Toray T700SC-12K CF / Epoxy	1100	-	95.6	-

When the tensile testing results of the filament wound composite plates were compared with the commonly used values in the literature, it was observed that

experimental values were significantly lower than values found in the literature. This phenomenon can be explained by the residual stresses caused by the sharp plate ends of the aluminum plate mandrel and thermal expansion difference of cured composite and aluminum. Due to the inferior results in composite mechanical properties, it was decided to use values from the literature for FE analysis of COPVs. The specimens after the tensile testing can be seen in Figure 7.1.

(a)   (b)   (c)
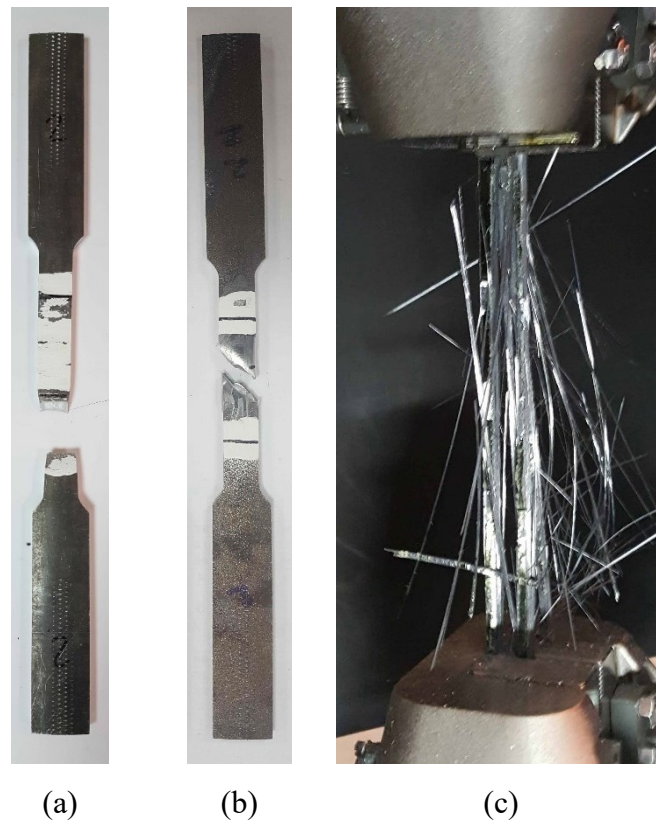
Figure 7.1. The failure modes of the tensile test specimens. (a) aluminum, (b) steel, (c) carbon fiber/epoxy composite

7.2. Burst Pressure Test Results

The burst pressure test was carried out for steel liners, glass fiber COPVs and glass/carbon fiber hybrid COPVs. The average burst pressure of steel liner was found as 657 bar. The average burst pressure of aluminum liners was measured as 279 bar. The glass fiber COPVs exhibited an average burst pressure of 899 bar, which is nearly the same as hybrid COPVs (have an average burst pressure of 905 bar). The burst pressure test results of the prototype pressure vessels are presented in Table 5.1 above.

The burst failure modes of all the pressure vessels tested are shown in Figure 7.3.

As clearly observed, the final rupture occurred at the cylindrical section except for the aluminum-based COPVs and was detected as a safe burst mode.

(a)

(b)

(c)

Figure 7.2. (a) Neat steel liner, (b) glass fiber COPV, (c) hybrid Fiber COPV specimens after burst pressure testing.

Acoustic observations performed during hydrostatic testing revealed that matrix cracking developed first in the composite parts. The fiber breakage occurred predominantly on the hoop layers, presumably due to the larger strains measured in the hoop direction. The final rupture was observed on the liner, as soon as it reached a macroscale failure of the reinforcing composite layer.

The burst pressure test was carried out for aluminum-based COPVs and the results are given in Table 7.3. The COPVs ALCF 1 to 4 does not contain any doily layers and

although the number of helical and hoop layers increased, results showed the burst pressures are same. All the COPVs were failed from the front dome section. These results lead to the implementation of doily layers.

(a)

(b)
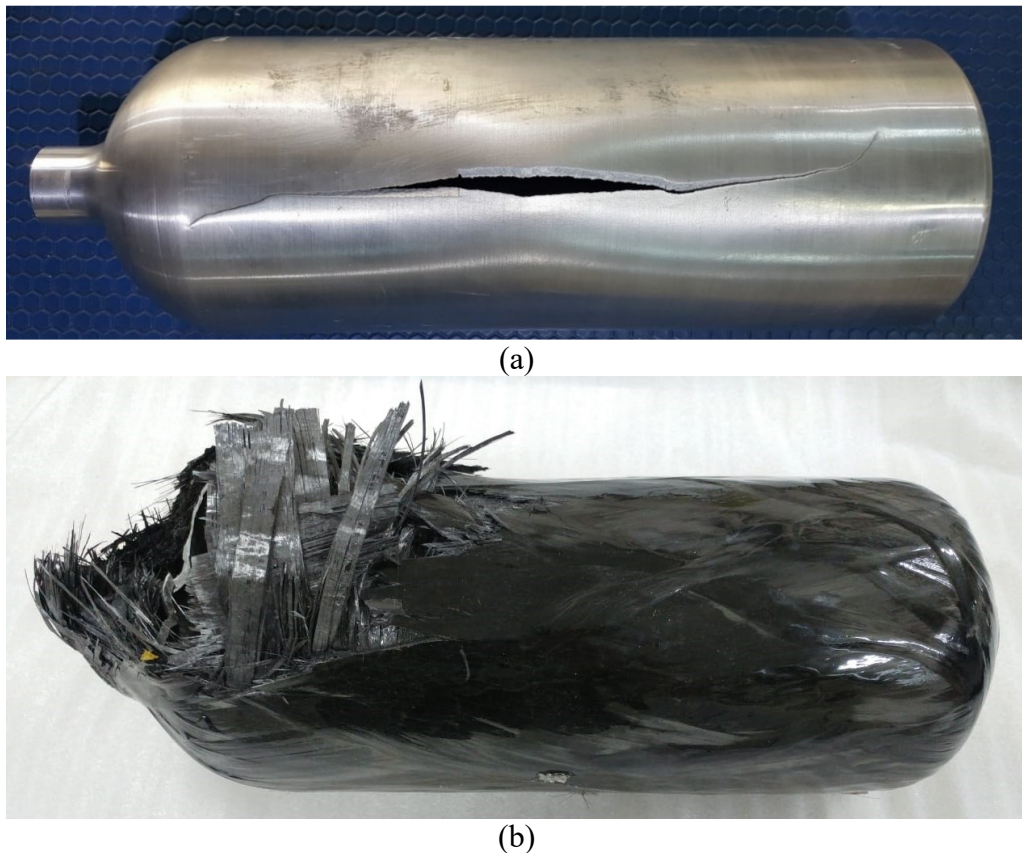
Figure 7.3. (a) Neat aluminum liner, (b) carbon fiber reinforced Al-based COPV
specimen after burst pressure testing.

The COPVs ALCF 5 to 8, contain additional doily layers that were placed to the front dome section and ALCF 9 prototype also contains extra doily layers positioned at the aft dome of the COPV. The number of helical and hoop layers were kept constant while increasing the number of doily layers to observe the effects of doily layers. The burst pressure test results were showed that the addition of doily layers increased the burst pressure performance of the COPVs significantly. Although the COPVs still continued to fail front dome section, the burst pressure increased from 1018 bar to 1330 bar (up to 30.6%).

Increasing the number of front and aft doily layers further shifted the burst location to the cylindrical section of the vessel, thus inducing a safe burst as it happened in specimen ALCF 10. A burst that happened in the cylindrical section created a room for additional hoop layer. In specimen ALCF 11, eighth hoop layer was introduced to the composite reinforcement. This further increased the burst pressure performance and

achieved nearly 1400 bar. 1400 bar is a critical pressure for COPVs as it is two times of working pressure of high-pressure COPVs. The ISO standard indicates a safety factor of 2 for fully carbon fiber reinforced COPVs, so specimen ALCF 11 fulfilled this standard for this criterion.

Table 7.3. Burst pressure test results of the Aluminum-based COPVs.

Specimen	Layer Orientation	# of Front Doily Layers	# of Aft Doily Layers	Burst Pressure (bar)
ALCF 1	$[\pm11°]_9 / [\pm90°]_7$	-	-	1018
ALCF 2	$[\pm11°]_9 / [\pm90°]_8$	-	-	1050
ALCF 3	$[\pm11°]_{12} / [\pm90°]_{11}$	-	-	1050
ALCF 4	$[\pm11°]_{13} / [\pm90°]_{11}$	-	-	1050
ALCF 5	$[\pm11°]_9 / [\pm90°]_7$	7	-	1146
ALCF 6	$[\pm11°]_9 / [\pm90°]_7$	11	-	1170
ALCF 7	$[\pm11°]_9 / [\pm90°]_7$	15	-	1264
ALCF 8	$[\pm11°]_9 / [\pm90°]_7$	17	-	1281
ALCF 9	$[\pm11°]_9 / [\pm90°]_7$	17	5	1330
ALCF 10	$[\pm11°]_9 / [\pm90°]_7$	17	9	1355
ALCF 11	$[\pm11°]_9 / [\pm90°]_8$	17	9	1397

7.3. FE Analysis – Tensile Testing

FE material model validated through simulation performed with different boundary conditions and hardening models. Figure 7.4 shows comparisons between experimental data and FE analysis. As one can clearly see the multilinear isotropic hardening model fits well with experimental results compared to bilinear isotropic hardening.

Two different loading conditions were also compared. The load was given as a displacement in x-direction fits well even beyond $\sigma_{eng,UTS}$. The local deformation (necking) at the center of the specimen was also observed in post-processed results in ANSYS. On the contrary, directly given forces on the same boundary results in convergence problems in ANSYS after $\sigma_{eng,UTS}$. This is explained through load condition given in force or pressure must monotonically increase equivalent stresses in 3D elements in ANSYS. Up until $\sigma_{eng,UTS}$ both load conditions showed nearly identical behavior. Unfortunately, it is not always possible to give load conditions as displacements, which

internally pressurizing of pressure vessels can be named as one.
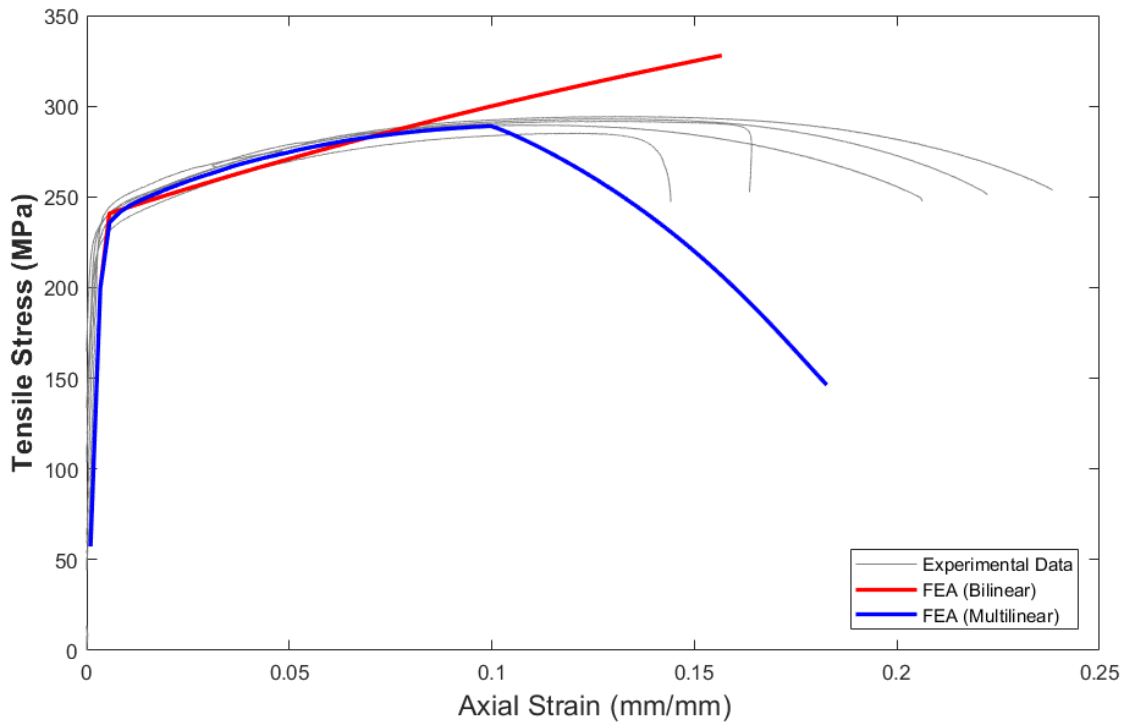
Figure 7.4. Stress vs. strain behavior between marked regions in the test coupons.

7.4. FE Analysis – Burst Pressure Testing

Numerical simulations for determining the burst pressure of the aluminum vessels carried out for different model and mesh sizes. Model specifications such as average element size of meshing, number of nodes and elements with the corresponding computation time were compared in Table 7.4.

Table 7.4. Comparison of FE models developed for determining the burst pressure for the Al liner

Model Size	Avg. Element Size (mm)	# of Nodes	# of Elements	CPU Time (s)	Burst Pressure (MPa)
Full	7	71999	14328	4399	27.90
Half	7	36872	7164	1471	27.92
Quarter	7	18769	3561	557	27.90
1/16	7	5398	900	122	27.92
1/16	6	9368	1700	223	27.90
1/16	5	13428	2492	359	27.93
1/16	4	22775	4435	732	27.90
1/16	3	55653	11613	2522	27.89
1/16	2	158354	34790	13132	27.89

It can be clearly seen from the burst pressure and mechanical behavior that the structural problem does not have a mesh size dependency. Moreover, when compared to the full model, the boundary conditions introduced with the model reduction did not affect the mechanical behavior of the vessel. In Figure 7.5 axial and radial deformation behavior of the liners with different mesh sizes were compared and it was found out the deformation curves overlapped on each other seamlessly.
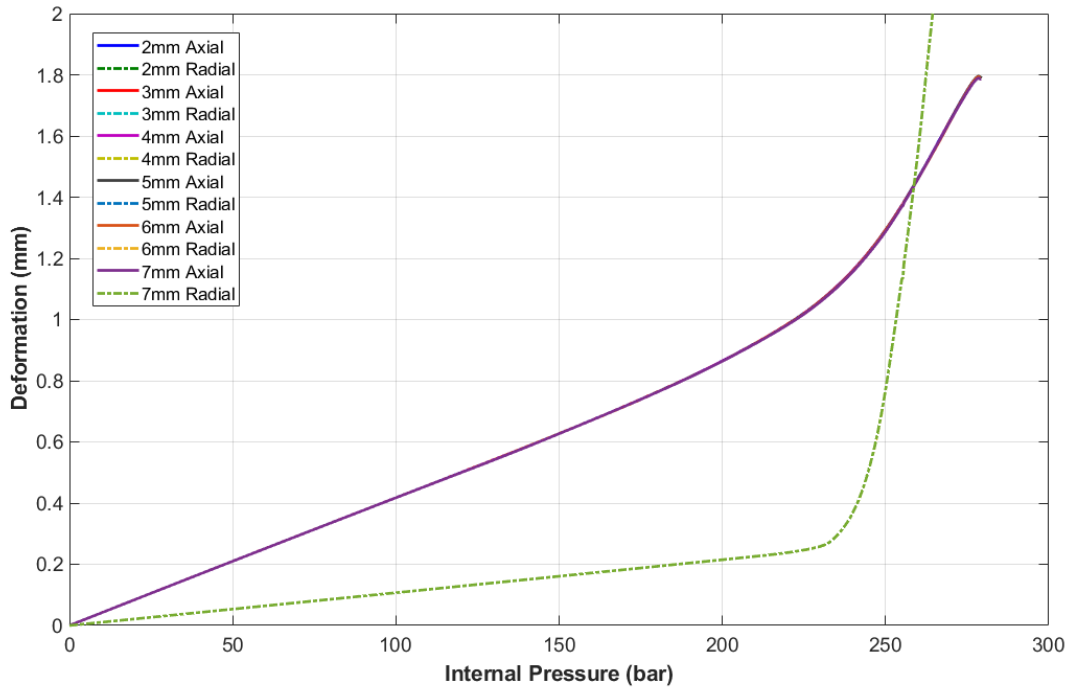
Figure 7.5. Radial and axial deformation comparison of FE models with different
average element size

Rosette type strain gages were utilized to measure the local strains (axial and hoop) in above-mentioned positions (Figure 5.2). Axial and hoop strains obtained from during burst pressure test were compared with the FEA results.

Figure 7.6 to Figure 7.8 show the comparison of experimental and predicted strain values at the strain gages located at the front, central and aft section of the vessel, respectively. It was found that the experimental and FEA results are very similar for the neat aluminum liners. Lower axial strains as compared to hoop strains, higher hoop strains in the central region and similar hoop strains at front and back regions of the vessel were observed. While the hoop strain behavior of the back cylindrical section of the neat Al liner was similar to the experimental results, there were still significant deviations in strain values. This can be explained by the local plastic deformation of the linear near the back cylindrical section of that specific liner.
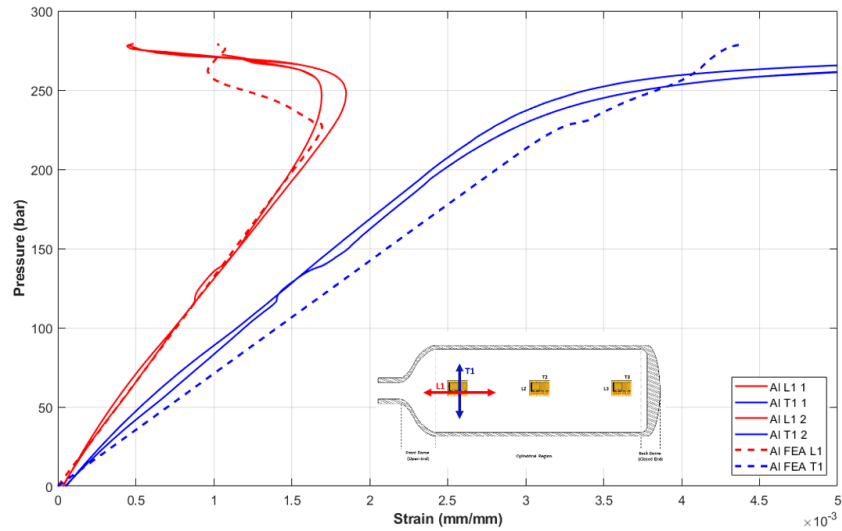
Figure 7.6. A comparison of experimental and FEA prediction of axial and hoop strain values of the Al pressure vessel at the front cylindrical section.
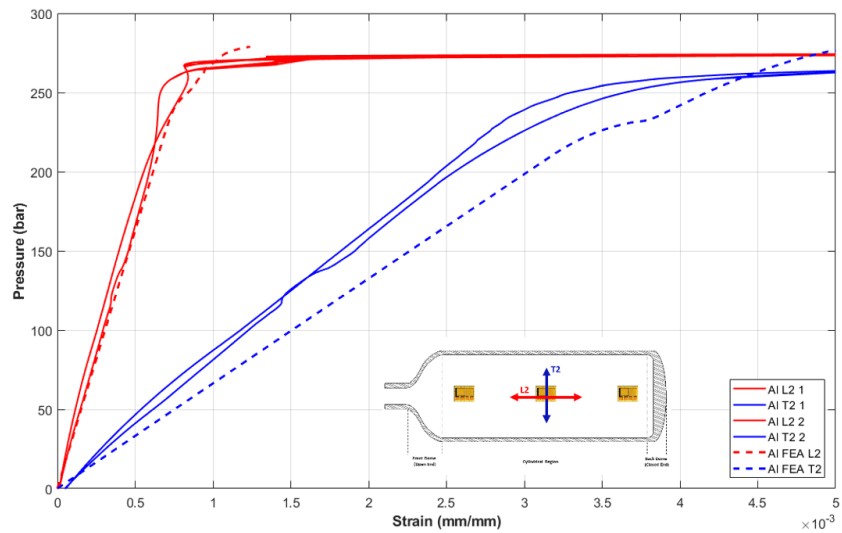
Figure 7.7. A comparison of experimental and FEA prediction of axial and hoop strain values of the Al pressure vessel at the central cylindrical section.
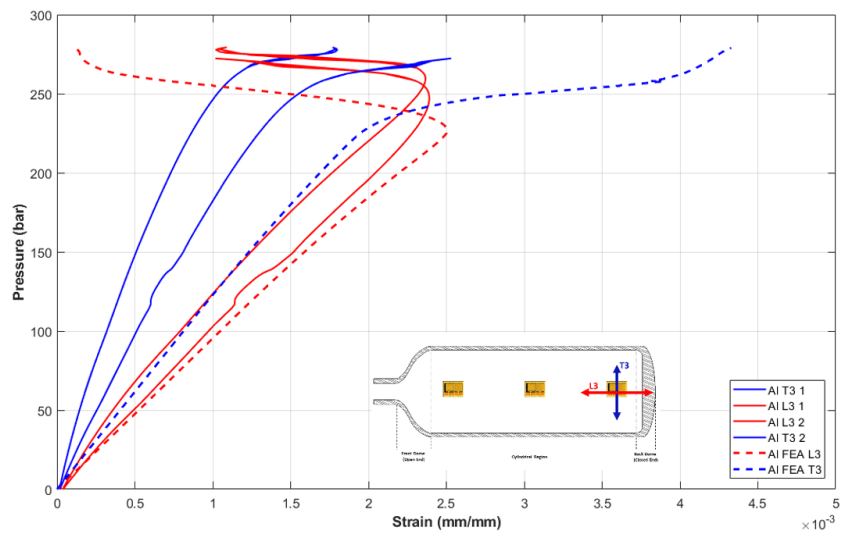
Figure 7.8. A comparison of experimental and FEA prediction of axial and hoop strain values of the Al pressure vessel at the back cylindrical section.

7.5. FE Analysis – Steel-based COPVs with Hybridization

Rosette-type strain gages were utilized to measure the local strains (axial and hoop) in the above-mentioned positions (Figure 5.12). The comparison of experimental and FE model predicted the hoop and axial strain values at the strain gages located at the front, central and back cylindrical section of the vessels, and were shown in Figure 7.9 to Figure 7.14, respectively. The respective positions of the strain gages were also specified within the abovementioned figures. The results indicated that there were satisfactory agreements between experimental and numerical strains, especially in the hoop direction. In general, the stiffer strain response was observed from hybrid vessels as expected.
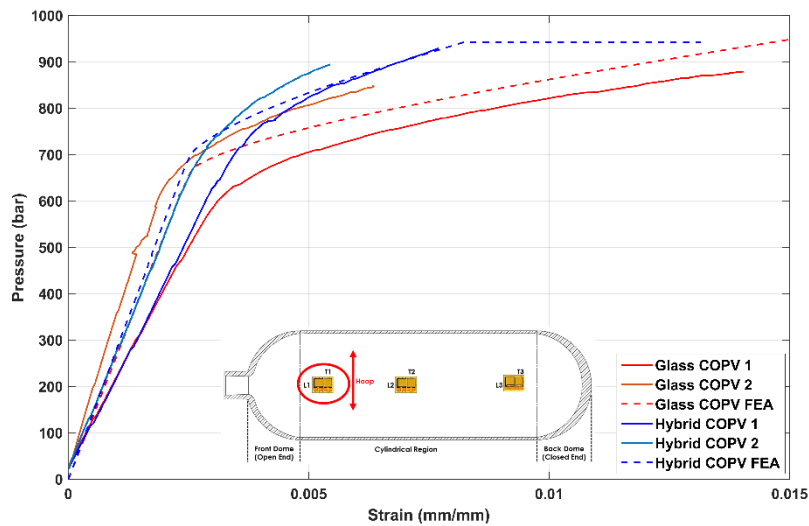
Figure 7.9. Comparison of experimental and FEA prediction of hoop strain values of glass fiber and Hybrid COPV at the front (T1) cylindrical section.
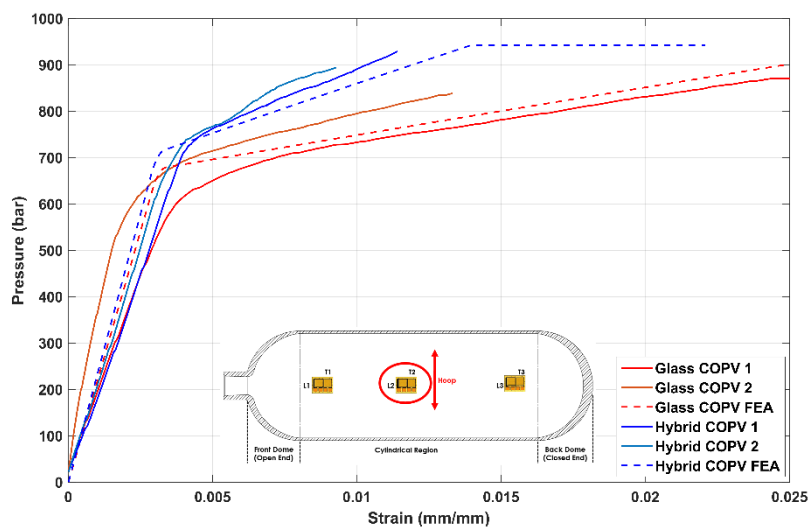
Figure 7.10. Comparison of experimental and FEA prediction of hoop strain values of glass fiber and Hybrid COPV at the central (T2) cylindrical section.
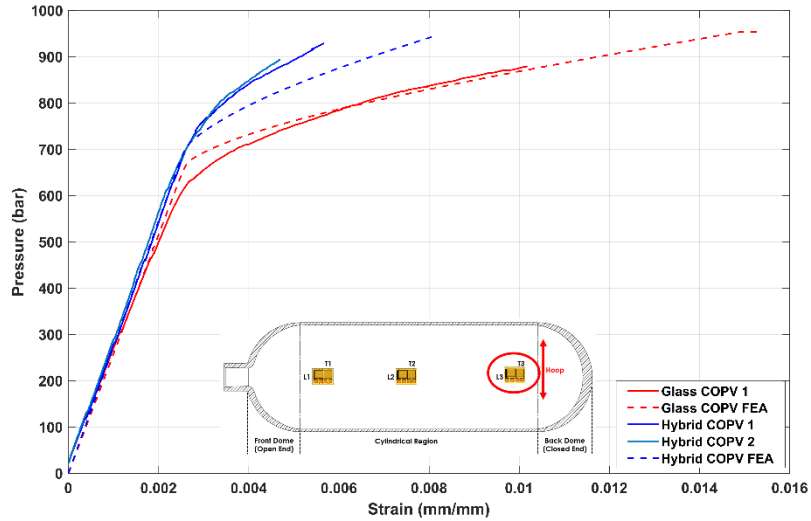
Figure 7.11. Comparison of experimental and FEA prediction of hoop strain values of glass fiber and Hybrid COPV at the back (T3) cylindrical section.
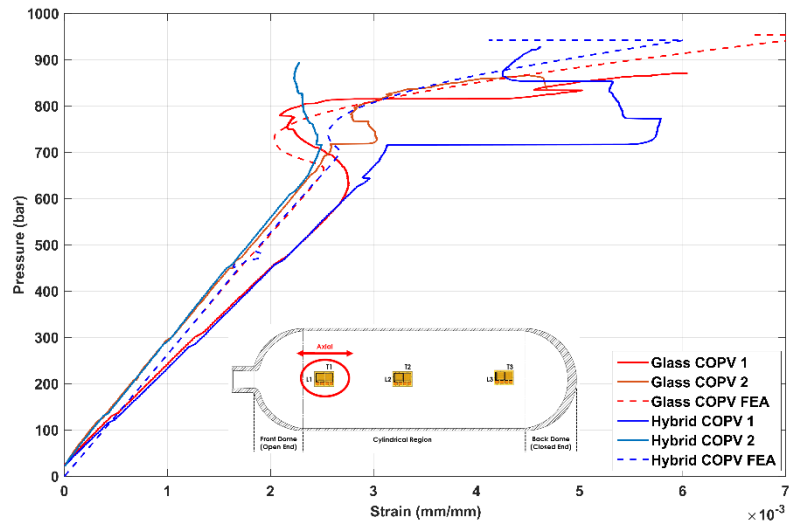
Figure 7.12. A comparison of experimental and FEA prediction of axial strain values of the glass fiber and Hybrid COPV at the front (L1) cylindrical section.
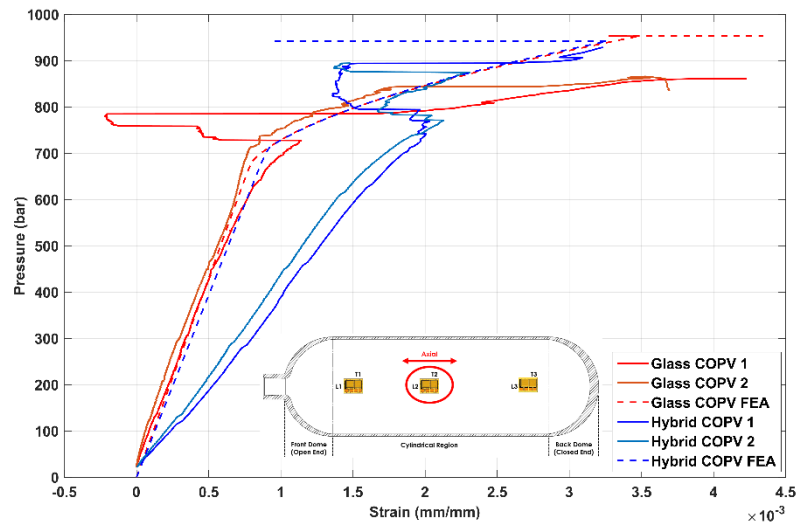
Figure 7.13. A comparison of experimental and FEA prediction of axial strain values of the glass fiber and Hybrid COPV at the central (L2) cylindrical section.
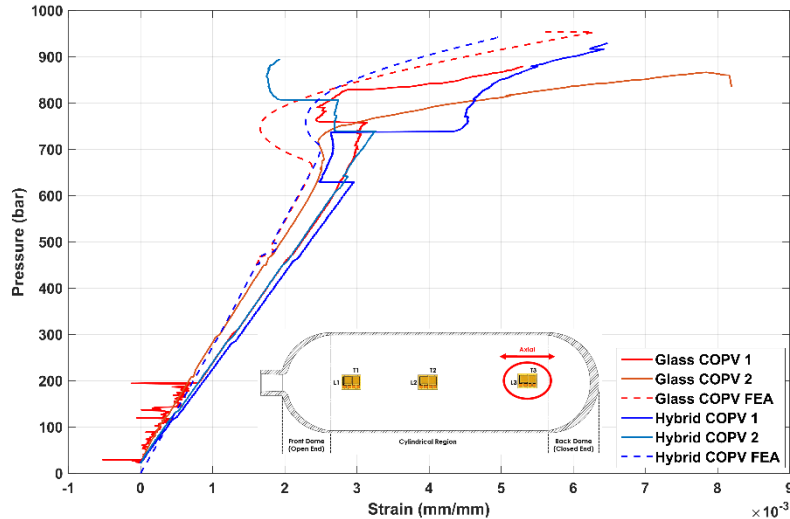
Figure 7.14. A comparison of experimental and FEA prediction of axial strain values of the glass fiber and Hybrid COPV at the back (L3) cylindrical section.

Strain gage measurement distortions were observed significantly more in the axial direction than the hoop direction. This might be linked to an order of magnitude smaller strains in the axial direction and strain gage sensitivity. The placement of axial strain gages between the outermost hoop rovings may also contribute to the observed distortions.

The radial and axial deformation vs. internal pressure curves were plotted for all types of vessels in order to determine the burst pressure based on FEA and shown in Figure 7.15 and Figure 7.16, respectively. The investigation of the metal liner behavior concluded that the liner apparently yielded at about 644 bar, and then a significant radial deformation was observed. The yield point of the bare the liner can also be considered as the lower limit burst of the bare metal liner, due to the absence of any additional reinforcements to keep the liner intact. The behavior of COPV distinctly differentiated from the bare liner since its liner yield occurred at higher internal pressures (679 bar for glass COPV and 715 bar for hybrid COPV). After yielding of COPV liners, composite reinforcement was the sole responsible for resisting the internal pressure, which is observable from the change in the linearity of radial deformation.

The deformation behavior of COPV also denoted as hybrid COPV radial deformation was significantly smaller than Glass COPVs at the same pressure, which is an indication of a positive hybridization effect. Last, the burst points of COPVs were clearly seen as a steep increase in the radial deformation without any increase in the internal pressure. COPV burst pressures were identified as 952 bar for glass-based COPV, and 942 bar for glass/carbon-based COPV. Both experimental and numerical findings

indicated that no hybridization effect was present for the burst pressure of the vessels (Table 7.5).
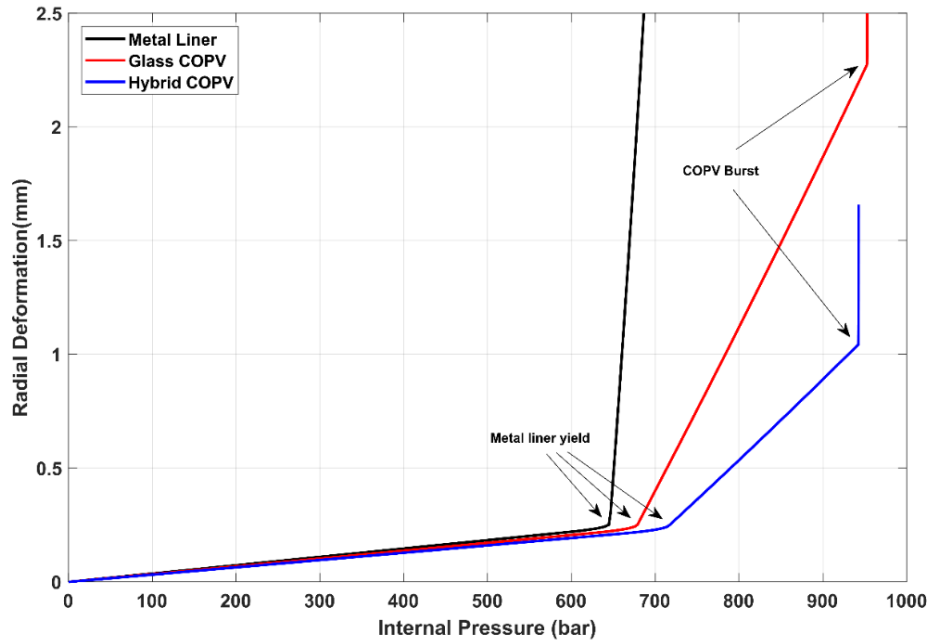
Figure 7.15. The radial deformation vs. internal pressure curves of pressure vessels, obtained from FEA
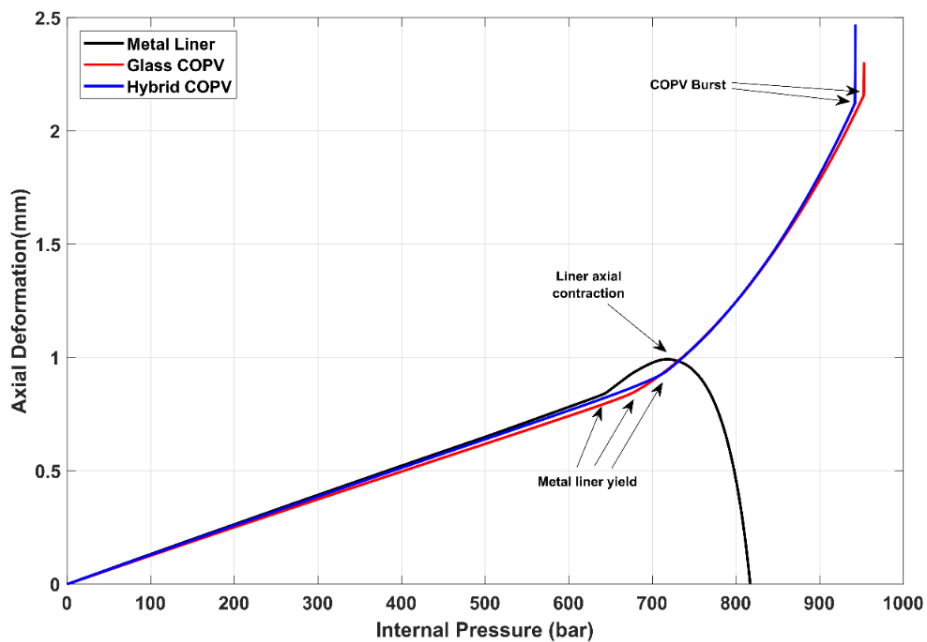
Figure 7.16. The axial deformation vs. internal pressure curves of pressure vessels, obtained from FEA

The result of FE analysis showed that axial deformations of the bare metal liner and COPVs differ significantly. After yielding of the bare metal liner, the axial deformation continued to increase up to 718 bar. After that point, the deformation of the

bare liner dominated by the radial deformation and began to contract axially. This may not occur during the hydrostatic pressure experiments due to the fact that the final burst pressures of bare metal liners did not exceed above 692 bar.

For bare metal liners, the lower (yielding) and upper (axial contraction) limits of burst pressures can be identified as 644 and 718 bar respectively. COPVs did not show any contraction behavior. This is owing to the perfectly bonded composite reinforcement in the FE model, as the composite reinforcement resists any expansion or contraction. Only glass helical filament wound layers reinforce both types of COPVs in the axial direction; therefore, the axial deformation behavior of both glass and hybrid COPVs were observed as nearly identical as expected. Similar to the radial deformation curves, burst pressures of COPVs can also be detected from axial deformation behavior, for axial deformations increase steeply without any increase in the internal pressure.

Figure 7.17 reveals the maximum equivalent (von-Misses) stress throughout the liner with increasing the internal pressure. The composite reinforcement effect can be realized as lower stresses were observed in COPVs compared to the bare metal liner, particularly at the linear region of the curves. Figure 7.17 depicts the maximum stress of the whole liner through the burst pressure test. The exact location may change with increasing pressure; for instance, the maximum stress may occur in the frontal dome at lower internal pressures and in the central cylindrical section at near burst pressures.
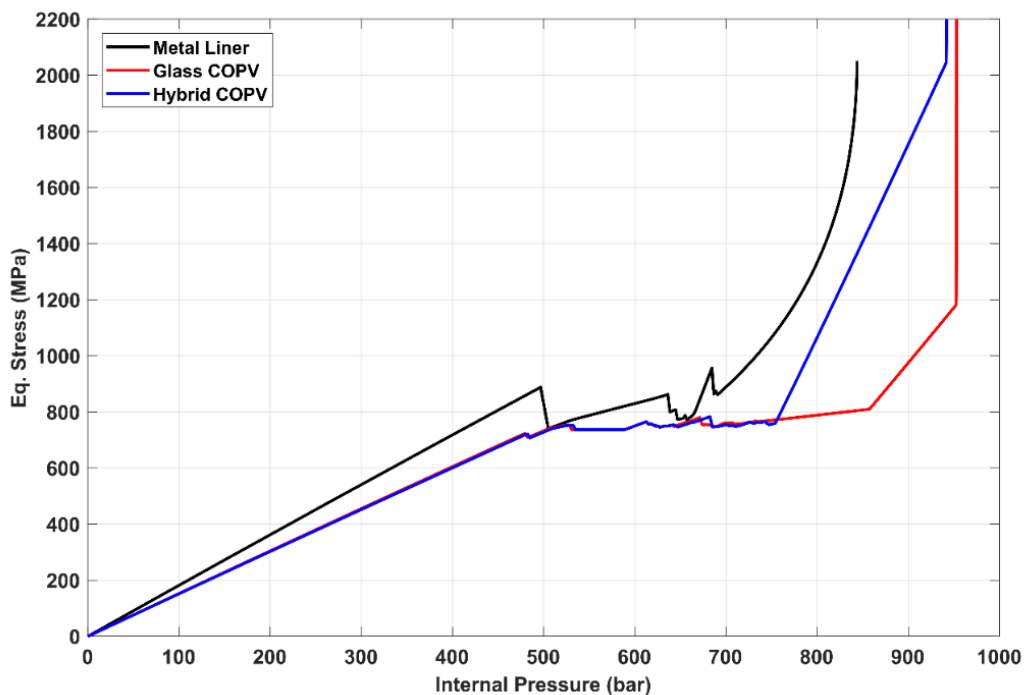
Figure 7.17. The maximum equivalent stress of the liner vs. internal pressure curves, obtained from FEA

So as to further investigate the mechanical behavior of the vessels, the equivalent stress through the inner surface of the liner obtained from FEA at internal pressure levels of 500 and 700 bar and plotted in Figure 7.18 and Figure 7.19, respectively. Before yielding of the liner (Figure 7.18), the highest stresses occur at halfway through the frontal dome section. The effect of composite reinforcement was apparent on stress concentrations at the frontal and back domes and through the cylindrical region. It can also be observed that the hybridization of composite hoop layers further contributed to lowering the stress of the cylindrical section of the vessel.
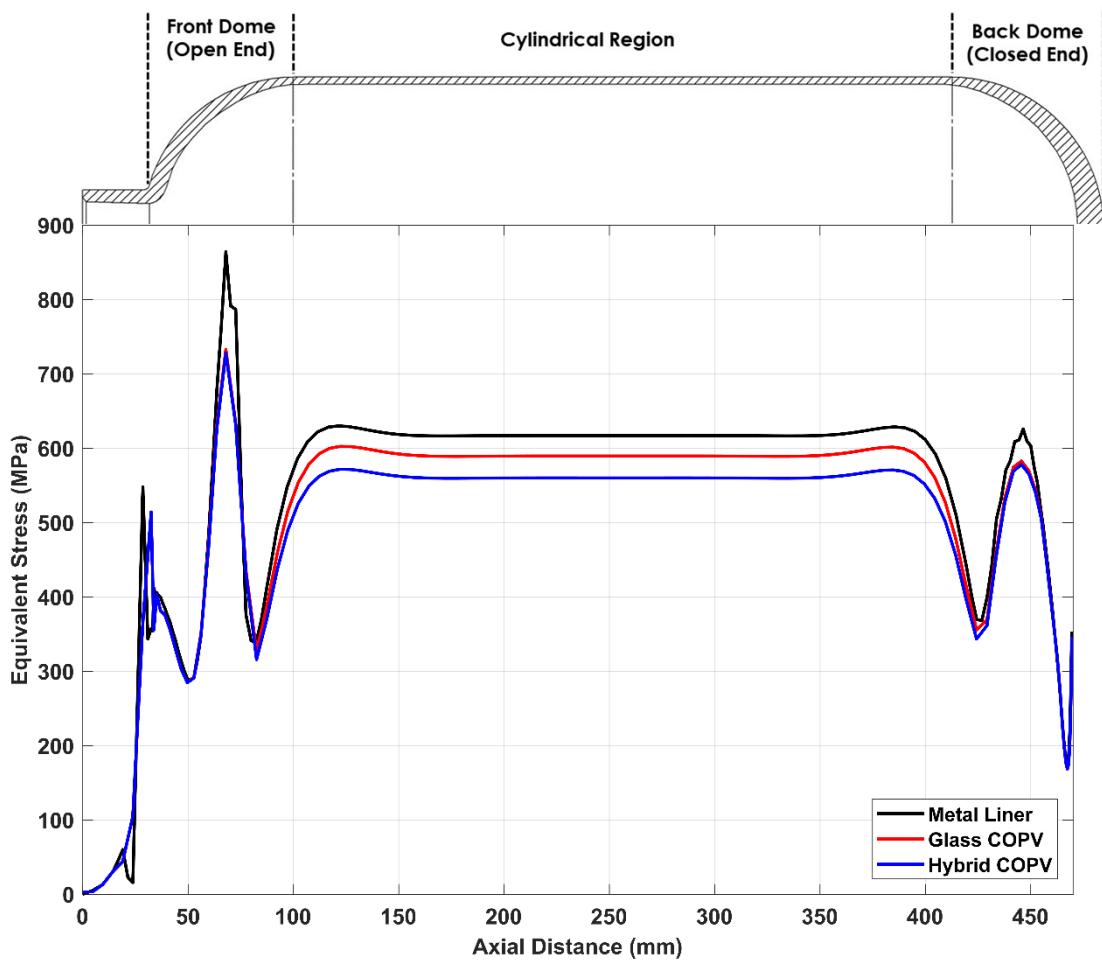
Figure 7.18. The equivalent stress vs. axial distance along the inner surface of the liner at 500 bar.

The maximum stress was reached at near burst (Figure 7.19) cylindrical region, as expected. The bare liner showed the highest stresses at the central section of the cylindrical region owing to the fact that it has no composite reinforcement. COPVs exhibit a similar behavior because of the fact that the liner has significantly lost its load-carrying capability, and that it reached maximum stress plateau through the cylindrical region of the vessel.
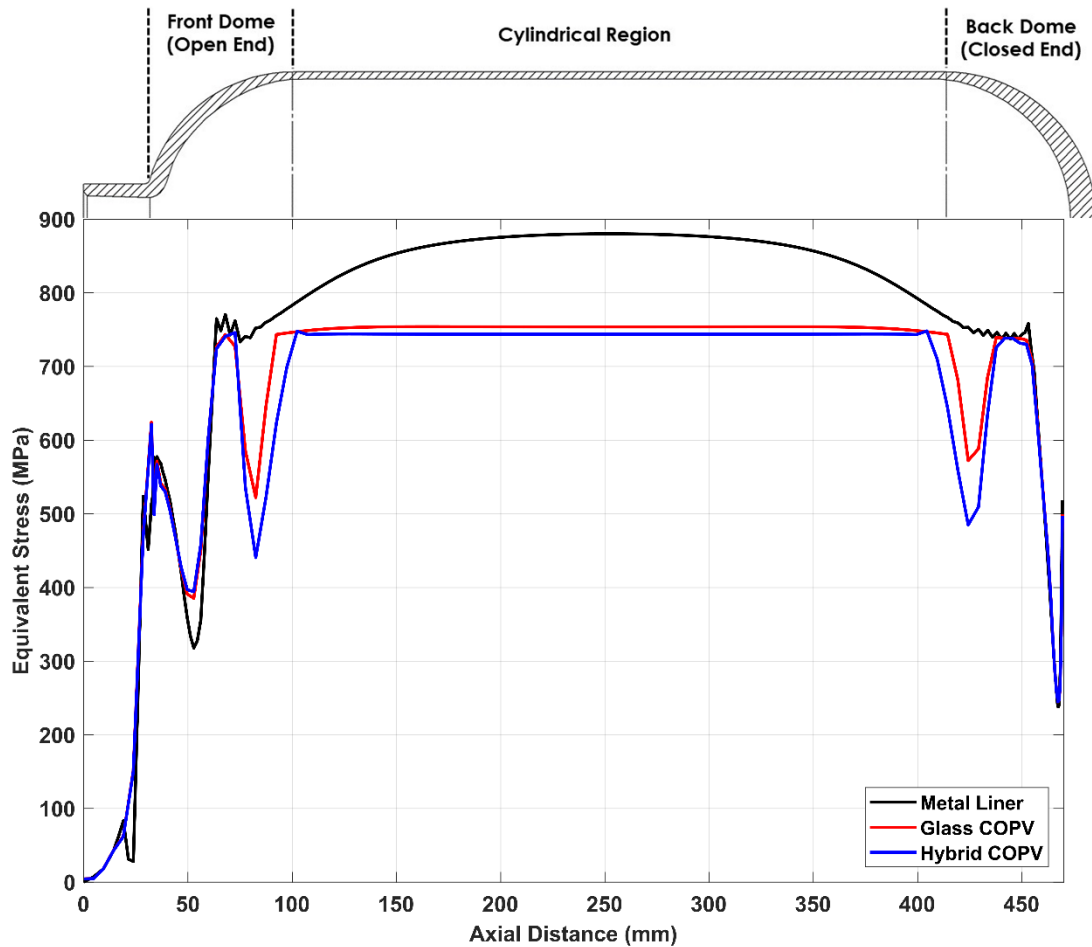
Figure 7.19. The equivalent stress vs. axial distance along the inner surface of the liner at 700 bar.

The experimental results and numerical predictions with their respective differences of the burst pressure of the produced vessels and the liner were given in Table 7.5. It is obviously seen that constructed 3D FE model with the Hashin FPF criterion and simple progressive failure, predicts in a range within about 8% of the experimental findings. The results of the numerical prediction were slightly higher in all cases, which were expected due to the fact that material inhomogeneity and manufacturing issues were not considered in the numerical model.

Table 7.5. The experimental results and numerical predictions of the burst pressure values

Specimen		Experimental Burst Pressure (bar)	Predicted FE Model Burst Pressure (bar)	Difference (%)
Steel Liner	Prototype 1	622	644	3.54
	Prototype 2	692		-6.94
GF (Glass fiber based) COPV	Prototype 1	919	952	3.59
	Prototype 2	879		8.30
Hybrid (Glass/carbon fiber based) COPV	Prototype 1	922	942	2.17
	Prototype 2	887		6.20

Although the hybridization of carbon hoop layers positively influences radial deformations and equivalent stress at the cylindrical section of the liner, both experimental and numerical burst results revealed that hybridization had no effect on the final burst pressure. This outcome can be explained by the difference of the stiffness between the carbon and glass fibers. In hybrid COPVs, due to their higher stiffness and lower elongation, the inner carbon fiber layers tend to carry load first; thus, reducing effective load-carrying capacity of the outermost glass / epoxy hoop plies. Consequently, lower stresses will occur at outermost hoop plies. Figure 7.20 shows a comparison in order to demonstrate this phenomenon. The curves belong to the outermost hoop ply which consists of glass / epoxy for both cases. As distinctly seen from the curves, significantly lower stresses occur in hybrid COPV at identical internal pressures:
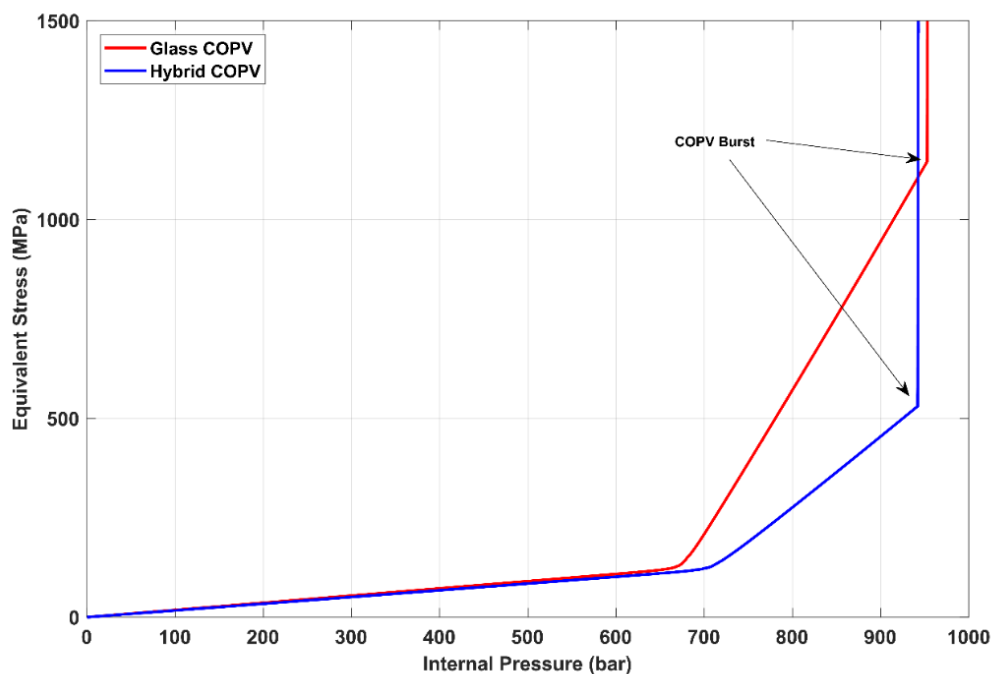
Figure 7.20. A comparison of the maximum equivalent stress vs. internal pressure at the outermost glass / epoxy layer for both types of COPVs.

Figure 7.21 shows a comparison of calculated Hashin fiber tensile failure indices of all plies to demonstrate this phenomenon. It was evident that stress accumulation in hoop plies was significantly faster than the helical plies in both types of COPV. It was also noteworthy to observe that two carbon fiber (CF) hoop layers in hybrid COPV significantly reduced the failure indices in helical plies and the outermost glass fiber (GF) layer.

The comparison between the hoop plies of both COPV types near burst were also made and shown in Figure 7.22. The progressive failure of the plies began when the

innermost hoop ply reach fiber tensile failure index of 1. This was followed by the sequential failures of the hoop plies from inner to the outermost direction. Finally, all helical layers immediately fail after all hoop plies lose their load-bearing ability.
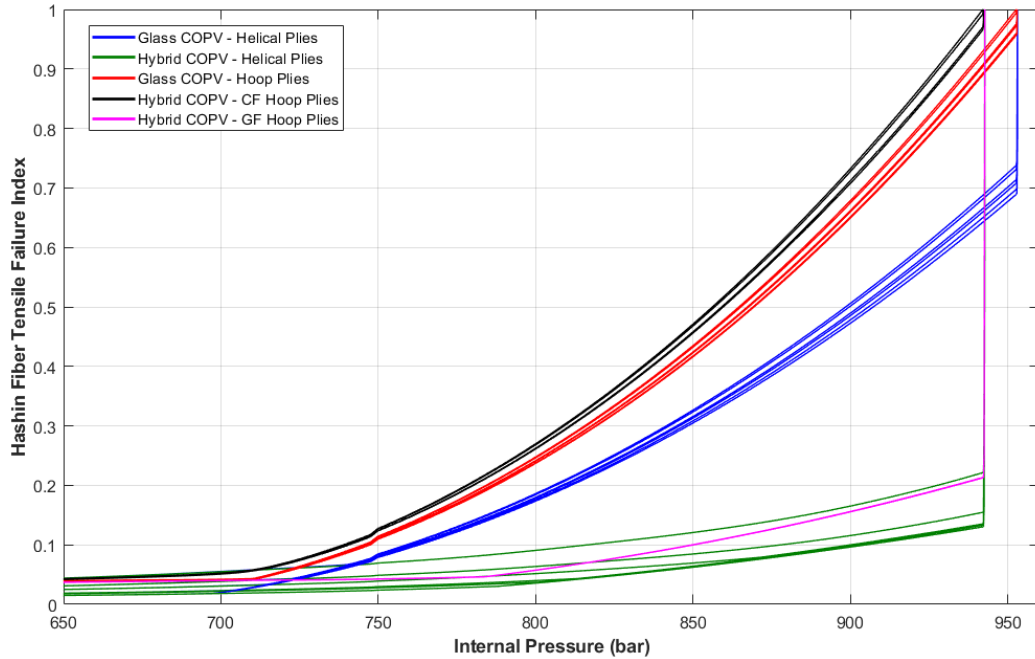
Figure 7.21. A comparison of the maximum equivalent stress vs. internal pressure at the outermost glass / epoxy layer for both types of COPVs
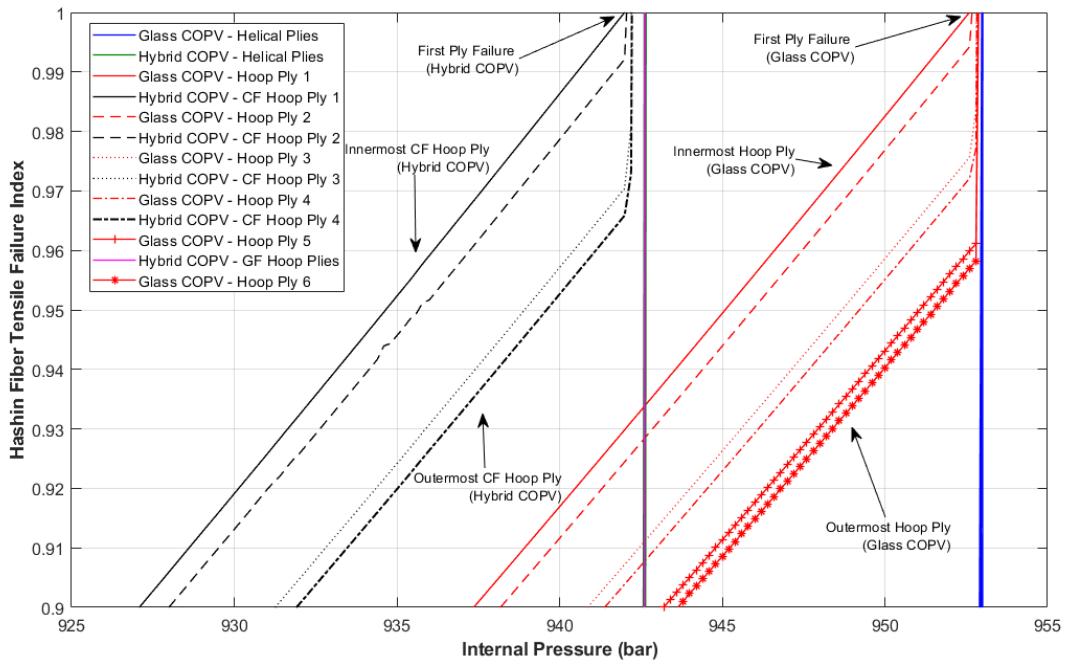
Figure 7.22. The comparison of failure indices of hoop plies of both COPV types near burst

7.6. FE Analysis – Al-based COPVs with Doily Layers

The experimental results and numerical predictions of the burst pressure of the Al-based liner COPVs with additions of composite reinforcement orientations and burst failure locations were given in Table 7.6. It is obviously seen that constructed 3D FE model with the Hashin FPF criterion and simple progressive failure, predicts in a range within about 7.2% of the experimental findings. The results of the numerical prediction were slightly lower in all cases, except the ALCF 8 specimen in which hoop composite layer thickness was calibrated (indicated as *). In contrast, the prediction of the location of the burst failure was strikingly different from the experimental results. This was contributed to the perfect bonding of the composite plies in the numerical simulations as in reality there might be epoxy rich regions and voids may occur, especially in the end dome sections with the higher number of doily layers.

Table 7.6. The experimental results and numerical predictions of the burst pressure values for the Al-based liner reinforced with carbon fiber / epoxy composite.

Specimen	Layer Orientation	Front Doily Layers	Aft Doily Layers	Exp. Burst (bar)	Exp. - Burst Location	FEA Burst (bar)	FEA Burst Location
ALCF 1	$[\pm11°]_9 / [\pm90°]_7$	-	-	1018	Front Dome (unsafe)	999	Front Dome (unsafe)
ALCF 2	$[\pm11°]_9 / [\pm90°]_8$	-	-	1050	Front Dome (unsafe)		
ALCF 3	$[\pm11°]_{12} / [\pm90°]_{11}$	-	-	1050	Front Dome (unsafe)		
ALCF 4	$[\pm11°]_{13} / [\pm90°]_{11}$	-	-	1050	Front Dome (unsafe)		
ALCF 5	$[\pm11°]_9 / [\pm90°]_7$	7	-	1146	Front Dome (unsafe)	1123	Cylindrical (safe)
ALCF 6	$[\pm11°]_9 / [\pm90°]_7$	11	-	1170	Front Dome (unsafe)	1124	Cylindrical (safe)
ALCF 7	$[\pm11°]_9 / [\pm90°]_7$	15	-	1264	Front Dome (unsafe)	1172	Aft Dome transition (unsafe)
ALCF 8	$[\pm11°]_9 / [\pm90°]_7$	17	-	1281	Aft Dome transition (unsafe)	1306*	Cylindrical (safe)
ALCF 9	$[\pm11°]_9 / [\pm90°]_7$	17	5	1330	Aft Dome to Cylindrical Region	-	-
ALCF 10	$[\pm11°]_9 / [\pm90°]_7$	17	9	1355	Cylindrical Region	-	-
ALCF 11	$[\pm11°]_9 / [\pm90°]_8$	17	9	1397	Front Dome to Cylindrical Region	-	-

It was also noteworthy to mention that the model for Al-based liner reinforced with CF / epoxy composite was still in development. Introducing a substantial number of

composite layers affects the computation time of the structural problem. Additionally, the transition region from the cylindrical to the aft dome region was problematic due to the sharp turn in the geometry of the dome. Similarly, the transition region from the frontal dome to the boss had a steep curvature in which composite build up greatly complicates the meshing of the composite section.

In Al-based liner COPVs, mechanical properties of CF reinforcement and the proper determination of helical and hoop layers were vital as the number of composite plies increases. Finally, it can be clearly said that the thickness variation of the liner material through the longitudinal direction significantly affects the burst pressure location of the simulation solution.

Due to the abovementioned reasons, the current model for the ALCF COPVs produced results for up to ALCF 8 specimen. The model was still calibrated to obtain a physically meaning solution for a higher number of composite plies as it is the case for ALCF 9 to ALCF 11 specimens.

CHAPTER 8

CONCLUDING REMARKS

Hydrogen is considered as the new energy carrier for the century for its high gravimetric energy density. But hydrogens very low volumetric energy density creates a considerable drawback for the acceptance of hydrogen as an energy carrier. Thus, the storage of hydrogen is extensively studied to improve the volumetric capabilities of the new energy carrier.

The demand for higher volumetric energy density and lower cost paves the way for new hydrogen storage techniques such as metal hydrides or adsorption with metal organic frames. Nevertheless, these new techniques are still in development, and physical-based storage is still the most feasible and standard method for high-pressure storage. While operating at cryogenic temperatures significantly improves the volumetric energy density of the hydrogen, the cost of maintaining these temperatures are still a challenge for the industry.

The simplicity and the practicality of compressed gaseous storage of hydrogen are very attractive for the industry and the scientific community. Increasing the working pressure of the pressure vessels demands advanced materials and manufacturing techniques. Utilizing composite materials with the filament winding manufacturing technique offer a solution to this problem.

Composite overwrapped pressure vessels are well-known and employed for gas storage since the 1960s. Increasing the working pressure of the vessels naturally requires winding of more composite materials and shifting for more carbon fiber usage. Fully composite overwrapped vessel types (Type-III and Type-IV) are suitable for pressures 350 bar and higher and broadly researched for possible higher pressures.

The working pressure of 700 bar provides a challenge for COPVs, due to the standard requirement of the burst pressure being at least two times of the working pressure. The burst pressure of 1400 bar without a load-sharing liner requires detailed and cautious modeling and manufacturing of the COPVs.

This study aims to approach the modeling of COPVs with two different approaches. With the first approach, the interlayer hybridization of the vessels was

investigated to obtain any positive hybridization effects and reduce the cost of the vessel. The second approach emphasizes on the maximizing the burst pressure of an aluminum liner with carbon fiber reinforcement.

Both approaches require similar procedures for the modeling of the COPVs. Metal vessels for both load sharing and non-loading sharing liners were obtained from the local manufacturers. The steel-based liners were directly purchased as they are already available products for other purposes. On the contrary, aluminum liners were successfully produced by the manufacturer on request, and several design decisions were made with the manufacturer for optimizing the liner for the filament winding manufacturing.

All materials involving this study, including the metal liners were experimentally evaluated, and their mechanical behavior was obtained by tensile testing. The obtained mechanical behavior of the specimens that were water-jet cut from the liners was provided modulus and the multilinear isotropic hardening data for the numerical model. When compared with the values found in the literature, the experimentally obtained values seemed to be lower. This might due to the manufacturing processes of the metal liners. It was observed that using the experimental values of the isotropic metal liner improved the burst pressure predictions of the numerical model.

In contrast, the tensile testing results of the filament wound composite were significantly lower than the accepted values in the literature. Simulations utilizing these experimental values for the composite shell of the COPVs dramatically reduces the accuracy of the strain behavior and the burst pressure predictions of the numerical simulations. It was thought that residual thermal stresses on the filament wound composite plates were the primary reason for the mechanical property deficiency.

The manufacturing of the COPVs began with dry winding trials. The transition to the wet winding introduced several manufacturing issues such as slippage of the rovings while winding. Furthermore, increasing the number of helical layers created new challenges as the geometry of the COPV drastically changes, and the areas where the rovings were attached were physically disappeared. Nevertheless, the burst pressure of 1330 bar was achieved with carbon fiber reinforced aluminum liner COPVs.

The validation process of the numerical model involves three aspects of the experimental findings; the strain behavior of the COPVs from several locations, the burst pressure, and the burst location. The strain behavior was successfully obtained with utilizing strain gages attached to the front, center, and the aft of the cylindrical section of the COPVs and the liners.

To investigate the interlayer hybridization effects on COPVs, glass fiber, and hybrid (glass/carbon) COPVs containing both helical and hoop layers were manufactured with filament winding technique. A progressive failure FEA model, featuring non-linear elastic-plastic behavior of isotropic liner material, thickness and fiber angle variation on the dome sections with progressive damage was developed. FEA model provided good correlations between experimental and numerical findings for steel liner and glass fiber COPVs. However, the results showed that carbon hoop layers introduced in hybrid COPVs do not have any significant effect on the experimental burst pressure values as compared those for entirely glass fiber COPVs. This phenomenon may be attributed to the stiffness difference of carbon and glass fiber reinforced layers in a back-to-back orientation and non-uniformity of mechanical properties of composite layers. Despite that, the developed numerical model was able to predict the burst pressures of all the COPVs and liners within %8 of the experimental results. In addition to that, the model has successfully located the failure locations and thus, determined the safety of the burst.

For the other aspect of this thesis study, achieving burst pressures as highest as possible was aimed. The number of composite reinforcement layers were increased significantly, and only carbon fibers were utilized. It was observed that liner thickness variations (especially in the front and aft dome and dome to boss transition sections), mechanical properties of the aluminum liner, physical limitations due to nature of the filament winding process and the geometry of the dome sections of the liner significantly affects the burst performance of the COPVs. It was observed that higher burst pressures than 1000 bar were not achievable without further modifications. Such modifications include doily layers as local reinforcements to the front and aft domes and the addition of polyurethane-based layer inside the aluminum liner to reduce the permeability of the COPV through the microcracks formed under high pressures. With these additions, COPVs capable of 1330 bar burst pressure was obtained. This result is very promising as the standards dictate two times the working pressure of 700 bar must be achieved as the burst pressure.

It is possible to achieve good internal pressure vs. strain correlations for the COPVs using a progressive failure analysis numerical model. Determination of burst pressures and safe/unsafe burst modes are also critical and possible with a proper FEA model. As revealed in this study, experimental validation of the numerical model featuring essential aspects of COPVs is fundamental for the future development of high-

pressure hydrogen COPVs, thus enabling widespread adoption of hydrogen usage as a clean energy source.

8.1. Future Studies

Considering the acceptance of hydrogen as a new energy carrier for the future demands further improvements for its storage. From a research and manufacturing point of view, there are specific ways to improve the gravimetric and volumetric energy density of the COPVs and to increase the safety of the COPVs for onboard applications.

From this study, it was observed that the geometry and the material quality of the linear greatly influence the burst performance and safety of the COPVs, especially in pressures higher than 1000 bar. Thus, liners with geometries possible for geodesic winding should be manufactured and modeled in future studies. Identical front and aft openings with proper dome curvature enable geodesic winding, reduce slippage, and increase possible winding angles. This also creates opportunities for optimization of the number of layers and layer orientations for reducing carbon fiber usage, thus reducing the cost and weight of COPVs. For metal liners, the thickness of the liner should be controlled and set correctly in order to prevent unsafe and premature bursts.

Type-IV vessels with thermoplastic liners might result in better strength-to-weight ratios. The study on this type of vessels should focus on the integration of the metal boss to the liner, the contact surface, and bonding between plastic liner and the composite shell.

Acquiring proper mechanical properties of the composite reinforcements by filament winding process is critical for modeling of the COPVs. The specimens should be obtained from a medium that must be representative of the composite shell manufactured by the filament winding with similar fiber and void volume fractions and without any residual stresses.

Filament winding manufacturing process can also be improved according to past experiences with previously manufactured COPVs and composite tubes. Modifications to the resin bath may result in improved wetting of fibers, decreasing the air bubbles introduced while wetting of the fibers and reducing the excess resin, thus increasing the fiber volume fraction.

For more accurate prediction of the burst pressure, burst location, and the strain

behavior of COPVs, the progressive damage analysis with continuum damage mechanics (CDM) technique should be studied. Furthermore, the interactive failure theories of Puck, LaRC03, and LaRC04 should be compared with the already studied Hashin failure criterion. Implementation of custom material and damage models to the commercial FEA packages will be required for previously mentioned damage onset and evolution theories. Lastly, microscale modeling of the reinforcement might significantly improve the accuracy of the model with modeling of the experimentally observed microstructure of the composite reinforcement.

Possible interyarn and interfiber hybridization techniques coupled with the previously mentioned microscale modeling may result in lowering the cost of the COPVs.

REFERENCES

(1)   Carrel, P.; Martin, M. G7 Leaders Bid "Auf Wiedersehen" to Carbon Fuels. *Reuters*. June 8, 2015.

(2)   Sheffield, J.W., Sheffield, C. *Assessment of Hydrogen Energy for Sustainable Development*; Sheffield, J. W., Sheffield, Ç., Eds.; NATO Science for Peace and Security Series C: Environmental Security; Springer Netherlands: Dordrecht, 2007. https://doi.org/10.1007/978-1-4020-6442-5.

(3)   Johnston, B.; Mayo, M. C.; Khare, A. Hydrogen: The Energy Source for the 21st Century. *Technovation* **2005**, *25* (6), 569–585. https://doi.org/10.1016/j.technovation.2003.11.005.

(4)   Hosseini, M.; Dincer, I.; Naterer, G. F.; Rosen, M. a. Thermodynamic Analysis of Filling Compressed Gaseous Hydrogen Storage Tanks. *Int. J. Hydrogen Energy* **2012**, *37* (6), 5063–5071. https://doi.org/10.1016/j.ijhydene.2011.12.047.

(5)   Jain, I. P. Hydrogen the Fuel for 21st Century. *Int. J. Hydrogen Energy* **2009**, *34* (17), 7368–7378. https://doi.org/10.1016/j.ijhydene.2009.05.093.

(6)   Gurz, M.; Baltacioglu, E.; Hames, Y.; Kaya, K. The Meeting of Hydrogen and Automotive: A Review. *Int. J. Hydrogen Energy* **2017**, *42* (36), 23334–23346. https://doi.org/10.1016/j.ijhydene.2017.02.124.

(7)   Ayaji-Oyakhire, O. *Hydrogen - Untapped Energy?*; 2012.

(8)   US Deparment of Energy Office of Energy Efficiency & Renewable Energy. Hydrogen Storage - Fuel Cell Technologies https://www.energy.gov/eere/fuelcells/hydrogen-storage (accessed Jul 3, 2019).

(9)   Enerdata. *World Energy Technology Outlook to 2050*; 2010.

(10)   Zheng, J.; Liu, X.; Xu, P.; Liu, P.; Zhao, Y.; Yang, J. Development of High Pressure Gaseous Hydrogen Storage Technologies. *Int. J. Hydrogen Energy* **2012**, *37* (1), 1048–1057. https://doi.org/10.1016/j.ijhydene.2011.02.125.

(11)   Chapelle, D.; Perreux, D. Optimal Design of a Type 3 Hydrogen Vessel: Part I—Analytic Modelling of the Cylindrical Section. *Int. J. Hydrogen Energy* **2006**, *31* (5), 627–638. https://doi.org/10.1016/j.ijhydene.2005.06.012.

(12)   Bertin, M.; Touchard, F.; Lafarie-Frenot, M.-C. Experimental Study of the Stacking Sequence Effect on Polymer/Composite Multi-Layers Submitted to Thermomechanical Cyclic Loadings. *Int. J. Hydrogen Energy* **2010**, *35* (20), 11397–11404. https://doi.org/10.1016/j.ijhydene.2010.07.018.

(13)   Barthelemy, H.; Weber, M.; Barbier, F. Hydrogen Storage: Recent Improvements and Industrial Perspectives. *Int. J. Hydrogen Energy* **2017**, *42* (11), 7254–7262. https://doi.org/10.1016/j.ijhydene.2016.03.178.

(14) Red, C. Pressure Vessels for Alternative Fuels, 2014-2023. *Composites World*. 2014.

(15) Ghouaoula, A.; Hocine, A.; Chapelle, D.; Karaachira, F.; Boubakar, M. L. Analytical Prediction of Damage in the Composite Part of a Type-3 Hydrogen Storage Vessel. *Mech. Compos. Mater.* **2012**, *48* (1), 77–88.

(16) Ichikawa, T.; Hanada, N.; Isobe, S.; Leng, H.; Fujii, H. Composite Materials Based on Light Elements for Hydrogen Storage. *Mater. Trans.* **2005**, *46* (1), 1–14. https://doi.org/10.2320/matertrans.46.1.

(17) Lawrence Livermore National Laboratory. A Solid Hydrogen-Storage Solution https://str.llnl.gov/2018-01/wood (accessed Jul 3, 2019).

(18) Ahluwalia, R. K.; Hua, T. Q.; Peng, J.-K.; Lasher, S.; McKenney, K.; Sinha, J. *Technical Assessment of Cyro-Compressed Hydrogen Storage Tank System for Automotive Applications*; 2009.

(19) Gardiner, G. SpaceX announces COPV's role in September rocket explosion https://www.compositesworld.com/blog/post/spacex-announces-copvs-role-in-sept-rocket-explosion (accessed Jul 7, 2019).

(20) Apak, S.; Atay, E.; Tuncer, G. Renewable Hydrogen Energy and Energy Efficiency in Turkey in the 21st Century. *Int. J. Hydrogen Energy* **2017**, *42* (4), 2446–2452. https://doi.org/10.1016/j.ijhydene.2016.05.043.

(21) Kaw, A. K. *Mechanics of Composite Materials*, 2nd Editio.; Taylor & Francis Group, 1997.

(22) Middleton, B. Composites: Manufacture and Application. In *Design and Manufacture of Plastic Components for Multifunctionality*; Elsevier, 2016; pp 53–101. https://doi.org/10.1016/B978-0-323-34061-8.00003-X.

(23) Chawla, K. K. *Composite Materials*, 3rd Editio.; Springer New York: New York, NY, 2012. https://doi.org/10.1007/978-0-387-74365-3.

(24) Mallick, P. K. *Fiber-Reinforced Composites*; CRC Press, 2007.

(25) Long, A. *Design and Manufacture of Textile Composites*; CRC Press, 2005.

(26) Chung, D. D. L. *Composite Materials*, Second.; Springer, 2010. https://doi.org/10.1007/978-1-84882-831-5.

(27) Hill, E. H. *The Finite Element Method for Mechanics of Solids with ANSYS Applications*, 1st Editio.; Benaroya, H., Ed.; CRC Press, 2011.

(28) Zienkiewicz, O. C.; Taylor, R. L.; Fox, D. D. *The Finite Element Method for Solid and Structural Mechanics*, Seventh Ed.; Elsevier, 2014. https://doi.org/10.1016/C2009-0-26332-X.

(29) ANSYS Inc. ANSYS® Mechanical APDL Theory Reference, Release 17.2.

(30)   Murugesan, N.; Rajamohan, V. Prediction of Progressive Ply Failure of Laminated Composite Structures: A Review. *Arch. Comput. Methods Eng.* **2017**, *24* (4), 841–853. https://doi.org/10.1007/s11831-016-9191-2.

(31)   Hill, R. A Theory of the Yielding and Plastic Flow of Anisotropic Metals. *Proc. R. Soc. London. Ser. A. Math. Phys. Sci.* **1948**, *193* (1033), 281–297. https://doi.org/10.1098/rspa.1948.0045.

(32)   Azzi, V. D.; Tsai, S. W. Anisotropic Strength of Composites. *Exp. Mech.* **1965**, *5* (9), 283–288. https://doi.org/10.1007/BF02326292.

(33)   Tsai, S. W.; Wu, E. M. A General Theory of Strength for Anisotropic Materials. *J. Compos. Mater.* **1971**, *5* (1), 58–80. https://doi.org/10.1177/002199837100500106.

(34)   Hashin, Z. Failure Criteria for Unidirectional Fiber Composites. *J. Appl. Mech.* **1980**, *47* (2), 329. https://doi.org/10.1115/1.3153664.

(35)   Doitrand, A.; Fagiano, C.; Chiaruttini, V.; Leroy, F. H.; Mavel, A.; Hirsekorn, M. Experimental Characterization and Numerical Modeling of Damage at the Mesoscopic Scale of Woven Polymer Matrix Composites under Quasi-Static Tensile Loading. *Compos. Sci. Technol.* **2015**, *119*, 1–11. https://doi.org/10.1016/j.compscitech.2015.09.015.

(36)   Puck, A.; Schürmann, H. Failure Analysis of FRP Laminates by Means of Physically Based Phenomenological Models. *Compos. Sci. Technol.* **1998**, *58*, 1045–1067. https://doi.org/10.1016/B978-008044475-8/50028-7.

(37)   Puck, A.; Kopp, J.; Knops, M. Guidelines for the Determination of the Parameters in Puck's Action Plane Strength Criterion. *Compos. Sci. Technol.* **2002**, *62* (3), 371–378. https://doi.org/10.1016/S0266-3538(01)00202-0.

(38)   Davila, C. G.; Camanho, P. P.; Rose, C. A. Failure Criteria for FRP Laminates. *J. Compos. Mater.* **2005**, *39* (4), 323–345. https://doi.org/10.1177/0021998305046452.

(39)   Pinho, S. T.; Dávila, C. G.; Camanho, P. P.; Iannucci, L.; Robinson, P. Failure Models and Criteria for FRP Under In-Plane or Three-Dimensional Stress States Including Shear Non-Linearity. *NASA/TM-2005-213530* **2005**, No. February, 68. https://doi.org/NASA/TM-2005-213530.

(40)   Marulo, F.; Guida, M.; Maio, L.; Ricci, F. Numerical Simulations and Experimental Experiences of Impact on Composite Structures. In *Dynamic Response and Failure of Composite Materials and Structures*; Elsevier, 2017; pp 85–125. https://doi.org/10.1016/B978-0-08-100887-4.00003-2.

(41)   Jorgensen, S. W. Hydrogen Storage Tanks for Vehicles: Recent Progress and Current Status. *Curr. Opin. Solid State Mater. Sci.* **2011**, *15* (2), 39–43. https://doi.org/10.1016/j.cossms.2010.09.004.

(42)   Rafiee, M. A.; Rafiee, J.; Wang, Z.; Song, H.; Yu, Z.-Z.; Koratkar, N. Enhanced Mechanical Properties of Nanocomposites at Low Graphene Content. *ACS Nano*

2009, *3* (12), 3884–3890. https://doi.org/10.1021/nn9010472.

(43) Rongguo Wang; Weicheng Jiao; Wenbo Liu; Fan Yang. A New Method for Predicting Dome Thickness of Composite Pressure Vessels. *J. Reinf. Plast. Compos.* **2010**, *29* (22), 3345–3352. https://doi.org/10.1177/0731684410376330.

(44) Bunsell, A. R. Composite Pressure Vessels Supply an Answer to Transport Problems. *Reinf. Plast.* **2006**, *50* (2), 38–41. https://doi.org/10.1016/S0034-3617(06)70914-6.

(45) Barthélémy, H. Hydrogen Storage – Industrial Prospectives. *Int. J. Hydrogen Energy* **2012**, *37* (22), 17364–17372. https://doi.org/10.1016/j.ijhydene.2012.04.121.

(46) Roh, H. S.; Hua, T. Q.; Ahluwalia, R. K. Optimization of Carbon Fiber Usage in Type 4 Hydrogen Storage Tanks for Fuel Cell Automobiles. *Int. J. Hydrogen Energy* **2013**, *38* (29), 12795–12802. https://doi.org/10.1016/j.ijhydene.2013.07.016.

(47) Hua, T. Q.; Roh, H.-S.; Ahluwalia, R. K. Performance Assessment of 700-Bar Compressed Hydrogen Storage for Light Duty Fuel Cell Vehicles. *Int. J. Hydrogen Energy* **2017**, *42* (40), 25121–25129. https://doi.org/10.1016/j.ijhydene.2017.08.123.

(48) Musthak, M.; Valli, P. M.; Rao, S. N. Prediction of Transverse Directional Strains and Stresses of Filament Wound Composite Pressure Vessel by Using Higher Order Shear Deformation Theories. *Int. J. Compos. Mater.* **2016**, *6* (3), 79–87. https://doi.org/10.5923/j.cmaterials.20160603.03.

(49) Madhavi, M.; Venkat, R. Predicting Structural Behavior of Filament Wound Composite Pressure Vessel Using Three Dimensional Shell Analysis. *J. Inst. Eng. Ser. C* **2014**, *95* (1), 41–50. https://doi.org/10.1007/s40032-014-0094-4.

(50) Yao, D.; Cai, L.; Bao, C. A New Approach on Necking Constitutive Relationships of Ductile Materials at Elevated Temperatures. *Chinese J. Aeronaut.* **2016**, *29* (6), 1626–1634. https://doi.org/10.1016/j.cja.2016.10.011.

(51) Liu, P. F.; Zheng, J. Y. Finite Element Analysis of Tensile Behavior of Ductile Steel with Defects. *J. Fail. Anal. Prev.* **2010**, *10* (3), 212–217. https://doi.org/10.1007/s11668-010-9337-8.

(52) Huang, X.; Chen, Y.; Lin, K.; Mihsein, M.; Kibble, K.; Hall, R. Burst Strength Analysis of Casing With Geometrical Imperfections. *J. Press. Vessel Technol.* **2007**, *129* (4), 763. https://doi.org/10.1115/1.2767370.

(53) Paul, S. K.; Roy, S.; Sivaprasad, S.; Bar, H. N.; Tarafder, S. Identification of Post-Necking Tensile Stress–Strain Behavior of Steel Sheet: An Experimental Investigation Using Digital Image Correlation Technique. *J. Mater. Eng. Perform.* **2018**, *27* (11), 5736–5743. https://doi.org/10.1007/s11665-018-3701-3.

(54) Tardif, N.; Kyriakides, S. Determination of Anisotropy and Material Hardening for Aluminum Sheet Metal. *Int. J. Solids Struct.* **2012**, *49* (25), 3496–3506.

https://doi.org/10.1016/j.ijsolstr.2012.01.011.

(55) Barlat, F.; Aretz, H.; Yoon, J. W.; Karabin, M. E.; Brem, J. C.; Dick, R. E. Linear Transfomation-Based Anisotropic Yield Functions. *Int. J. Plast.* **2005**, *21* (5), 1009–1039. https://doi.org/10.1016/j.ijplas.2004.06.004.

(56) Xue, L.; Widera, G. E. O.; Sang, Z. Burst Analysis of Cylindrical Shells. *J. Press. Vessel Technol.* **2008**, *130* (1), 014502. https://doi.org/10.1115/1.2826454.

(57) Brabin, T. A.; Christopher, T.; Nageswara Rao, B. Bursting Pressure of Mild Steel Cylindrical Vessels. *Int. J. Press. Vessel. Pip.* **2011**, *88* (2–3), 119–122. https://doi.org/10.1016/j.ijpvp.2011.01.001.

(58) Korkolis, Y. P.; Kyriakides, S.; Giagmouris, T.; Lee, L.-H. Constitutive Modeling and Rupture Predictions of Al-6061-T6 Tubes Under Biaxial Loading Paths. *J. Appl. Mech.* **2010**, *77* (6), 064501. https://doi.org/10.1115/1.4001940.

(59) ISO. ISO/TS 15869:2009 Gaseous Hydrogen and Hydrogen Blends \ Land Vehicle Fuel Tanks. 2009.

(60) Hocine, A.; Chapelle, D.; Boubakar, M. L.; Benamar, A.; Bezazi, A. Experimental and Analytical Investigation of the Cylindrical Part of a Metallic Vessel Reinforced by Filament Winding While Submitted to Internal Pressure. *Int. J. Press. Vessel. Pip.* **2009**, *86* (10), 649–655. https://doi.org/10.1016/j.ijpvp.2009.06.002.

(61) Shao, Y.; Betti, A.; Carvelli, V.; Fujii, T.; Okubo, K.; Shibata, O.; Fujita, Y. High Pressure Strength of Carbon Fibre Reinforced Vinylester and Epoxy Vessels. *Compos. Struct.* **2016**, *140*, 147–156. https://doi.org/10.1016/j.compstruct.2015.12.053.

(62) Cohen, D. Influence of Filament Winding Parameters on Composite Vessel Quality and Strength. *Compos. Part A Appl. Sci. Manuf.* **1997**, *28* (12), 1035–1047. https://doi.org/10.1016/S1359-835X(97)00073-0.

(63) Cohen, D.; Mantell, S. C.; Zhao, L. The Effect of Fiber Volume Fraction on Filament Wound Composite Pressure Vessel Strength. *Compos. Part B Eng.* **2001**, *32* (5), 413–429. https://doi.org/10.1016/S1359-8368(01)00009-9.

(64) Liu, P. F.; Chu, J. K.; Hou, S. J.; Xu, P.; Zheng, J. Y. Numerical Simulation and Optimal Design for Composite High-Pressure Hydrogen Storage Vessel: A Review. *Renew. Sustain. Energy Rev.* **2012**, *16* (4), 1817–1827. https://doi.org/10.1016/j.rser.2012.01.006.

(65) Francescato, P.; Gillet, A.; Leh, D.; Saffré, P. Comparison of Optimal Design Methods for Type 3 High-Pressure Storage Tanks. *Compos. Struct.* **2012**, *94* (6), 2087–2096. https://doi.org/10.1016/j.compstruct.2012.01.018.

(66) Leh, D.; Saffré, P.; Francescato, P.; Arrieux, R.; Villalonga, S. A Progressive Failure Analysis of a 700-Bar Type IV Hydrogen Composite Pressure Vessel. *Int. J. Hydrogen Energy* **2015**, *40* (38), 13206–13214. https://doi.org/10.1016/j.ijhydene.2015.05.061.

(67)   Xu, P.; Zheng, J. Y.; Liu, P. F. Finite Element Analysis of Burst Pressure of Composite Hydrogen Storage Vessels. *Mater. Des.* **2009**, *30* (7), 2295–2301. https://doi.org/10.1016/j.matdes.2009.03.006.

(68)   Alcántar, V.; Ledesma, S.; Aceves, S. M.; Ledesma, E.; Saldaña, A. Optimization of Type III Pressure Vessels Using Genetic Algorithm and Simulated Annealing. *Int. J. Hydrogen Energy* **2017**, *42* (31), 20125–20132. https://doi.org/10.1016/j.ijhydene.2017.06.146.

(69)   Kim, C.-U.; Hong, C.-S.; Kim, C.-G.; Kim, J.-Y. Optimal Design of Filament Wound Type 3 Tanks under Internal Pressure Using a Modified Genetic Algorithm. *Compos. Struct.* **2005**, *71* (1), 16–25. https://doi.org/10.1016/j.compstruct.2004.09.006.

(70)   Park, J. S.; Hong, C. S.; Kim, C. G.; Kim, C. U. Analysis of Filament Wound Composite Structures Considering the Change of Winding Angles through the Thickness Direction. *Compos. Struct.* **2002**, *55* (1), 63–71. https://doi.org/10.1016/S0263-8223(01)00137-4.

(71)   Almeida, J. H. S.; Faria, H.; Marques, A. T.; Amico, S. C. Load Sharing Ability of the Liner in Type III Composite Pressure Vessels under Internal Pressure. *J. Reinf. Plast. Compos.* **2014**, *33* (24), 2274–2286. https://doi.org/10.1177/0731684414560221.

(72)   Swolfs, Y.; Gorbatikh, L.; Verpoest, I. Fibre Hybridisation in Polymer Composites: A Review. *Compos. Part A Appl. Sci. Manuf.* **2014**, *67*, 181–200. https://doi.org/10.1016/j.compositesa.2014.08.027.

(73)   Mahdi, E.; Hamouda, A. M. .; Sahari, B. .; Khalid, Y. . Effect of Hybridisation on Crushing Behaviour of Carbon/Glass Fibre/Epoxy Circular–Cylindrical Shells. *J. Mater. Process. Technol.* **2003**, *132* (1–3), 49–57. https://doi.org/10.1016/S0924-0136(02)00260-1.

(74)   Kobayashi, S.; Imai, T.; Wakayama, S. Burst Strength Evaluation of the FW-CFRP Hybrid Composite Pipes Considering Plastic Deformation of the Liner. *Compos. Part A Appl. Sci. Manuf.* **2007**, *38* (5), 1344–1353. https://doi.org/10.1016/j.compositesa.2006.10.011.

(75)   Gemï, L. Investigation of the Effect of Stacking Sequence on Low Velocity Impact Response and Damage Formation in Hybrid Composite Pipes under Internal Pressure. A Comparative Study. *Compos. Part B Eng.* **2018**, *153* (July), 217–232. https://doi.org/10.1016/j.compositesb.2018.07.056.

(76)   Prusty, R. K.; Rathore, D. K.; Singh, B. P.; Mohanty, S. C.; Mahato, K. K.; Ray, B. C. Experimental Optimization of Flexural Behaviour through Inter-Ply Fibre Hybridization in FRP Composite. *Constr. Build. Mater.* **2016**, *118*, 327–336. https://doi.org/10.1016/j.conbuildmat.2016.05.054.

(77)   Zheng, J. Y.; Liu, P. F. Elasto-Plastic Stress Analysis and Burst Strength Evaluation of Al-Carbon Fiber/Epoxy Composite Cylindrical Laminates. *Comput. Mater. Sci.* **2008**, *42* (3), 453–461. https://doi.org/10.1016/j.commatsci.2007.09.011.

(78)   Hu, J.; Chandrashekhara, K. Fracture Analysis of Hydrogen Storage Composite Cylinders with Liner Crack Accounting for Autofrettage Effect. *Int. J. Hydrogen Energy* **2009**, *34* (8), 3425–3435. https://doi.org/10.1016/j.ijhydene.2009.01.094.

(79)   Liu, P. F.; Xing, L. J.; Zheng, J. Y. Failure Analysis of Carbon Fiber/Epoxy Composite Cylindrical Laminates Using Explicit Finite Element Method. *Compos. Part B Eng.* **2014**, *56*, 54–61. https://doi.org/10.1016/j.compositesb.2013.08.017.

(80)   Burov, A. E.; Lepihin, A. M.; Makhutov, N. A.; Moskvichev, V. V. Numerical Analysis of Stress-Strain State and Strength of Metal Lined Composite Overwrapped Pressure Vessel. *Strength Mater.* **2017**, *49* (5), 666–675. https://doi.org/10.1007/s11223-017-9912-2.

(81)   Berro Ramirez, J. P.; Halm, D.; Grandidier, J.-C.; Villalonga, S. A Fixed Directions Damage Model for Composite Materials Dedicated to Hyperbaric Type IV Hydrogen Storage Vessel – Part II: Validation on Notched Structures. *Int. J. Hydrogen Energy* **2015**, *40* (38), 13174–13182. https://doi.org/10.1016/j.ijhydene.2015.06.014.

(82)   Rafiee, R.; Torabi, M. A. Stochastic Prediction of Burst Pressure in Composite Pressure Vessels. *Compos. Struct.* **2018**, *185* (October 2017), 573–583. https://doi.org/10.1016/j.compstruct.2017.11.068.

(83)   Son, D.-S.; Hong, J.-H.; Chang, S.-H. Determination of the Autofrettage Pressure and Estimation of Material Failures of a Type III Hydrogen Pressure Vessel by Using Finite Element Analysis. *Int. J. Hydrogen Energy* **2012**, *37* (17), 12771–12781. https://doi.org/10.1016/j.ijhydene.2012.06.044.

(84)   Berro Ramirez, J. P.; Halm, D.; Grandidier, J.-C.; Villalonga, S.; Nony, F. 700 Bar Type IV High Pressure Hydrogen Storage Vessel Burst – Simulation and Experimental Validation. *Int. J. Hydrogen Energy* **2015**, *40* (38), 13183–13192. https://doi.org/10.1016/j.ijhydene.2015.05.126.

(85)   Magneville, B.; Gentilleau, B.; Villalonga, S.; Nony, F.; Galiano, H. Modeling, Parameters Identification and Experimental Validation of Composite Materials Behavior Law Used in 700 Bar Type IV Hydrogen High Pressure Storage Vessel. *Int. J. Hydrogen Energy* **2015**, *40* (38), 13193–13205. https://doi.org/10.1016/j.ijhydene.2015.06.121.

(86)   ASTM International. ASTM E8/E8M-16a - Standard Test Methods for Tension Testing of Metallic Materials. 2016. https://doi.org/10.1520/E0008_E0008M-16A.

(87)   Materials SA. CADWIND V9 User Manual. Material SA: Brussels.

(88)   Harada, S.; Arai, Y.; Araki, W.; Iijima, T.; Kurosawa, A.; Ohbuchi, T.; Sasaki, N. A Simplified Method for Predicting Burst Pressure of Type III Filament-Wound CFRP Composite Vessels Considering the Inhomogeneity of Fiber Packing. *Compos. Struct.* **2018**, *190*, 79–90. https://doi.org/10.1016/J.COMPSTRUCT.2018.02.011.

(89) Cho, S.; Kim, K.; Lee, S.-K.; Jung, G.; Lee, S.; Lyu, S. Effect of Dome Curvature on Failure Mode of Type4 Composite Pressure Vessel. *Int. J. Precis. Eng. Manuf.* **2018**, *19* (3), 405–410. https://doi.org/10.1007/s12541-018-0048-5.

(90) ANSYS Inc. ANSYS® Academic Research Mechanical, Release 17.2.

(91) Liao, B.; Wang, D.; Jia, L.; Zheng, J.; Gu, C. Continuum Damage Modeling and Progressive Failure Analysis of a Type III Composite Vessel by Considering the Effect of Autofrettage. *J. Zhejiang Univ. A* **2018**, *1775* (2016), 1–14. https://doi.org/10.1631/jzus.A1800152.

(92) Toh, W.; Tan, L. Bin; Tse, K. M.; Giam, A.; Raju, K.; Lee, H. P.; Tan, V. B. C. Material Characterization of Filament-Wound Composite Pipes. *Compos. Struct.* **2018**, *206* (July 2017), 474–483. https://doi.org/10.1016/j.compstruct.2018.08.049.

(93) Hashin, Z.; Rotem, A. A Fatigue Failure Criterion for Fiber Reinforced Materials. *J. Compos. Mater.* **1973**, *7* (4), 448–464. https://doi.org/10.1177/002199837300700404.

(94) El-Sisi, A. E.-D. A.; El-Emam, H. M.; Salim, H. A.; Sallam, H. E.-D. M. Efficient 3D Modeling of Damage in Composite Materials. *J. Compos. Mater.* **2015**, *49* (7), 817–828. https://doi.org/10.1177/0021998314525983.

(95) Wang, L.; Zheng, C.; Luo, H.; Wei, S.; Wei, Z. Continuum Damage Modeling and Progressive Failure Analysis of Carbon Fiber/Epoxy Composite Pressure Vessel. *Compos. Struct.* **2015**, *134* (August), 475–482. https://doi.org/10.1016/j.compstruct.2015.08.107.

(96) Rafiee, R.; Torabi, M. A.; Maleki, S. Investigating Structural Failure of a Filament-Wound Composite Tube Subjected to Internal Pressure: Experimental and Theoretical Evaluation. *Polym. Test.* **2018**, *67* (March), 322–330. https://doi.org/10.1016/j.polymertesting.2018.03.020.

(97) Pietropaoli, E. Progressive Failure Analysis of Composite Structures Using a Constitutive Material Model (USERMAT) Developed and Implemented in ANSYS ©. *Appl. Compos. Mater.* **2012**, *19* (3–4), 657–668. https://doi.org/10.1007/s10443-011-9220-0.

(98) Ortiz, D.; Abdelshehid, M.; Dalton, R.; Soltero, J.; Clark, R.; Hahn, M.; Lee, E.; Lightell, W.; Pregger, B.; Ogren, J.; et al. Effect of Cold Work on the Tensile Properties of 6061, 2024, and 7075 Al Alloys. *J. Mater. Eng. Perform.* **2007**, *16* (5), 515–520. https://doi.org/10.1007/s11665-007-9074-7.

APPENDIX A

MATLAB PROGRAMMING SCRIPTS

A.1. MATLAB Script for evaluating data obtained from FEA solution

```
clear;clc;format compact;

co = [0 0 1;
      0 0.5 0;
      1 0 0;
      0 0.75 0.75;
      0.75 0 0.75;
      0.75 0.75 0;
      0.25 0.25 0.25
       0    0.4470   0.7410;
      0.8500   0.3250   0.0980;
      0.9290   0.6940   0.1250;
      0.4940   0.1840   0.5560;
      0.4660   0.6740   0.1880;
      0.3010   0.7450   0.9330;
      0.6350   0.0780   0.1840];
set(groot,'defaultAxesColorOrder',co)

[num,sheet_file,raw]=xlsread('AL_case_study_v3','sheet_names','A1:B100
');

full_data0=xlsread('AL_case_study_v3',sheet_file{9,1},'A5:CN2000');

exp_L1=full_data0(:,1);
exp_L1(isnan(exp_L1)) = [];
exp_L1=exp_L1(:,1)-exp_L1(1,1);

exp_T1=full_data0(:,2);
exp_T1(isnan(exp_T1)) = [];
exp_T1=exp_T1(:,1)-exp_T1(1,1);

exp_L2=full_data0(:,3);
exp_L2(isnan(exp_L2)) = [];
exp_L2=exp_L2(:,1)-exp_L2(1,1);

exp_T2=full_data0(:,4);
exp_T2(isnan(exp_T2)) = [];
exp_T2=exp_T2(:,1)-exp_T2(1,1);

exp_L3=full_data0(:,5);
exp_L3(isnan(exp_L3)) = [];
exp_L3=exp_L3(:,1)-exp_L3(1,1);

exp_T3=full_data0(:,6);
exp_T3(isnan(exp_T3)) = [];
exp_T3=exp_T3(:,1)-exp_T3(1,1);

time_sg=full_data0(:,7);
```

```
time_sg(isnan(time_sg)) = [];
time_sg=time_sg(:,1)-time_sg(1,1);


time_p=full_data0(:,8);
time_p(isnan(time_p)) = [];
time_p=time_p(:,1)-time_p(1,1);


pressure=full_data0(:,9);
pressure(isnan(pressure)) = [];
pressure=pressure(:,1)-pressure(1,1);


burst_pressure=max(pressure)


figure(1);plot(time_p,pressure)
title('Pressure vs. Time')
xlabel('Time')
ylabel('Pressure(bar)')


figure(2);plot(time_sg,exp_L1,time_sg,exp_L2,time_sg,exp_L3,time_sg,ex
p_T1,time_sg,exp_T2,time_sg,exp_T3)
title('Strain vs. Time')
xlabel('Time (s)')
ylabel('Strain (mm/mm)')
legend('L1','L2','L3','T1','T2','T3')


pressure_fit=fit(time_p,pressure,'linearinterp');


p_sg=feval(pressure_fit,time_sg);


figure(3);plot(exp_L1,p_sg,'-',exp_L2,p_sg,'-',exp_L3,p_sg,'-
','LineWidth',1.5)
ylabel('Pressure (bar)','FontSize',12,'FontWeight','bold')
xlabel('Axial Strain (mm/mm)','FontSize',12,'FontWeight','bold')
legend('L1','L2','L3','Location','southeast')


figure(4);plot(exp_T1,p_sg,'-',exp_T2,p_sg,'-',exp_T3,p_sg,'-
','LineWidth',1.5)
ylabel('Pressure (bar)','FontSize',12,'FontWeight','bold')
xlabel('Hoop Strain (mm/mm)','FontSize',12,'FontWeight','bold')
legend('T1','T2','T3','Location','southeast')

ansys_pressure=10*full_data0(:,13);
ansys_pressure(isnan(ansys_pressure)) = [];
ansys_eqstress=full_data0(:,17);
ansys_eqstress(isnan(ansys_eqstress)) = [];
ansys_1X=full_data0(:,18);
ansys_1X(isnan(ansys_1X)) = [];
ansys_1Y=full_data0(:,19);
ansys_1Y(isnan(ansys_1Y)) = [];
ansys_1Z=full_data0(:,20);
ansys_1Z(isnan(ansys_1Z)) = [];
ansys_2X=full_data0(:,29);
ansys_2X(isnan(ansys_2X)) = [];
ansys_2Y=full_data0(:,30);
ansys_2Y(isnan(ansys_2Y)) = [];
ansys_2Z=full_data0(:,31);
ansys_2Z(isnan(ansys_2Z)) = [];
ansys_3X=full_data0(:,40);
ansys_3X(isnan(ansys_3X)) = [];
ansys_3Y=full_data0(:,41);
```

```matlab
ansys_3Y(isnan(ansys_3Y)) = [];
ansys_3Z=full_data0(:,42);
ansys_3Z(isnan(ansys_3Z)) = [];

figure(5);plot(exp_L1,p_sg,'-
',ansys_1Z,ansys_pressure,':',exp_T1,p_sg,'-
',ansys_1Y,ansys_pressure,':','LineWidth',1.5)
xlabel('Strain (mm/mm)','FontSize',12,'FontWeight','bold')
ylabel('Pressure (bar)','FontSize',12,'FontWeight','bold')
legend('EXP L1','FEA L1','EXP T1','FEA T1','Location','southeast')
hold on

figure(6);plot(exp_L2,p_sg,'-
',ansys_2Z,ansys_pressure,':',exp_T2,p_sg,'-
',ansys_2Y,ansys_pressure,':','LineWidth',1.5)
xlabel('Strain (mm/mm)','FontSize',12,'FontWeight','bold')
ylabel('Pressure (bar)','FontSize',12,'FontWeight','bold')
legend('EXP L2','FEA L2','EXP T2','FEA T2','Location','southeast')
hold on

figure(7);plot(exp_L3,p_sg,'-
',ansys_3Z,ansys_pressure,':',exp_T3,p_sg,'-
',ansys_3Y,ansys_pressure,':','LineWidth',1.5)
xlabel('Strain (mm/mm)','FontSize',12,'FontWeight','bold')
ylabel('Pressure (bar)','FontSize',12,'FontWeight','bold')
legend('EXP L3','FEA L3','EXP T3','FEA T3','Location','southeast')
hold on
%
figure(8);plot(ansys_pressure,ansys_eqstress,'-','LineWidth',1.5)
xlabel('Internal Pressure (bar)','FontSize',12,'FontWeight','bold')
ylabel('Max Eqv. Stress (MPa)','FontSize',12,'FontWeight','bold')
axis([0 900 0 2100]);
legend('Location','southeast');
grid on;
hold on;

def_on_L2T2_r=full_data0(:,84);
def_on_L2T2_r(isnan(def_on_L2T2_r)) = [];

figure(9);plot(ansys_pressure,def_on_L2T2_r,'-','LineWidth',1.5)
xlabel('Internal Pressure (bar)','FontSize',12,'FontWeight','bold')
ylabel('Radial Deformation(mm)','FontSize',12,'FontWeight','bold')
axis([0 900 0 5]);
legend('Location','southeast');
grid on;
hold on;

def_on_polar_vertex_x=full_data0(:,88);
def_on_polar_vertex_x(isnan(def_on_polar_vertex_x)) = [];

figure(10);plot(ansys_pressure,def_on_polar_vertex_x,'-
','LineWidth',1.5)
xlabel('Internal Pressure (bar)','FontSize',12,'FontWeight','bold')
ylabel('Axial Deformation(mm)','FontSize',12,'FontWeight','bold')
axis([0 900 0 1.1]);
legend('Location','southeast');
grid on
hold on;
```

A.2. MATLAB Script for evaluating experimental tensile testing data

```
clear;clc;format compact;

co = [0 0 1;
      0 0.5 0;
      1 0 0;
      0 0.75 0.75;
      0.75 0 0.75;
      0.75 0.75 0;
      0.25 0.25 0.25
        0     0.4470    0.7410;
     0.8500    0.3250    0.0980;
     0.9290    0.6940    0.1250;
     0.4940    0.1840    0.5560;
     0.4660    0.6740    0.1880;
     0.3010    0.7450    0.9330;
     0.6350    0.0780    0.1840];
set(groot,'defaultAxesColorOrder',co)

full_data2=xlsread('al_tensile_modelling_redux_v4','sg_data','A3:AI300
0');

liner3_SG{1}=full_data2(:,1:3);
liner3_SG{2}=full_data2(:,4:6);

figure(1);plot(liner3_SG{1}(:,3),liner3_SG{1}(:,1),liner3_SG{1}(:,3),l
iner3_SG{1}(:,2),liner3_SG{2}(:,3),liner3_SG{2}(:,1),liner3_SG{2}(:,3)
,liner3_SG{2}(:,2));
hold on
full_data1=xlsread('al_tensile_modelling_redux_v4','raw_data_al_tensil
e','A4:AI3000');
specimen_sizes=xlsread('al_tensile_modelling_redux_v4','specimen_size'
,'C2:F6');

j=1; g=1; h=1; alpha=0.5;

gauge_length=specimen_sizes(:,3);
thickness=specimen_sizes(:,1);
width=specimen_sizes(:,2);
width_ext=specimen_sizes(:,4);

while j<=(size(full_data1,2))

    eng_strain_stress{g}(:,1)=full_data1(:,j+3)/gauge_length(g,1);

eng_strain_stress{g}(:,2)=full_data1(:,j+1)/(thickness(g,1)*width(g,1)
);
    eng_strain_stress{g}(:,3)=full_data1(:,j+4)/width_ext(g,1);
    eng_strain_stress{g}(:,4)=full_data1(:,j);
    g=g+1;
    j=j+7;
end

figure(1);plot(eng_strain_stress{4}(:,4),eng_strain_stress{4}(:,1),eng
_strain_stress{4}(:,4),eng_strain_stress{4}(:,3),eng_strain_stress{5}(
:,4),eng_strain_stress{5}(:,1),eng_strain_stress{5}(:,4),eng_strain_st
ress{5}(:,3))
```

```
figure(2);plot(abs(liner3_SG{1}(:,1)),liner3_SG{1}(:,2),abs(liner3_SG{
2}(:,1)),liner3_SG{1}(:,2),eng_strain_stress{4}(:,3),eng_strain_stress
{4}(:,1),eng_strain_stress{5}(:,3),eng_strain_stress{5}(:,1))

wo_nan1=liner3_SG{1}(:,1);
wo_nan2=liner3_SG{1}(:,2);
wo_nan3=liner3_SG{1}(:,3);
wo_nan1(isnan(wo_nan1)) = [];
wo_nan2(isnan(wo_nan2)) = [];
wo_nan3(isnan(wo_nan3)) = [];

liner3_SG{1}=[];
liner3_SG{1}=[wo_nan1 wo_nan2 wo_nan3];

sg_fit1=fit(liner3_SG{1}(:,3),liner3_SG{1}(:,2),'linearinterp');
sg_fit2=fit(liner3_SG{2}(:,3),liner3_SG{2}(:,2),'linearinterp');

sg_mech_test_time1=feval(sg_fit1,eng_strain_stress{4}(:,4));
sg_mech_test_time2=feval(sg_fit2,eng_strain_stress{5}(:,4));

figure(3);plot(eng_strain_stress{4}(:,1),eng_strain_stress{4}(:,2),eng
_strain_stress{5}(:,1),eng_strain_stress{5}(:,2),sg_mech_test_time1,en
g_strain_stress{4}(:,2),sg_mech_test_time2,eng_strain_stress{5}(:,2));

altensile_test_5=[eng_strain_stress{4}(:,4) sg_mech_test_time1
eng_strain_stress{4}(:,2)];
altensile_test_6=[eng_strain_stress{5}(:,4) sg_mech_test_time2
eng_strain_stress{5}(:,2)];

altensile_test_5=altensile_test_5(1:521,:);
altensile_test_6=altensile_test_6(1:521,:);
```

A.3. MATLAB Script for evaluating and synchronizing internal pressure and strain gauge measurements during burst pressure testing

```
clear;clc;

formatSpec = '%{HH:mm:ss:SSS}D%f%f';
T = readtable('al_liner3_02.csv','Delimiter',',','Format',formatSpec);

exp_time=T.TIME;
exp_duration=exp_time-exp_time(1,1);
exp_dur_secs=seconds(exp_duration);

cihaz_okuma=75;

exp_press=T.BASIN-cihaz_okuma;
yyaxis left
figure(1);plot(exp_dur_secs,exp_press);
hold on

sg_data=xlsread('sg_data_excel','sheet1','A5:G5000');

fark=7.2;

for i=1:1:size(sg_data,1)
sg_data_zero(i,:)=sg_data(i,:)-sg_data(1,:);
end
```

```matlab
sg_data_zero(:,7)=sg_data_zero(:,7)-fark;

yyaxis right
figure(1);plot(sg_data_zero(:,7),sg_data_zero(:,1:6));
axis(['auto y' 0 250])

pressure_fit=fit(exp_dur_secs,exp_press,'linearinterp');
p_sg=feval(pressure_fit,sg_data_zero(:,7));

figure(2);plot(sg_data_zero(:,1:6),p_sg);

figure(3);plot(exp_dur_secs,exp_press,sg_data_zero(:,7),p_sg);

for k=1:size(sg_data_zero,2)
    sg_smooth(:,k)=smooth(p_sg,sg_data_zero(:,k),0.2,'loess');
end
figure(30);plot(sg_data_zero(:,1:6),p_sg,'b.',sg_smooth(:,1:6),p_sg,'r
-');
hold on
```

VITA

Serkan KANGAL

30.07.1983, İzmir / TURKEY

EDUCATION

Ph.D. in Mechanical Engineering, İzmir Institute of Technology (2019)

M.Sc. in Materials Science and Engineering, İzmir Institute of Technology (2013)

B.Sc. in Chemical Engineering, İzmir Institute of Technology (2006)

RESEARCH INTERESTS

Composite materials, composite overwrapped pressure vessels, radar absorbing structures, lightweight structures, polymeric composite machining (cutting, drilling, trimming), additive manufacturing, numerical modeling for composite structures (modal analysis, transient analysis, explicit dynamics), vacuum infusion and resin transfer molding (RTM) composite manufacturing techniques for automotive, aerospace and wind turbine applications

Language – Turkish (Native), English (Full professional proficiency)

PUBLICATIONS

Journal Articles

S. Kangal, O. Kartav, M. Tanoğlu, H. Seçil Artem, E. Aktaş, Investigation of interlayer hybridization effect on burst pressure performance of high pressure composite pressure vessels with load sharing metallic liner, Journal of Composite Materials, August 2019 (Accepted, prepared for online publishing)

Preprints

M. Z. Okur, **S. Kangal**, M. Tanoğlu, Development of Aluminum Honeycomb Cored Carbon Fiber Reinforced Polymer Composite Based Sandwich Structure, Preprints 2018, (doi: 10.20944/preprints201812.0195.v1).

Selected Conference Proceedings

S. Kangal, O. Kartav, M. Tanoğlu, Development of Composite High Pressure Vessels for Hydrogen Storage, 9th International Automotive Technologies Congress (OTEKON 2018), May 2018, Bursa, Turkey

S. Kangal, M. D. Yaman, M. Tanoğlu, L. Özyüzer, Polymeric Composite Based Radar Absorbing Structures for Structural and Wideband Electromagnetic Wave Absorbing Applications, 3rd International Porous and Powder Materials Symposium and Exhibitions (PPM 2017), September 2017, İzmir, Turkey

B. Beylergil, **S. Kangal**, M. Z. Okur, E. Bilge, Ö. Türkaslan, E. Belen, D. Korkmaz, M. Tanoğlu, Development of Carbon Fiber Based Composites Prepared from Hybrid Fabrics with Different Weave Structure,3rd International Porous and Powder Materials Symposium and Exhibitions (PPM 2017), September 2017, İzmir, Turkey